mater.scichina.com link.springer.com

Sci China Mater 2026, 69(2): 1211–1222
https://doi.org/10.1007/s40843-025-3683-y

Strongly-adhesive hyaluronic acid/ε-PL aerogel for rapid hemostasis of life-threatening arterial bleeding and on-demand atraumatic removal

Lifei Huang[1], Quanrui Zhang[1], Fanglin Du[1], Zhihan Liu[1], Linwen Qiu[1], Yiming Wei[1], Wensheng Xie[1], Guofeng Li[1*], Dongsheng Kong[2*] and Xing Wang[1*]

ABSTRACT Effective management of traumatic hemorrhage requires not only rapid blood loss control but also facile removal of hemostatic materials after hemostasis to minimize secondary tissue damage. Herein, we fabricated a strongly adhesive aerogel OPA based on Schiff-base crosslinking of oxidized hyaluronic acid (OHA) and ε-polylysine (ε-PL), enabling rapid hemostasis in lethal arterial trauma and facile on-demand removal via phase transition to minimize secondary tissue damage. OPAs featured tunable porosity and rapid blood absorption. Moreover, the surface abundant hydroxyl, amino and carboxyl groups promoted strong hydrogen bonding interactions with tissues, blood cells and plasma proteins, enhancing tissue adhesion as well as platelet capture and activation. In the rabbit femoral-artery-injury model, OPA4 significantly shortened hemostatic time by ~80% and reduced blood loss to 38% of that in the blank group. Notably, OPAs retained only 2% of initial adhesion after hydration, allowing for gentle removal. OPAs also demonstrated excellent antibacterial activity, biocompatibility and biodegradability. Their simple one-step freeze-drying process and tailorable material shapes offered great promise for scalable production and versatile applications. Therefore, this study provides a versatile strategy for emergency and surgical hemostasis by combining rapid control of life-threatening arterial bleeding with on-demand atraumatic removal, promising to improve patient outcomes and streamline postoperative care.

Keywords: life-threatening arterial bleeding, hyaluronic acid, hemostatic aerogel, rapid hemostasis

INTRODUCTION

Traumatic hemorrhage poses a formidable challenge in both civilian and first aid settings, accounting for a substantial proportion of early preventable deaths [1–3]. Rapid prehospital intervention is critical, as delays in achieving hemostasis exponentially increase the risk of mortality [4,5]. Despite advances in hemostatic and surgical techniques, high-flow bleeding from vascular injuries, particularly in anatomically complex regions, remains difficult to control using conventional methods [6,7]. Traditional hemostatic materials (gauze dressings [8], cotton [9], and gelatin sponges [10]) are dedicated to rapid clot formation but often suffer from insufficient for the management of dynamic environmental wounds and fail to conform to complex wound geometries. These challenges underscore the urgent need for advanced hemostatic systems.

Recently, various types of hemostatic materials have been emerging. Inorganic hemostasis materials, including mesoporous silica [11,12], graphene [13–15], etc. [16–18], have excellent hemostatic properties. Yet, a critical limitation of these materials lies in their non-biodegradable nature. These materials must be manually removed, which requires manual removal after application. This process may lead to various adverse effects. Mechanical removal increases the risk of rebleeding, while residual materials may trigger foreign body reactions [19]. Moreover, the prolonged presence of non-degradable components can incite chronic immune activation, potentially leading to complications such as granuloma formation, fibrotic encapsulation, or secondary infections [19,20]. To address this, degradable materials capable of either *in vivo* degradation [21–25] or external stimulus-responsive disintegration [26–29] have been explored. Among them, polysaccharide-based hemostatic materials [30–32], such as chitosan [33,34] and hyaluronic acid (HA) [35,36], have emerged as promising candidates. These materials effectively concentrate hemocytes, promote platelet activation and initiate the coagulation cascade, thereby exhibiting potent hemostatic performance. Furthermore, their excellent biocompatibility and *in vivo* degradability after hemostasis have led to widespread clinical application in surgical procedures and wound care. Nevertheless, in prehospital settings involving life-threatening traumatic hemorrhage, prompt hemostasis must be followed by timely debridement for effective wound management. Traumatic wounds are frequently contaminated with exogenous materials such as soil, sand, or textile fibers. If these pollutants are sealed beneath the hemostatic dressing, they can create a closed, anaerobic microenvironment that significantly elevates the risk of infection. Moreover, ischemia-induced necrosis necessitates removal of dead tissue to promote wound healing [37–40]. In addition, Residual hemostatic materials that cannot be easily removed may act as a physical barrier obstructing wound drainage, triggering a foreign body reaction, or leading to chronic inflammation [41–43]. Thus, a key current challenge of hemostatic materials is the balance between rapid hemostasis and noninvasive debridement to avoid interfering with subsequent wound care.

Porous aerogels are advantageous in the treatment of arterial

[1] State Key Laboratory of Organic-Inorganic Composites, Beijing Laboratory of Biomedical Materials, Beijing University of Chemical Technology, Beijing 100029, China
[2] Department of Neurosurgery, First Medical Center, PLA General Hospital, Beijing 100853, China
* Corresponding author (email: ligf@mail.buct.edu.cn; kongdongsheng@301hospital.com.cn; wangxing@mail.buct.edu.cn)

© Science China Press 2026

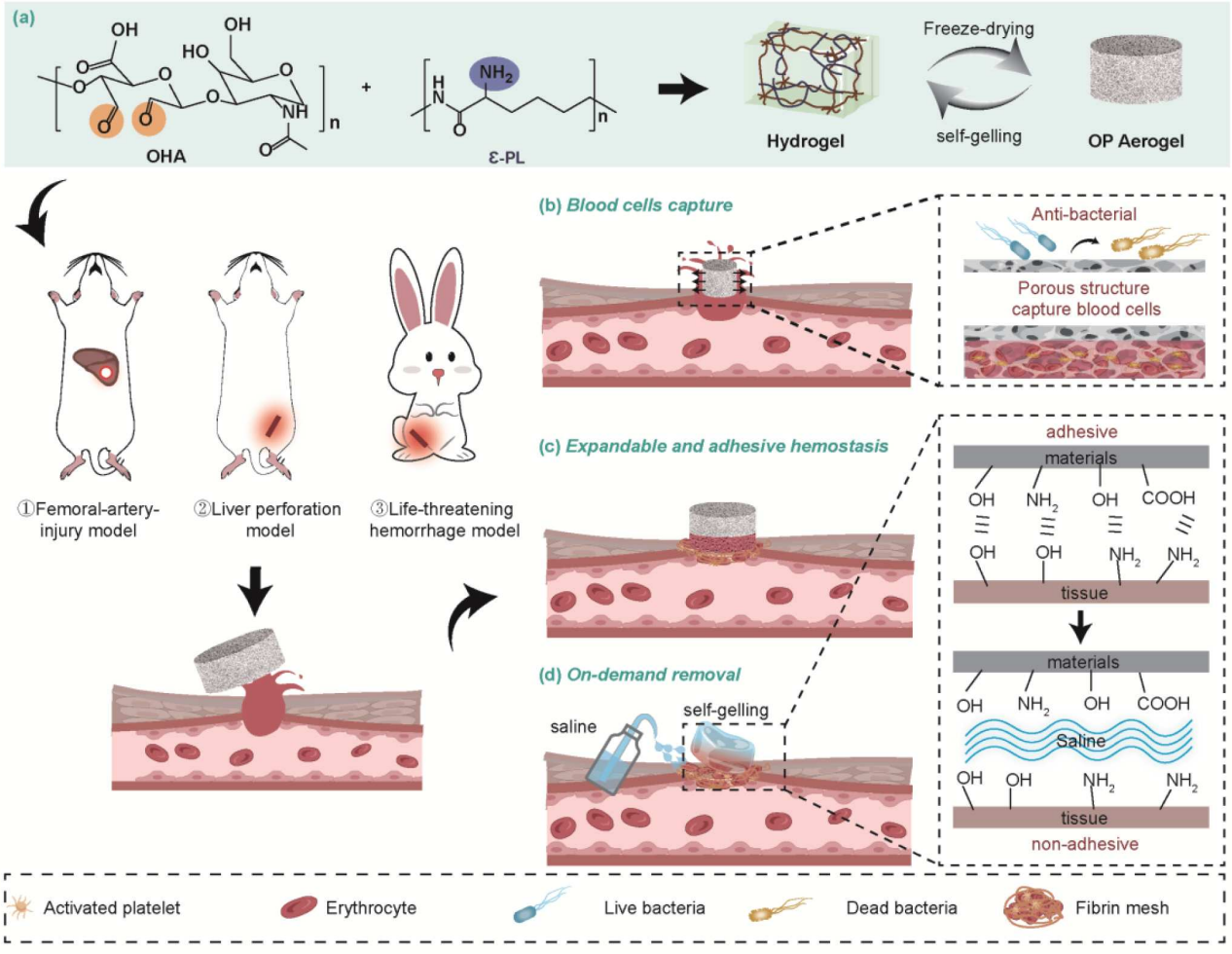
and visceral hemorrhage due to their excellent fluid absorbency, light weight, stability, portability and ease of handling [44–46]. Among the components used in aerogel preparation, HA, as a major component of extracellular matrix (ECM), can adhere well to tissues, supports healing, and is both biocompatible and degradable by *in vivo* enzymes [47–49]. Besides, the high-water retention properties of HA encourage it to fully allow water infiltration. These properties allow it to be an excellent scaffold for the development of hemostatic aerogels with potentially peelable qualities. Although HA has been extensively studied, current research efforts primarily focus on structural modifications and the development of composite materials to enhance hemostatic performance and impart additional functionalities, such as antibacterial activity and promotion of wound healing [50,51]. However, current hemostatic aerogels rarely integrate rapid adhesion hemostasis, antimicrobial activity and on-demand removability in a single system.

Therefore, we aimed to prepare a Schiff base cross-linked aerogel composed of oxidized hyaluronic acid (OHA) and ε-polylysine (ε-PL), termed OP aerogel (OPA) by a one-step freeze-drying process (Scheme 1). This aerogel has a simple preparation process, involves mild and biodegradable components, supporting further high-volume industrial production. OPAs were evaluated for fluid absorption properties, blood clotting index (BCI), platelet activation, hemocyte adsorption and antimicrobial properties to fully assess the fluid absorption and procoagulant ability of the OPAs. The *in vivo* degradation behavior was evaluated by subcutaneous implantation of aerogel. To simulate traumatic and non-compressible hemorrhage, the rat femoral-artery-injury model, liver perforation model and rabbit femoral-artery-injury model were employed. The adhesive hemostatic efficacy and on-demand removability of OPAs were assessed using a commercial absorbable gelatin hemostatic sponge (AGS) as a control. Finally, the "adhesive hemostasis and on-demand removal" mechanism of OPAs was thoroughly investigated using a porcine intestinal mucosa adhesion model.

EXPERIMENTAL SECTION

Animals

The rat research was carried out by the National Research Council's Guide for the Care and Use of Laboratory Animals



Scheme 1 Schematic illustration for the preparation, applications and features of OPAs. (a) OPAs were prepared from OHA and ε-PL by a one-step freeze-drying process. (b, c) OPAs could adhere strongly to tissue via hydrogen bonding due to the abundance of hydroxyl, amino and carboxyl groups on the surface, and rapidly absorb blood, thus exhibiting fast and excellent hemostatic properties. (d) After hemostasis, OPAs transformed into a hydrogel upon saline exposure and the infiltration of saline into the adhesion interface disrupted the hydrogen bonding interaction between the material and the tissue, facilitating atraumatic detachment.

© Science China Press 2026

and was authorized by the Animal Section of the SPF of the China-Japan Friendship Hospital (approval number: 211001). The rabbit research was carried out by the National Research Council's Guide for the Care and Use of Laboratory Animals and was authorized by the Laboratory Animal Ethics Committee of Beijing Yongxin Kangtai Technology Development Co., Ltd. (refinement No. YXKT2025L020).

Statistical analysis

All the values in this work were presented as mean ± standard deviation. The Student's *t*-test was employed for the comparison between the two groups. Differences between multiple groups were evaluated by one-way analysis of variance (ANOVA). $*p < 0.05$ was considered statistically significant. $^{\#/}*p < 0.05$, $^{\#\#/}**p < 0.01$, $^{\#\#\#/}***p < 0.0001$, $^{\#\#\#\#/}****p < 0.0001$.

RESULTS AND DISCUSSION

Synthesis and characterization of OPA

The OPA was prepared by a facile two-step reaction (Scheme 1a). First, HA was oxidized by $NaIO_4$ to generate OHA with aldehyde group. The aldehyde group of OHA reacted with the amino group of ε-PL to form Schiff base bonds, which were chemically crosslinked to obtain a hydrogel. Further, the hydrogel was freeze-dried to prepare OPA. The structure of OHA was confirmed by ^{1}H nuclear magnetic resonance (NMR) and Fourier transform infrared (FTIR) spectra. In the ^{1}H NMR spectrum of OHA, additional peaks at 4.99, 5.10 and 5.20 ppm confirmed the successful aldehyde modification of HA (Fig. S1). Furthermore, the FTIR spectrum exhibited a characteristic absorption band at 1730 cm^{-1}, further confirming the presence of the –CHO group (Fig. S2). The M_w of OHA determined by gel permeation chromatography (GPC) was 155,629 Da (Fig. S3, Table S1). The degree of oxidation (DO) of OHA was determined using the hydroxylamine hydrochloride titration method and was found to be approximately 23% [52]. Subsequently, the obtained OHA underwent a mild reaction with ε-PL at room temperature. After freeze-dried, regular-shaped aerogel material OPA was obtained. During preparation, the temperature of freezing was found to affect the morphology of the aerogel. The morphology of aerogels obtained under different freezing conditions was further examined (Fig. S4). When frozen at −20°C, irregular pores and uneven cross-linking were exhibited. Liquid-nitrogen freeze-drying (~−196°C) was found to be excessively harsh, causing cross-linking points to fracture and uniform pore formation to be inhibited. An optimal freezing temperature of −80°C produced aerogels with well-defined, regularly sized pores. The possible reasons are that freezing at −20°C results in slower ice crystal formation, producing larger and unevenly distributed crystals that lead to irregular and poorly connected pore structures [53]. In contrast, ultra-rapid freezing at −196°C introduced high stresses, which could cause structural cracking or uneven shrinkage during drying [54]. Freezing at −80°C may offer an optimal balance between freezing rate and structural preservation. At this temperature, water rapidly formed fine and uniformly distributed ice crystals, which sublimated to create a highly porous and interconnected aerogel network. This well-organized porous structure enhanced structural integrity, improved liquid absorption capacity and increased the specific surface area. Therefore, −80°C was used as the optimized freezing temperature for subsequent experiments. Regulating the concentration of the aerogel components allowed a range of aerogels (OPA_3, OPA_4, OPA_5) to be prepared. Scanning electron microscopy (SEM) showed that all OPAs contained many interconnected pores, but with varying pore sizes (Fig. 1a, Fig. S5). As the percentage of OHA increased, the porosity of OPAs decreased from 57.67% ± 2.87% in OPA_3 to 44.33% ± 1.25% in OPA_5 (Fig. S6). The pores of the aerogel become denser as the proportion of OHA increases, which is related to the increase in the number of aldehyde groups, leading to a tighter cross-linking network. Interestingly, there was no significant difference in porosity from OPA_4 to OPA_5, which may be related to the limited cross-linkage points and spatial site resistance caused by high OHA concentration.

Absorption and mechanical properties

Hemostatic materials must not only absorb blood from excessively bleeding wounds but also adapt to different wound conditions. Thereby, they need to be capable of possess moldability and liquid uptake. The porous structure of OPAs may confer outstanding liquid absorption ability. OPAs (0.5 cm × 0.5 cm × 0.5 cm) were placed in 3 mL of water (with methylene blue added for observation) to assess the water absorption properties (Figs S7 and S8a). OPA_3 exhibited negligible swelling throughout the 5 min observation period, with its structure remaining largely unchanged, indicating poor fluid absorption and limited swelling capacity (Fig. S8a, b). In contrast, OPA_4 demonstrated moderate swelling, with a noticeable increase in volume beginning around 1 min and gradually progressing over the 5 min interval. OPA_5 displayed rapid and sustained swelling, initiating within the 1 min of immersion and resulting in a substantial volume increase by 5 min. Quantitative analysis of the total swelling ratio (Fig. S8c) confirmed these trends. The swelling ratio of OPA_3 was relatively low at 362.00% ± 33.94% after 300 s. OPA_4 exhibited a moderate water absorption capacity, with a swelling ratio of 842.00% ± 59.40%. In contrast, the swelling ratio of OPA_5 increased dramatically, reaching 2892.27% ± 271.91% in the same time frame, indicating superior swelling properties. Furthermore, each OPA absorbed several times its own weight in water (OPA_5: 112.43 ± 6.85 w/w%; OPA_4: 85.69 ± 5.11 w/w%; OPA_3: 47.22 ± 1.91 w/w%) (Fig. 1b, c), collectively demonstrating excellent liquid uptake capacity. These findings indicate that increasing the OHA content enhances the hydrophilicity of porous network and capillary suction, thereby boosting liquid absorption ($OPA_5 > OPA_4 > OPA_3$). Upon water absorption, the aerogel gradually transformed into a hydrogel, highlighting its reversible phase-transition capability. This transformation is attributed to the rehydration of the porous matrix, which swells and retains water within its three-dimensional network, improving compliance with irregular wound surfaces.

The location and depth of bleeding impose stricter requirements on the shape and size of hemostatic materials. In this context, the ability to fabricate materials with adaptable and customizable shapes becomes particularly important for ensuring adequate coverage and effective hemostasis. Therefore, three typical aerogels of spherical, cylindrical and cuboid morphologies were prepared. Among the different shapes, spherical structures are especially suitable for catheter-mediated delivery systems, commonly employed as embolic agents. Cylindrical forms can fill bleeding cavities or perforations in soft tissue. Cuboid shapes are well suited for application to wounds with

© Science China Press 2026

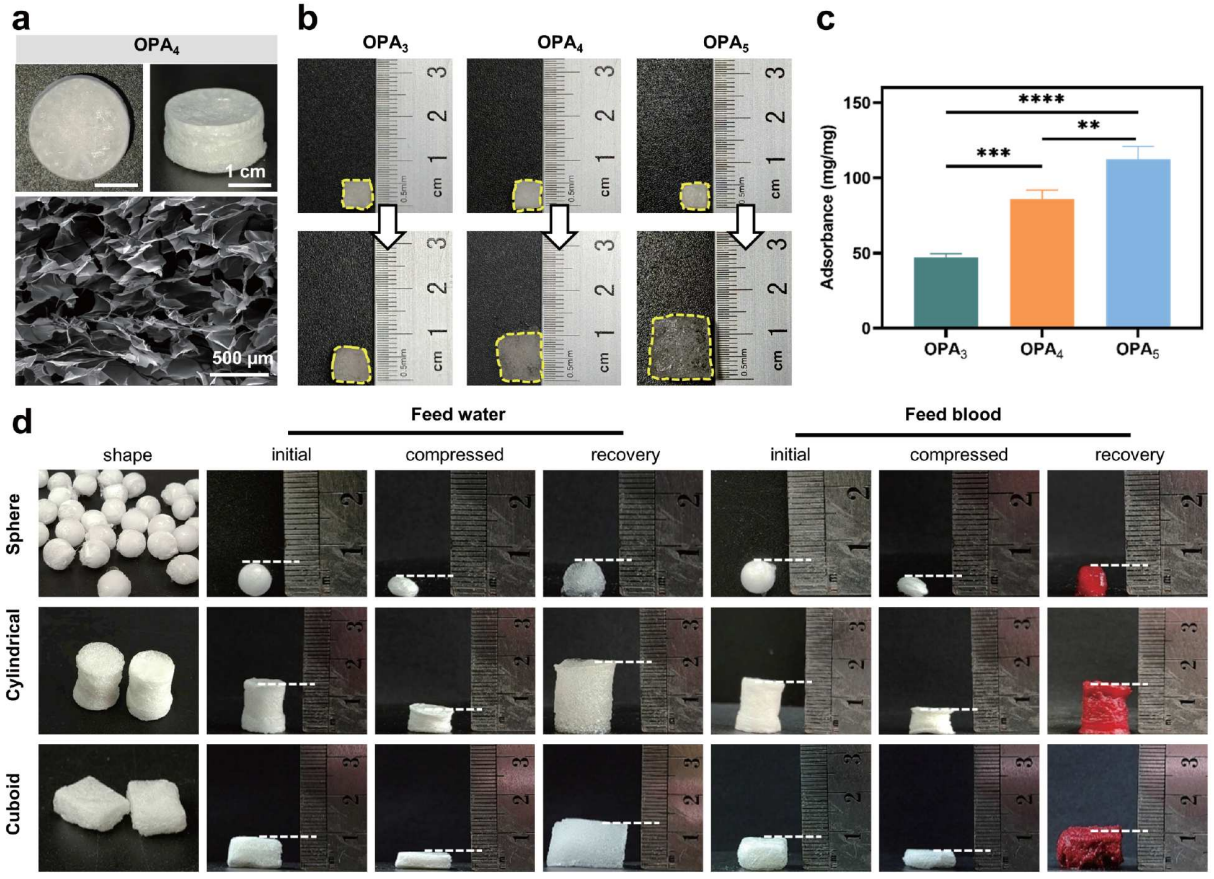


Figure 1 Liquid absorption and swell properties of OPAs. (a) Photographs of OPA_4 and corresponding SEM images. (b) Swelling behavior and morphological transformation of a representative OPA cube (0.5 cm × 0.5 cm × 0.5 cm) and (c) corresponding total liquid absorption (w/w%). (d) Photographs of shape memory performance of the macroscopic appearance of OPAs (sphere, cylindrical and cuboid) in water and blood. Error bar indicates SD (n = 3), *p < 0.05, **p < 0.01, ***p < 0.001, ****p < 0.0001.

irregular skin surfaces, offering better conformability and coverage over uneven areas. All forms retained an intact porous structure during fabrication and lyophilization. Moreover, the ability of the aerogel to undergo compression and rapid shape recovery in water and blood environments was further evaluated on three geometries (Fig. 1d). The "compressed-recovery" behavior of the three aerogel shapes exhibits several common features. Firstly, after a uniaxial compression of more than 50% in water or blood, all forms recovered to more than 90% of their original height. This indicates that the aerogels can be stored in a compressed state and subsequently re-expand upon fluid absorption, making them suitable for compact storage and rapid deployment. Secondly, the recovery was consistently higher in water compared to blood. This is mainly due to blood containing cellular components (red blood cells, white blood cells and platelets) and high-molecular-weight proteins (fibrinogen, albumin, etc.), giving it a viscosity 3–4 times that of water [55]. Taken together, OPAs exhibit excellent fluid uptake and "compressed-recovery" capabilities, laying the material foundation for subsequent *in vivo* hemostatic efficacy evaluations.

Blood cells and platelets adhesion properties

The ability of hemostatic materials to aggregate blood cells is crucial for the coagulation process. *In vitro* blood clotting ability was assessed by whole blood coagulation assay. As shown in Fig. 2a, OPAs effectively accelerated blood coagulation and reduced hemoglobin release. Statistical analysis of BCI values (Fig. 2b) demonstrated that OPAs exhibited excellent procoagulant activity, with OPA_4 showing the most pronounced effect (2.58% ± 0.73%), significantly outperforming the commercial hemostat AGS (22.16% ± 2.63%). To further investigate the hemostatic mechanism, the erythrocyte-adhered hemostatic materials were examined by SEM. Numerous erythrocytes were found adhered to the surface of OPA_4 (Fig. 2c). In addition, platelets with typical activated pseudopodia-like morphology were observed in OPA_4. The adhered rate of OPA_3 to erythrocytes and platelets (66.97% ± 1.54%, 64.64% ± 4.18%) was significantly higher than that of AGS (48.89% ± 1.61%, 41.72% ± 1.15%) (Fig. 2d, e). Noticeably, OPAs showed no significant differences between them. Thus, OPAs are effective in accumulating blood cells and activating platelets, which is mainly attributed to the highly interconnected porous network that promotes rapid and extensive absorption of blood and effective aggregation of red blood cells.

Antimicrobial properties

The good antimicrobial activity of the hemostatic material helps to prevent bacterial infection during hemostasis. To investigate the antimicrobial efficacy of OPAs, their bacteriostatic activity against *E. coli* and *S. aureus* was evaluated using the zone of inhibition assay. As shown in Fig. 3a, clear inhibition zones were observed around OPHs and ε-PL discs, while the blank group

© Science China Press 2026

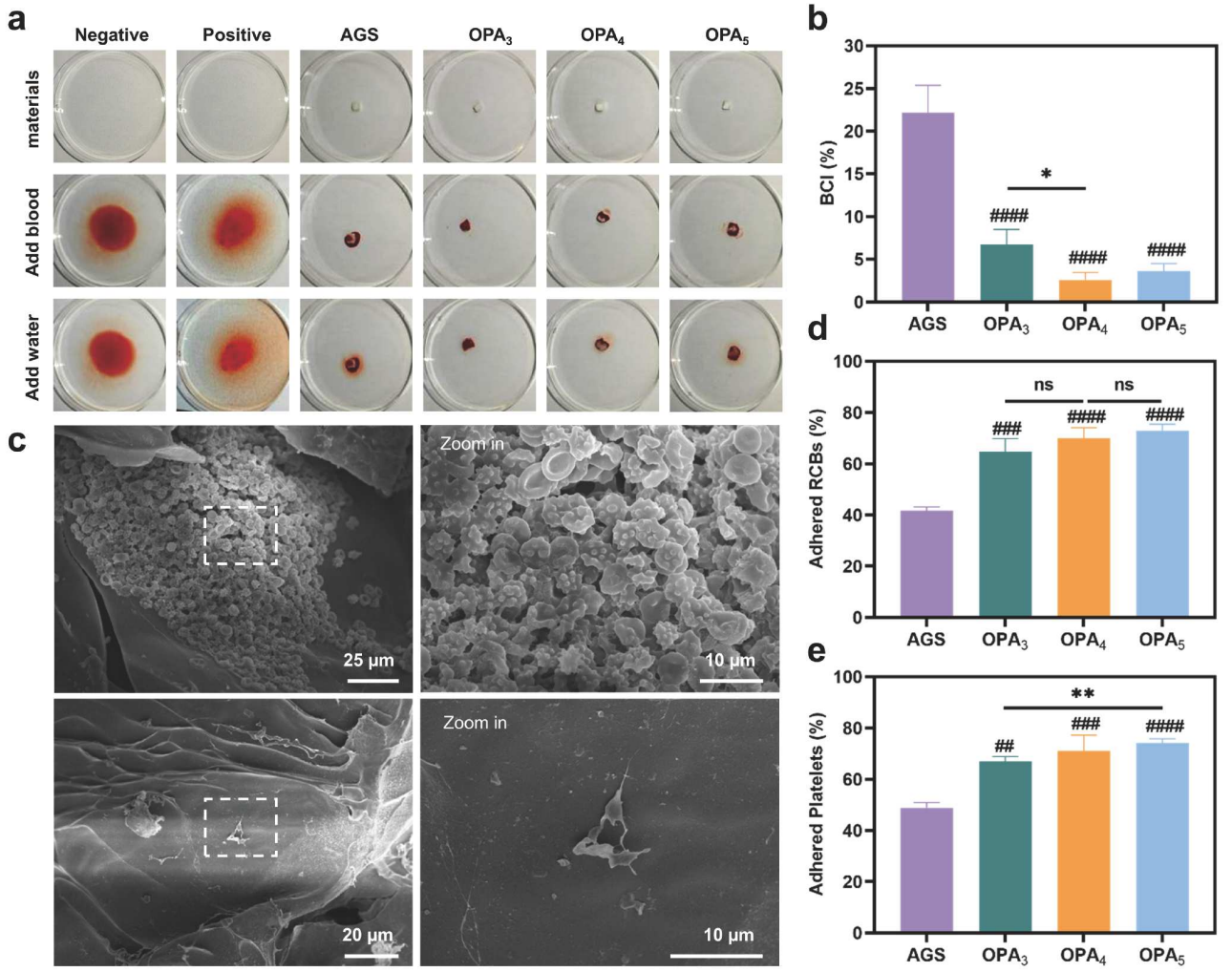


Figure 2 *In vitro* clotting properties of OPAs. (a) Hemoglobin release from blood in contact with different samples (AGS and OPAs). Negative control: PBS. Positive control: water. (b) BCI of OPAs. (c) SEM images showing the adhesion of red blood cells (RBCs) and activation of platelets on the surface of OPA_4. (d) Quantification of RBCs and (e) platelets adhered ratio of AGS and OPAs. Error bar indicates SD (n = 3), # means the contrasts between experimental groups and AGS, $^{\#/*}p < 0.05$, $^{\#\#/**}p < 0.01$, $^{\#\#\#/***}p < 0.001$, $^{\#\#\#\#/****}p < 0.0001$.

and OHA group exhibited no significant antimicrobial activity, indicating that ε-PL contributes to the antibacterial properties of the aerogel. The quantitative analysis of the inhibition zone diameters (Fig. 3b, c) suggested that both OPHs and ε-PL significantly inhibited bacterial growth compared to the blank and OHA group. OPAs had a notable inhibitory effect on *E. coli*. and *S. aureus*, suggesting that OPAs possessed broad-spectrum antibacterial properties. The cationic ε-PL possesses broad-spectrum antibacterial activity. As the material degrades, the gradually released ε-PL, together with a small amount of non-covalently bound ε-PL to exert antibacterial effect, helped reduce the risk of infection at the wound interface.

Biocompatibility and *in vivo* biodegradation

The cytotoxicity of OPAs was evaluated using the L929 cells (Wuhan Servicebio Technology Co., Ltd. (China)). A series of OPAs was co-incubated with the cells for 24 h at a concentration of 10 mg/mL and then stained with Calcein AM/propidium iodide (PI). The results displayed that the cells almost entirely displayed green color with a few sporadic red fluorescence (Fig. 3d), indicating that OPAs were biocompatible at this concentration. The viability of L929 cells incubated with the extract was further measured by MTT assay. The cell viability was all above 95% (Fig. 3e, Fig. S9), confirming a high biocompatibility. Hemocompatibility was assessed by hemolytic activity assay. After incubation with OPA_4, the supernatants obtained from the erythrocyte suspensions were all a light color, close to the negative control of the PBS group (Fig. 3f, Fig. S10). Quantitative data indicated that the hemolysis rate was less than 5%. Therefore, OPAs have low cytotoxicity and good hemocompatibility. For *in vitro* degradation experiments, OPAs degraded within 24 h (Fig. S11), but *in vivo* degradation is unknown. To this end, OPAs were placed subcutaneously on the back of rats (Fig. S7, Fig. 3g). No aerogel material was observed at the implantation site after one week. Hematoxylin and eosin (H&E) staining analysis of the obtained rat back skin tissues showed that the back skin of the implanted group showed a physiological state identical to that of the control group. The skin tissue displayed a neat and orderly cell arrangement, a uniform direction of muscle fibers and without inflammatory reaction (Fig. 3h). This means that porous OPAs combine excellent fluid absorption, inherent antimicrobial efficacy and

© Science China Press 2026

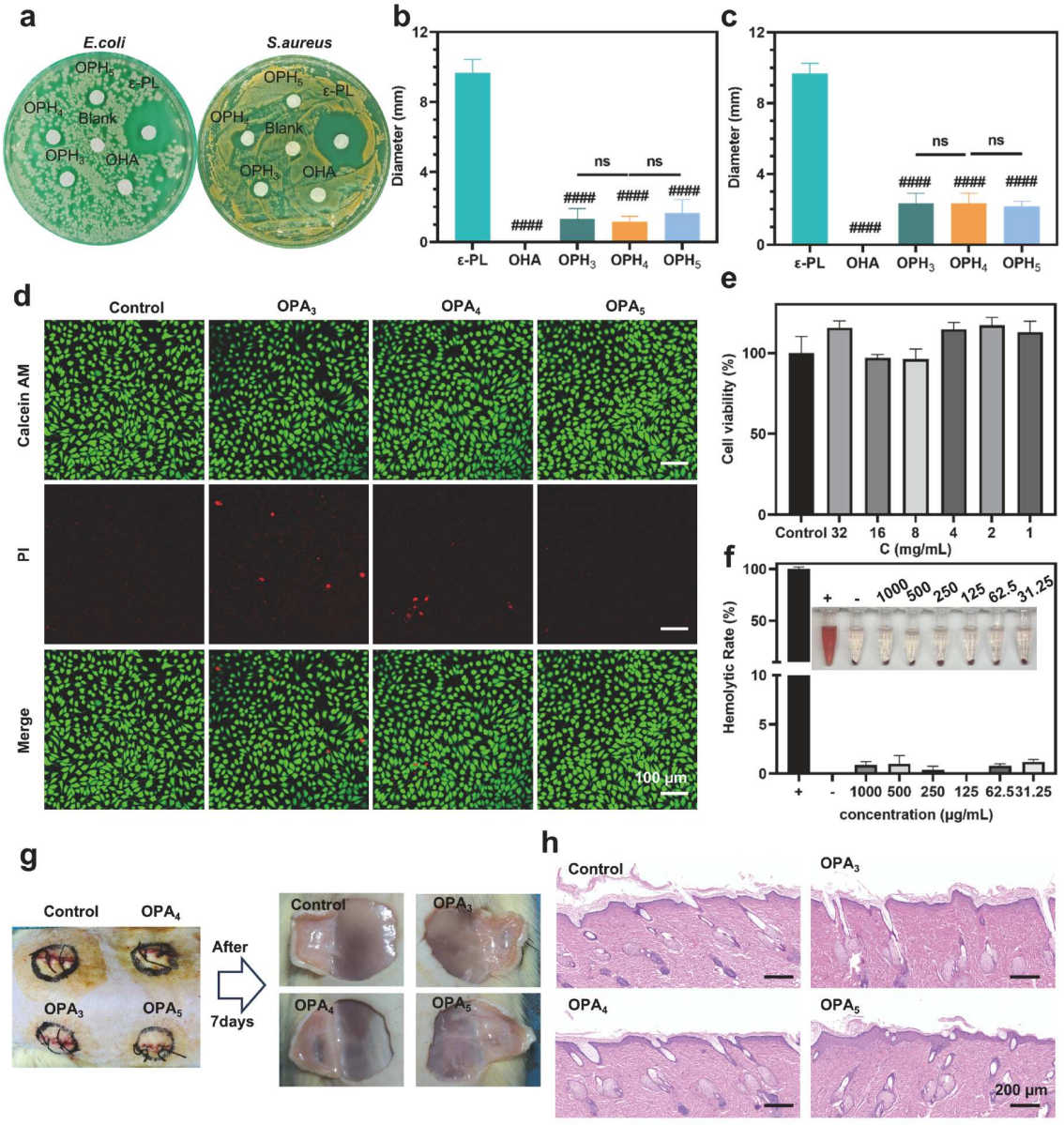


Figure 3 Evaluation of antimicrobial properties, biosafety and *in vivo* biodegradability of OPAs. (a) Representative images of inhibition zones produced by OPHs and OHA, ε-PL against *E. coli* and *S. aureus*. Quantitative analyses of the zone of inhibition of (b) *E. coli* and (c) *S. aureus* (n = 3). (d) Cytotoxicity of OPAs assessed via Calcein AM/PI staining and (e) cell viability following incubation with the extract of OPA_4 (n = 6). (f) Hemolytic assessment of OPA_4 and corresponding hemolysis ratio (n = 3). (g) Optical images of OPAs after subcutaneous implantation and of the implantation sites after 7 days. (h) H&E staining of skin tissue in direct contact with OPAs. Error bar indicates SD, # means the contrasts between experimental groups and ε-PL, $^{\#/}*p < 0.05$, $^{\#\#/}**p < 0.01$, $^{\#\#\#/}***p < 0.001$, $^{\#\#\#\#/}****p < 0.0001$.

outstanding biocompatibility with the potential to be used for rapid control of bleeding.

In vivo hemostatic capacity

To evaluate the hemostatic efficacy of OPAs, three hemostatic models were established *in vivo*: rat femoral-artery-injury model, rat liver perforation model and rabbit femoral-artery-injury model. Fig. 4a illustrates the hemostatic process of materials in the femoral-artery-injury model. The hemostatic time and blood loss of different groups were quantitatively assessed (Fig. 4b, c). The blank group exhibited prolonged hemostatic time (129.60 ± 10.90 s) and significant blood loss (4.85 ± 0.22 g), while the commercial hemostat AGS group had less 45% hemostatic time (71.60 ± 4.64 s) and less 44.90% blood loss (2.67 ± 0.11 g) than blank. Notably, OPA_3 (66.60 ± 2.92 s; 0.31 ± 0.04 g), OPA_4 (41.20 ± 2.27 s; 0.19 ± 0.02 g) and OPA_5 (59.80 ± 3.89 s; 0.31 ± 0.03 g) significantly reduced both hemostatic time and blood loss compared to the blank and AGS groups. The hemostatic time and blood loss result (Fig. 4f, g) further validated these observations, showing that OPAs materials (OPA_3, 0.17 ± 0.01 g; OPA_4, 0.11 ± 0.01 g and OPA_5, 0.23 ± 0.03 g) significantly outperformed AGS and the blank control in controlling hemorrhage. Among the tested materials, OPA_4 exhibited the shortest hemostatic time, which was 83%, 76%, 46%, 58% less than blank, AGS, OPA_3, OPA_5, indicating its superior hemostatic efficiency. Again, OPA_4 demonstrated the best perfor-

© Science China Press 2026

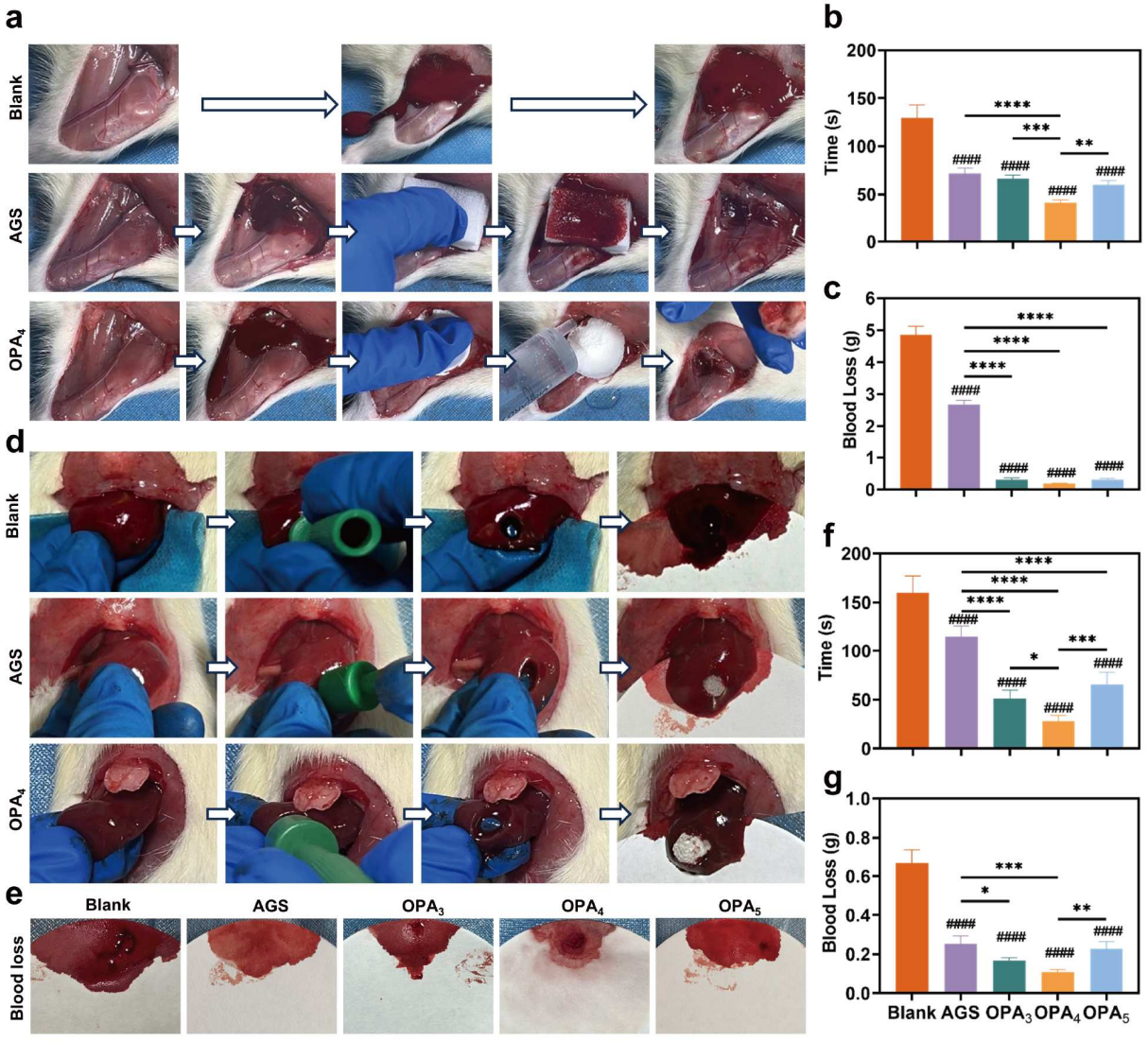


Figure 4 *In vivo* hemostatic performance of OPAs in rat models. (a) Representative images of the hemostatic process in the SD rat femoral artery injury model of blank, AGS, OPA_4. (b) Hemostatic time and (c) total blood loss of blank, AGS, OPAs-treated groups. (d) Hemostatic process in the rat liver perforation model of blank, AGS, OPA_4. (e) Blood loss assessed by filter paper staining. (f) Statistical hemostatic time and (g) blood loss of blank, AGS, OPAs-treated groups in the rat liver perforation model. Error bar indicates SD (n = 5), # means the contrasts between experimental groups and blank, $^{\#/*}p < 0.05$, $^{\#\#/**}p < 0.01$, $^{\#\#\#/***}p < 0.001$, $^{\#\#\#\#/****}p < 0.0001$.

mance, achieving the most rapid hemostasis with minimal blood loss. This indicates that the proportion of material components affects properties such as porosity and water absorption rate; these factors alone do not determine the final hemostatic performance of the material. Considering the results, such as blood cell adsorption and BCI, OPA_4 presents a more balanced profile of water absorption, mechanical strength, and adhesion, thereby demonstrating superior hemostatic efficacy *in vivo*. The results from both arterial and parenchymal bleeding models confirm the superior hemostatic efficacy of OPA formulations, particularly OPA_4. The observed performance can be attributed to the optimized composition of OPAs, which enables rapid absorption of blood, strong adhesion to the wound site and effective clot formation. Compared with commercial hemostat AGS, OPAs not only absorb blood quickly, but also activate platelets and promote coagulation. The *in vivo* results suggest that OPAs exhibit effective hemostatic performance. Its porous structure facilitates rapid fluid absorption and cell embedding, while the ε-PL component enhances blood cell aggregation, further contributing to hemostasis. Additionally, OPA conforms to the wound morphology, enabling mechanical occlusion to aid in bleeding control. Among the tested formulations, OPA_4 holds significant potential as a highly effective hemostatic biomaterial for clinical applications. Moreover, the noninvasive peeling of OPAs is a critically important advantage when treating sensitive anatomical regions such as internal organs or blood vessels.

In addition, a life-threatening hemorrhage model was established via transection of the rabbit femoral artery (Fig. 5a). Under hypertensive conditions, the blood flow usually shows jet and high-flow bleeding (Fig. 5b). The hemostatic time was higher than 20 min and the blood loss (41.37 ± 18.96 g) was large when relying solely on gauze and compression (Fig. 5b–d). The commercial chitosan-based Celox powder could achieve rapid hemostasis with the aid of compression (2.66 ± 0.26 min,

© Science China Press 2026

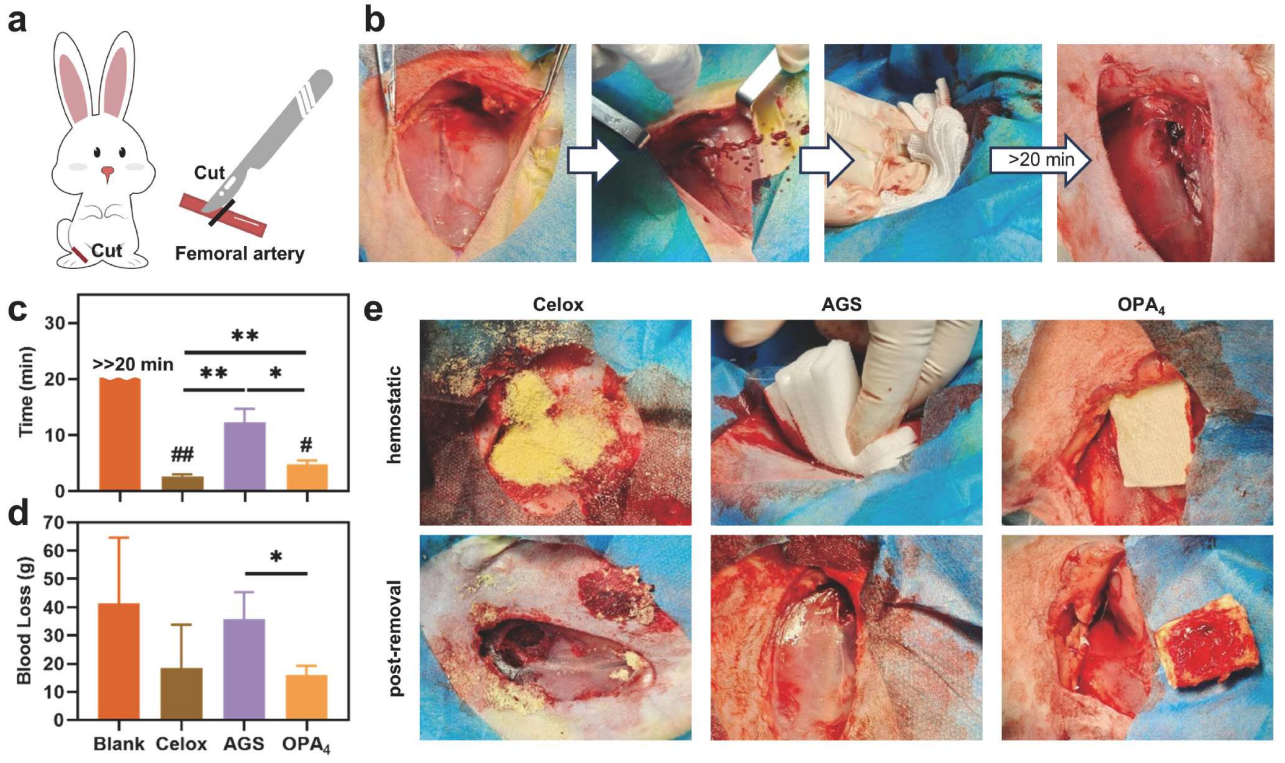


Figure 5 *In vivo* hemostatic performance of OPA_4 in the rabbit femoral-artery-injury model. (a) Schematic illustration of the rabbit femoral artery transection hemorrhage model. (b) Procedure for hemostasis using gauze. (c) Hemostatic time and (d) total blood loss of blank, Celox, AGS, and OPA_4 in the rabbit artery injury model. (e) Representative images of intraoperative hemostasis and post-hemostatic debridement of Celox, AGS and OPA_4. Error bar indicates SD (n = 3), # means the contrasts between experimental groups and blank, $^{\#/*}p < 0.05$, $^{\#\#/**}p < 0.01$.

18.33 ± 12.57 g). In contrast, the AGS was insufficient to control bleeding under these conditions, resulting in markedly prolonged hemostatic time (12.25 ± 1.75 min) and increased blood loss (35.70 ± 6.80 g) compared to the Celox group. The hemostatic time of the OPA_4 (4.79 ± 0.54 min) was 80% higher than that of the Celox group, 60.87% less than that of AGS. The blood loss of OPA_4 (15.90 ± 2.69 g) was 13% and 55% less than that of Celox and AGS, respectively. Although Celox exhibited the shortest hemostatic time, it also presents non-negligible drawback. It was prone to being washed away by high-pressure blood flow and was difficult to remove after hemostasis, posing a problem for postoperative debridement (Fig. 5e). In comparison, OPA_4 could be readily removed by simple saline irrigation following bleeding control. Hence, OPA_4 not only provides effective and rapid hemostasis but also offers operational advantages in terms of stability under pressure and ease of removal, emphasizing its potential as a superior hemostatic agent for arterial bleeding under extreme conditions.

Adhesion behavior and mechanism

After hemostasis with OPA_4 was achieved, the material adhered firmly to the tissue surface. The hemostatic interface could be easily moistened with saline, allowing the OPA_4 to be gently removed without secondary bleeding or material residue (Fig. 6a). To systematically investigate the adhesive properties of the developed aerogel-based systems, the adhesive properties were analyzed by peel strength measurements and interfacial interactions. OPA_4 was able to adhere to organs and tissues (Fig. 6b). Further, OPA_4 adhered to the mucosa of porcine small intestine and was lifted, stretched, bent and twisted without detachment (Fig. S12). This suggested that OPAs were suitable for hemostatic applications in a dynamic environment, particularly in anatomically complex regions such as the liver and major arteries. Inspired by the above results, an adhesion testing system was constructed, as shown in Fig. 6c. The adhesive system consists of an interface between functionalized aerogels (OPAs) and biological tissues under controlled separation forces (Fig. S13). Comparative peeling strength tests (Fig. S14a) revealed that the OPAs systems exhibited significantly enhanced adhesive strength compared to the commercial hemostat AGS group. This indicated that the hydroxyl, amino and carboxyl groups on the surface of OPAs form hydrogen bonding interactions with the tissue surface, resulting in adhesion. Specifically, OPA_4 achieved a peak peeling strength of 8.16 ± 0.22 kPa under blood-added interface conditions, which was 217% higher than AGS (1.45 ± 0.22 kPa) (Fig. 6d, Fig. S14a).

Notably, the interfacial interaction between the material and tissue could be disrupted upon the introduction of saline. After application of water at the interface, a marked reduction in peel strength was observed (Fig. 6e, Fig. S14b). Exactly, the peak peel strength of OPA_4 was 2% of the initial adhesion (0.47 ± 0.07 kPa) and AGS remained at 36% (0.52 ± 0.05 kPa) under interfacial water addition. On the one hand, upon water absorption, OPAs underwent swelling and self-gelation, accompanied by softening and pore shrinkage, thereby enhancing interfacial lubricity and reducing friction. Additionally, water molecules infiltrated the interface and disrupted pre-existing hydrogen bonds between the material and tissue,

© Science China Press 2026

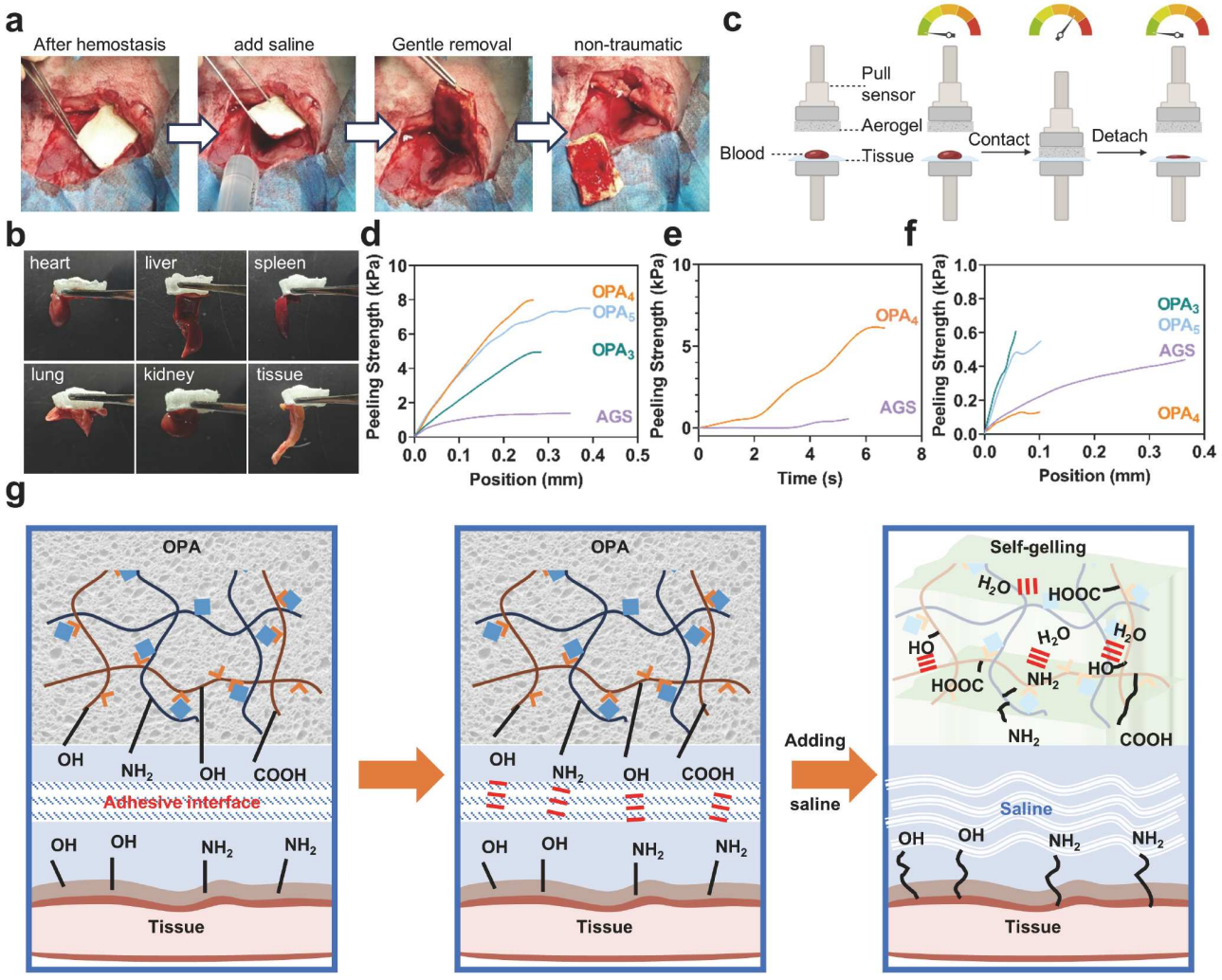


Figure 6 Mechanisms for "adhesion-removal" performance of OPAs. (a) Gentle removal of OPA_4 after hemostasis. (b) Photographs of aerogel adhesion to tissues and organs. (c) Schematic illustration of the setup for quantifying the peeling strength between OPAs and porcine small intestinal mucosa. Peeling strength between OPAs and the mucosal surface with (d) blood and (e) saline. (f) Quantitative analysis of tissue adhesion. (g) Schematic illustration of the adhesion mechanism of OPAs.

causing a decrease in adhesion. The adhesive performance on biological tissues was further evaluated *in vivo* (Fig. S15a). In the rat femoral artery injury model, OPA_4 exhibited strong adhesion to tissue with a measured strength of 7.05 ± 0.64 kPa, whereas AGS showed minimal adhesion, registering only 0.66 ± 0.14 kPa (Fig. 6f, Fig. S15b). These results collectively demonstrate that OPAs provide strong initial tissue adhesion for effective hemostasis while allowing for gentle, on-demand removal through simple water application.

Given these results, the mechanism of "strongly-adhesive and on-demand removal" of OPAs is elucidated in Fig. 6g. The surface of OPAs was functionalized with hydroxyl (–OH), amino ($–NH_2$) and carboxyl (–COOH) groups, which collectively facilitated robust interactions with tissue surfaces. Upon application, these groups formed hydrogen bonding with tissue proteins ($–NH_2$, –COOH) [56,57]. Notably, the initial contact of the aerogel with tissue occurred more rapidly than the diffusion of blood across the adhesive interface. Thus, functional groups on the aerogel surface could form preliminary anchoring interactions with the tissue. In turn, the porous structure of the aerogel created a negative capillary pressure that actively drew water and cellular components from the blood. These combined effects minimized disruption of the adhesive interface by blood, allowing the blood to be absorbed into the aerogel network and contributed to hemostasis before the interface is compromised. Additionally, the introduction of saline or water modulated the interfacial environment: when water was added at the interface, the aerogel absorbed the water and turned into a hydrogel. This may change the physical and chemical properties of the material surface. First, the intervention of water molecules could shield or weaken the interactions between functional groups [58]. For example, hydroxyl, amino and carboxyl groups could hydrate in water, thereby reducing the effectiveness of tissue contact [59]. Another possible factor was the lubricating effect of water. In a moist environment, the coefficient of friction between the aerogel and the tissue was reduced, thus decreasing physical adhesion. These factors altogether contributed to the atraumatic removal of OPAs. For incompressible wounds, particularly under the conditions of high blood flow and elevated pressure within the liver, insertion of the cylindrical aerogel material into

© Science China Press 2026

the perforation immediately created a "plugging" effect. By physically blocking the bleeding channel, OPAs effectively stopped the blood flow. Subsequently, the porous network of the aerogel rapidly absorbed blood via capillary action, capturing blood cells and platelets within its pores and facilitating the rapid formation of a fibrin network. This generated a dense composite of coagulation materials. Following the establishment of the initial clot, the internal fibrin structure continued to aggregate and remodel under the shear forces exerted by ongoing blood flow. This dynamic reinforcement permitted the aerogel-clot interface to maintain structural integrity. OPAs could further be easily removed in the presence of water. Thus, by integrating hydrogen bonding interactions and structural adaptations, OPAs achieve tunable adhesion and controlled removal suitable for dynamic biological environments.

CONCLUSIONS

In this study, a facilely prepared OPA cross-linked with Schiff base bonds integrated rapid hemostasis and controlled removal to maximize hemostatic efficacy and minimize secondary injury. Upon blood exposure, the hydroxyl, amino and carboxyl groups on the surface could form strong adhesions with tissues via hydrogen bonding. Whereas, the interconnected pores drove swift plasma uptake and local enrichment of platelets and coagulation proteins. In the rat femoral-artery-injury model and liver perforation model, OPAs achieved complete hemostasis and greatly reduced blood loss compared to commercial hemostat AGS. In the rabbit life-threatening hemorrhage model, OPA_4 effectively enabled hemostasis under hypertensive and high-flow conditions, significantly reducing blood loss than blank group. Critically, unlike permanent adhesives, gentle saline irrigation triggered the reconversion of aerogel into a hydrogel after hemostasis, attenuating hydrogen bonding interactions at the adherent interface with atraumatic removal. In addition, OPAs had broad-spectrum antimicrobial activity that reduced the risk of infection at the interface of injury and supported *in vivo* degradation. By integrating rapid hemostasis, on-demand removal, antibacterial efficacy and biodegradability, OPAs overcame the limitations of existing hemostats. OPAs achieved rapid hemostasis while enabling controlled and atraumatic removal, presenting a versatile strategy applicable to both emergency and surgical settings. Future studies should focus on large-animal trials and clinical translation to validate its efficacy in complex human wounds.

Received 17 July 2025; accepted 2 September 2025; published online 4 January 2026

1 Fisher AD, Bulger EM, Gestring ML. Stop the bleeding. JAMA, 2018, 320: 589
2 Holcomb JB, Moore EE, Sperry JL, *et al.* Evidence-based and clinically relevant outcomes for hemorrhage control trauma trials. Ann Surg, 2021, 273: 395–401
3 Eastridge BJ, Holcomb JB, Shackelford S. Outcomes of traumatic hemorrhagic shock and the epidemiology of preventable death from injury. Transfusion, 2019, 59: 1423–1428
4 Li XF, Lu P, Jia HR, *et al.* Emerging materials for hemostasis. Coord Chem Rev, 2023, 475: 214823
5 Guo B, Dong R, Liang Y, *et al.* Haemostatic materials for wound healing applications. Nat Rev Chem, 2021, 5: 773–791
6 Hickman DSA, Pawlowski CL, Sekhon UDS, *et al.* Biomaterials and advanced technologies for hemostatic management of bleeding. Adv Mater, 2018, 30: 1700859
7 Dong R, Zhang H, Guo B. Emerging hemostatic materials for non-compressible hemorrhage control. Natl Sci Rev, 2022, 9: nwac162
8 Zhu T, Wu J, Zhao N, *et al.* Superhydrophobic/superhydrophilic Janus fabrics reducing blood loss. Adv Healthcare Mater, 2018, 7: 1701086
9 Fang Y, Zhang Y, Qiu L, *et al.* Amphiphilic Janus cotton gauze with enhanced moisture management and blood coagulation for rapid hemostasis and wound healing. Int J Biol Macromol, 2024, 276: 133826
10 Du Y, Bai Y, Lang S, *et al.* Gelatin sponges with a uniform interoperable pore structure and biodegradability for liver injury hemostasis and tissue regeneration. Biomacromolecules, 2023, 24: 5313–5327
11 Wang C, Zhou H, Niu H, *et al.* Tannic acid-loaded mesoporous silica for rapid hemostasis and antibacterial activity. BioMater Sci, 2018, 6: 3318–3331
12 Liu C, Yao W, Tian M, *et al.* Mussel-inspired degradable antibacterial polydopamine/silica nanoparticle for rapid hemostasis. Biomaterials, 2018, 179: 83–95
13 Liang Y, Xu C, Li G, *et al.* Graphene-kaolin composite sponge for rapid and riskless hemostasis. Colloids Surfs B-Biointerfaces, 2018, 169: 168–175
14 Du F, A W, Liu F, *et al.* Hydrophilic chitosan/graphene oxide composite sponge for rapid hemostasis and non-rebleeding removal. Carbohydrate Polyms, 2023, 316: 121058
15 Wu B, Du F, A W, *et al.* Graphene-based hemostatic sponge. Chin Chem Lett, 2022, 33: 703–713
16 Li G, Quan K, Liang Y, *et al.* Graphene-montmorillonite composite sponge for safe and effective hemostasis. ACS Appl Mater Interfaces, 2016, 8: 35071–35080
17 Li J, Wu H, He X, *et al.* Silk fibroin aerogels with AIE-featured berberine and MXene for rapid hemostasis and efficient wound healing. Int J Biol Macromol, 2024, 283: 137629
18 Jin Z, Chen L, Liu X, *et al.* Zeolite firmly anchored regenerated cellulose aerogel for efficient and biosafe hemostasis. Int J Biol Macromol, 2025, 304: 140743
19 Montazerian H, Davoodi E, Baidya A, *et al.* Engineered hemostatic biomaterials for sealing wounds. Chem Rev, 2022, 122: 12864–12903
20 Guo Y, Wang M, Liu Q, *et al.* Recent advances in the medical applications of hemostatic materials. Theranostics, 2023, 13: 161–196
21 Pourshahrestani S, Zeimaran E, Kadri NA, *et al.* Polymeric hydrogel systems as emerging biomaterial platforms to enable hemostasis and wound healing. Adv Healthcare Mater, 2020, 9: 2000905
22 Peng X, Xu X, Deng Y, *et al.* Ultrafast self-gelling and wet adhesive powder for acute hemostasis and wound healing. Adv Funct Mater, 2021, 31: 2102583
23 Zhang K, Chen X, Xue Y, *et al.* Tough hydrogel bioadhesives for sutureless wound sealing, hemostasis and biointerfaces. Adv Funct Mater, 2022, 32: 2111465
24 Teng L, Shao Z, Bai Q, *et al.* Biomimetic glycopolypeptide hydrogels with tunable adhesion and microporous structure for fast hemostasis and highly efficient wound healing. Adv Funct Mater, 2021, 31: 2105628
25 Li M, Zhang M, Liu Z, *et al.* Injectable and self-fused hydrogels with antifouling capability based on amino acid derivatives for postoperative anti-adhesion application. Sci China Mater, 2024, 67: 1521–1532
26 Meng X, Xiao X, Jeon S, *et al.* An ultrasound-driven bioadhesive triboelectric nanogenerator for instant wound sealing and electrically accelerated healing in emergencies. Adv Mater, 2023, 35: 2209054
27 He J, Zhang Z, Yang Y, *et al.* Injectable self-healing adhesive pH-responsive hydrogels accelerate gastric hemostasis and wound healing. Nano-Micro Lett, 2021, 13: 80
28 Shi T, Xiong YH, Song W, *et al.* Polysaccharide-based antibacterial nanocomposite hydrogels with Janus structure for treatment of infected extraction socket. Sci China Mater, 2024, 67: 2550–2557
29 Zhang Z, Zhang Y, Liu Y, *et al.* Water-retaining and separable adhesive hydrogel dressing for wound healing without secondary damage. Sci China Mater, 2023, 66: 3337–3346
30 Liu C, Liu X, Liu C, *et al.* A highly efficient, *in situ* wet-adhesive dextran derivative sponge for rapid hemostasis. Biomaterials, 2019, 205: 23–37
31 Lv C, Zhou X, Wang P, *et al.* Biodegradable alginate-based sponge with antibacterial and shape memory properties for penetrating wound

 © Science China Press 2026

hemostasis. Compos Part B-Eng, 2022, 247: 110263
32 Liu C, Shi Z, Sun H, *et al.* Preparation and characterization of tissue-factor-loaded alginate: toward a bioactive hemostatic material. Carbohydrate Polyms, 2020, 249: 116860
33 Wei X, Ding S, Liu S, *et al.* Polysaccharides-modified chitosan as improved and rapid hemostasis foam sponges. Carbohydrate Polyms, 2021, 264: 118028
34 Yang E, Hou W, Liu K, *et al.* A multifunctional chitosan hydrogel dressing for liver hemostasis and infected wound healing. Carbohydrate Polyms, 2022, 291: 119631
35 Bian S, Hao L, Qiu X, *et al.* An injectable rapid-adhesion and anti-swelling adhesive hydrogel for hemostasis and wound sealing. Adv Funct Mater, 2022, 32: 2207741
36 Weng H, Jia W, Li M, *et al.* New injectable chitosan-hyaluronic acid based hydrogels for hemostasis and wound healing. Carbohydrate Polyms, 2022, 294: 119767
37 Yang X, Wang X, Gao X, *et al.* What else should hemostatic materials do beyond hemostasis: a review. Mater Today Bio, 2024, 25: 101008
38 Keast D, Janmohammad A. The hemostatic and wound healing effect of chitosan following debridement of chronic ulcers. Wounds, 2021, 33: 263–270
39 Chiara O, Cimbanassi S, Bellanova G, *et al.* A systematic review on the use of topical hemostats in trauma and emergency surgery. BMC Surg, 2018, 18: 68
40 Bottosso S, Pasquali S, Ricci R, *et al.* Surgical debridement in wound care. In: Maruccia M, Papa G, Ricc E, *et al.* (eds.). Pearls and Pitfalls in Skin Ulcer Management. Cham: Springer International Publishing, 2024. 429–437
41 Yu P, Zhong W. Hemostatic materials in wound care. Burns Trauma, 2021, 9: tkab019
42 Spaziani E, Di Filippo A, Francioni P, *et al.* Subhepatic mass occurrence after using oxidized and regenerated cellulose polymer in laparoscopic cholecystectomy: a case series. Acta Chirurgica Belgica, 2018, 118: 48–51
43 Nam KH, Lee JH, Chung YS, *et al.* The efficacy of oxidized regenerated cellulose (SurgiGuard®) in breast cancer patients who undergo total mastectomy with node surgery: a prospective randomized study in 94 patients. PLoS ONE, 2022, 17: e0267694
44 Huang Y, Zhao X, Wang C, *et al.* High-strength anti-bacterial composite cryogel for lethal noncompressible hemorrhage hemostasis: synergistic physical hemostasis and chemical hemostasis. Chem Eng J, 2022, 427: 131977
45 Huang H, Liao S, Zhang D, *et al.* A macromolecular cross-linked alginate aerogel with excellent concentrating effect for rapid hemostasis. Carbohydrate Polyms, 2024, 338: 122148
46 Wang Y, Guo Y, Liu Y, *et al.* Platelet vesicles synergetic with biosynthetic cellulose aerogels for ultra-fast hemostasis and wound healing. Adv Healthcare Mater, 2024, 13: 2304523
47 Luo Z, Wang Y, Li J, *et al.* Tailoring hyaluronic acid hydrogels for biomedical applications. Adv Funct Mater, 2023, 33: 2306554
48 Xu Q, Torres JE, Hakim M, *et al.* Collagen- and hyaluronic acid-based hydrogels and their biomedical applications. Mater Sci Eng-R-Rep, 2021, 146: 100641
49 Kotla NG, Mohd Isa IL, Larrañaga A, *et al.* Hyaluronic acid-based bioconjugate systems, scaffolds, and their therapeutic potential. Adv Healthcare Mater, 2023, 12: 2203104
50 Cai B, Fan Y, Yang S, *et al.* A highly compressible and expandable cellulose sponge with arch-like lamellar structures for non-compressible hemorrhage. Carbohydrate Polyms, 2025, 353: 123255
51 Lei XX, Liu ML, Lu CF, *et al.* A self-hygroscopic, rapidly self-gelling polysaccharide-based sponge with robust wet adhesion for non-compressible hemorrhage control and infected wounds healing. Bioactive Mater, 2025, 46: 311–330
52 Wu Y, Chen X, Song P, *et al.* Functional oxidized hyaluronic acid cross-linked decellularized heart valves for improved immunomodulation, anti-calcification, and recellularization. Adv Healthcare Mater, 2024, 13: 2303737
53 Lozinsky VI. Cryostructuring of polymeric systems. 50.† Cryogels and cryotropic gel-formation: terms and definitions. Gels, 2018, 4: 77
54 Chen Y, Zhou L, Chen L, *et al.* Anisotropic nanocellulose aerogels with ordered structures fabricated by directional freeze-drying for fast liquid transport. Cellulose, 2019, 26: 6653–6667
55 Casa LDC, Deaton DH, Ku DN. Role of high shear rate in thrombosis. J Vascular Surg, 2015, 61: 1068–1080
56 Murray JS, Politzer P. Molecular electrostatic potentials and non-covalent interactions. WIREs Comput Mol Sci, 2017, 7: e1326
57 Li J, Celiz AD, Yang J, *et al.* Tough adhesives for diverse wet surfaces. Science, 2017, 357: 378–381
58 Frost SJ, Mawad D, Higgins MJ, *et al.* Gecko-inspired chitosan adhesive for tissue repair. NPG Asia Mater, 2016, 8: e280
59 Hladílková J, Fischer HE, Jungwirth P, *et al.* Hydration of hydroxyl and amino groups examined by molecular dynamics and neutron scattering. J Phys Chem B, 2015, 119: 6357–6365

Acknowledgement This work was supported by the Key Program of Beijing Natural Science Foundation (Z200025), the National Natural Science Foundation of China (52273118, 22275013), the Innovation & Transfer Fund of Peking University Third Hospital (BYSYZHKC123, BYSYZHKC107), and the Fundamental Research Funds for the Central Universities (PY2508, QNTD2023-01).

Author contributions Huang L developed, organized the study, and wrote-reviewed & edited the manuscript; Zhang Q assisted in materials preparation and measurement and data analysis; Du F helped with data analysis and provided assistance for materials preparation and measurement; Liu Z, Qiu L, and Wei Y provided assistance for materials preparation; Xie W guided the study; Li G designed, guided the study, and wrote-reviewed & edited the manuscript; Kong D guided the study; Wang X designed, guided, funded the study, and wrote-reviewed & edited the manuscript. All authors discussed the results and commented on the manuscript.

Conflict of interest The authors declare that they have no conflict of interest.

Supplementary information Supplementary materials are available in the online version of the paper.



Lifei Huang is studying for her PhD degree at Beijing Laboratory of Biomedical Materials, Beijing University of Chemical Technology. Her current research focuses on the synthesis of polysaccharide-based hydrogels for biomedical applications.



Guofeng Li received his PhD degree from Beijing University of Chemical Technology. After working as a visiting fellow in the Chemical Engineering Department, the University of New South Wales (UNSW), Australia, he first worked as a postdoc and then joined the College of Life Science and Technology, Beijing University of Chemical Technology as an associate professor in 2021. His research interests primarily focus on the development of hemostatic materials, polymer materials, and antibacterial materials.



Dongsheng Kong is an attending physician in the Department of Neurosurgery, the First Medical Center of the PLA General Hospital. He focuses on new diagnostic technologies and treatments for cranial and brain battle trauma, with in-depth research on rapid rescue for cerebrovascular injuries.

© Science China Press 2026



Xing Wang received his PhD degree in polymer chemistry and physics at Jilin University. After post-doctoral research at Münster University, Germany, he joined Beijing University of Chemical Technology with the talent honor. Now he is a full professor and doctoral supervisor in the College of Life Science and Technology. His research interests mainly focus on biomedical polymer materials, including antimicrobial polymers, hemostasis, and drug delivery system.

强黏性透明质酸/ε-PL气凝胶用于危及生命的动脉出血的快速止血和按需无创清除

黄丽霏[1], 张全睿[1], 杜芳林[1], 刘芝涵[1], 邱琳雯[1], 魏一鸣[1], 谢文升[1], 李国锋[1*], 孔东生[2*], 王兴[1*]

摘要 有效处理创伤性出血不仅需要快速止血，还应便于清除止血材料以减少二次组织损伤. 基于氧化透明质酸(OHA)和ε-聚赖氨酸(ε-PL)席夫碱交联, 我们制备了一种强黏附性气凝胶(OPAs), 可在致命性动脉创伤中快速止血, 并按需去除. OPAs孔隙率可调、吸血迅速, 表面丰富的羟基、氨基和羧基增强与组织、血细胞和蛋白的相互作用，促进组织黏附、血小板捕获和活化. 在兔股动脉损伤模型中，OPA_4使止血时间缩短约80%, 失血量减少38%. 水化后OPAs黏附力降至2%, 便于去除. OPAs还具有抗菌性、生物相容性和可降解性，其一步冷冻干燥制备工艺和可定制形态支持规模化生产和多功能应用. 这项研究提出了一种结合快速止血和无创去除的多功能策略，有望改善预后并简化术后处理.

© Science China Press 2026

International Journal of Biological Macromolecules 313 (2025) 144187

Contents lists available at ScienceDirect

International Journal of Biological Macromolecules

journal homepage: www.elsevier.com/locate/ijbiomac

Beyond thermal protection: Injectable self-healing chitosan hydrogel in liver tumor thermal ablation

Lifei Huang [a], Erpeng Qi [b], Zhihan Liu [a], Quanrui Zhang [a], Shuo Wang [a], Shaowei Zheng [a], Wensheng Xie [a], Guofeng Li [a], Xue Chen [a], Hui Sun [b,c,*], Fangyi Liu [b,**], Xing Wang [a,**]

[a] State Key Laboratory of Organic-Inorganic Composites, Beijing Laboratory of Biomedical Materials, Beijing University of Chemical Technology, Beijing 100029, China
[b] Department of Interventional Ultrasound, The Fifth Medical Center, Chinese PLA General Hospital, Beijing 100853, China
[c] Department of Hepatology, Tongliao Sixth People's Hospital, Tongliao 028000, China

ARTICLE INFO

Keywords:
Self-healing chitosan hydrogel
Thermal ablation
Hemostasis
Anti-tumor metastasis
Anti-tissue adhesion

ABSTRACT

Thermal ablation technology is crucial for treating early-stage primary tumors. However, the "water isolation" during clinical surgery is limited by unstable thermal protection caused by fluid loss. More seriously, it is prone to intraoperative bleeding, cancer cell metastasis, and postoperative tissue adhesion. Here we introduce a "one stone, four birds" strategy, which utilizes a self-healing chitosan hydrogel without drug assistance to offer four abilities, including thermal protection, hemostasis, anti-tumor metastasis and anti-tissue adhesion. A rabbit VX2 liver transplantation tumor model is established. The self-healing chitosan hydrogel, crosslink of hydroxyethyl chitosan (HC) and dual aldehyde-PEG (Ald-PEG-Ald) using dynamic Schiff base, adheres to the liver surface and remains *in situ* upon minimally invasive injection, resulting in outstanding thermal protection compared with saline. The temperature of the isolated tissue near the ablation foci remains below 42 °C. Moreover, the self-healing property of the hydrogel can prevent cell leakage during the procedure, thus avoiding intraoperative bleeding, tumor metastasis and postoperative abdominal adhesion. Therefore, this work identified four efficacies of the self-healing chitosan hydrogel in thermal ablation of metastatic liver tumors, providing an advanced alternative for clinical application.

1. Introduction

Thermal ablation is a crucial therapeutic technique in interventional oncology, especially for early primary tumors and oligometastatic tumors (those with three or fewer lesions) with minimal invasiveness and high technical success rate [1–5]. Currently, the mature thermal ablation technologies include Radiofrequency Ablation (RFA) [6,7], Microwave Ablation (MWA) [7,8], Laser-Induced Interstitial Thermotherapy (LITT) [9], and Cryotherapy [10]. Among them, MWA is superior for large tumors, locations around large vessels, and high perfusion areas with limited radiofrequency power [8]. Microwave energy generates faster heating and higher temperatures, leading to broader areas of necrosis [11–15]. Additionally, better defined ablation areas can be yielded in the MWA [16]. Despite MWA currently being considered an effective technique for local tumor treatment, postoperative complications such as pain, bleeding, tumor metastasis, tissue adhesion and infection are inevitably encountered [6,17–21]. Zensen et al. collectively analyzed 7228 cases of liver tumor ablation from 136 centers in Germany and Austria, revealing an overall complication rate of 3.0 % (214/7228) [22].

In clinical thermal ablation, adjunctive thermoprotective agents are often required to safeguard surrounding healthy tissue. The "water isolation" technique is commonly employed to reduce potential damage to nearby structures and minimize complications [23–28]. Saline or 5 % glucose solution is injected between the target lesion and adjacent tissues or organs to shield them from potential thermal injury [29,30]. However, its drawbacks are susceptibility to volume loss and unstable thermal protection effect. Since continuous injections are required, posing potential risks such as edema and electrolyte imbalances. Consequently, there is a pressing need in clinic for superior options to saline to implement better protection. Recent studies have developed several thermal protection hydrogels and evaluated its feasibility as substitutes for traditional liquids [31–36]. Ren et al. developed a hyaluronic acid-based hydrogel (HA-Dc) and exhibited thermal protection

* Correspondence to: H. Sun, Department of Interventional Ultrasound, The Fifth Medical Center, Chinese PLA General Hospital, Beijing 100853, China.
** Corresponding authors.
E-mail addresses: SunHuiTL@163.com (H. Sun), fangyi0317@163.com (F. Liu), wangxing@mail.buct.edu.cn (X. Wang).

https://doi.org/10.1016/j.ijbiomac.2025.144187
Received 6 March 2025; Received in revised form 8 May 2025; Accepted 12 May 2025
Available online 14 May 2025
0141-8130/© 2025 Elsevier B.V. All rights are reserved, including those for text and data mining, AI training, and similar technologies.

performance for thermal ablation [37]. While complications associated with clinical tumor ablation extend beyond thermal damage, encompassing potential issues such as bleeding, adhesions and tumor implantation, which require a systematic assessment.

For this purpose, we proposed a treatment strategy of "one stone, four birds" in this study, that is, utilizing an injectable self-healing chitosan hydrogel to evaluate the comprehensive effect of thermal ablation therapy of the hydrogel in the established rabbit VX2 highly metastatic liver tumor model. The specific self-healing chitosan hydrogel is formed based on the dynamic Schiff base between biocompatible Hydroxyethyl Chitosan (HC) and dual aldehyde-PEG (Ald-PEG-Ald), which endows the chitosan hydrogel injectability and shape adaptability. We aimed to achieve multiple goals with one intervention: the injectable self-healing chitosan hydrogel for thermal protection, hemostasis, anti-metastasis and anti-adhesion in tumor thermal ablation (Scheme 1). Compared with saline, the self-healing chitosan hydrogel exhibits superior *in-situ* retention. Its self-healing properties facilitate rapid healing of hydrogel gaps formed during surgical procedures, thus blocking the leakage of blood cells and tumor cells, then inhibiting tumor metastasis and potential postoperative tissue adhesion. We believe that this self-healing chitosan hydrogel holds significant advances in clinical adjunctive MWA treatment, not only effective for existing early-stage oligometastatic tumors, but also applicable to high metastatic tumors.

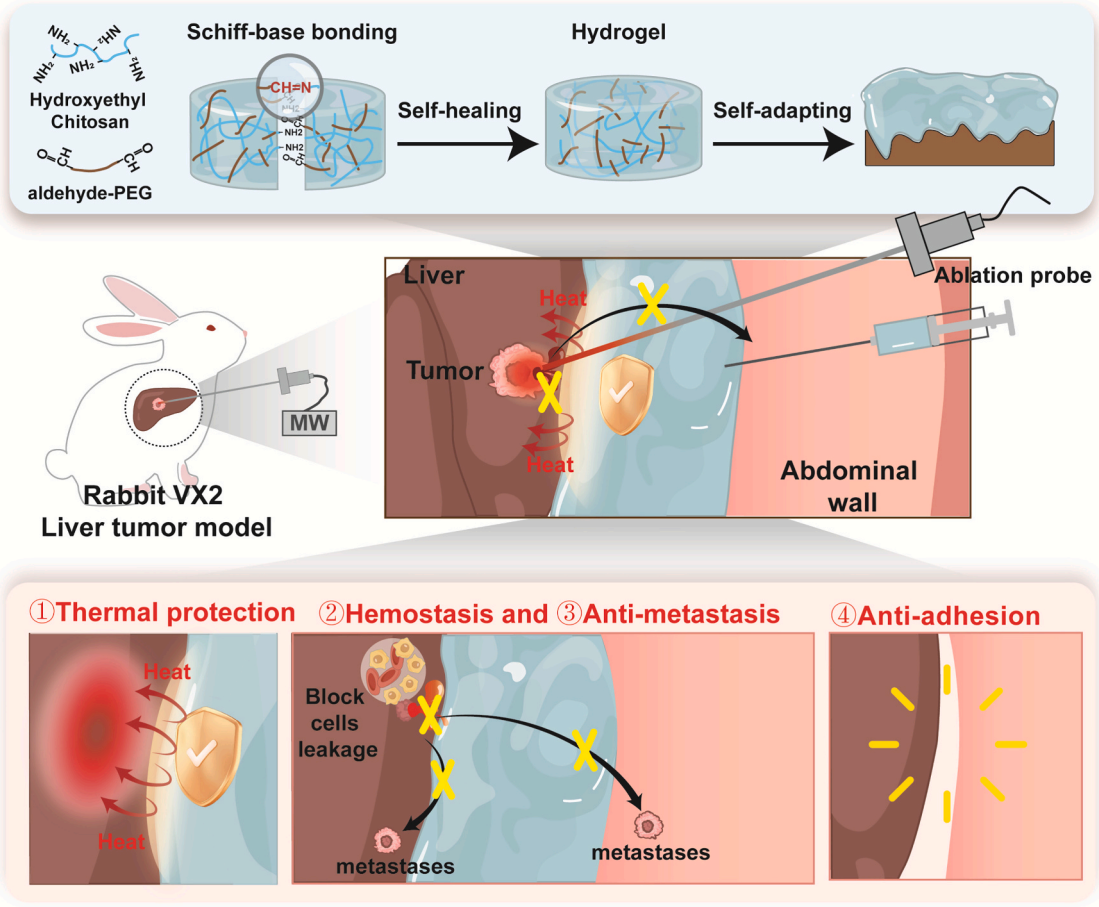
2. Materials and methods

2.1. Materials

Hydroxyethyl Chitosan (HC, 82 kDa, Wako Pure Chemical Industries, Ltd., Japan). Dual aldehyde-PEG (Ald-PEG-Ald, Mn ≈ 4000 g/mol) was prepared according to the experimental protocol reported [38]. L929 cells were acquired from Servicebio Co., Ltd. (Wuhan, China). RPMI 1640 medium (RPMI 1640), penicillin-streptomycin (PS) and trypsin were purchased from Gibco Life Technologies (Beijing, China). Fetal bovine serum (FBS) was purchased from Sigma. All solvents were purchased from Sinopharm Chemical Reagent and used directly without further purification. The animal experiments were performed using rabbits weighing 3.5–4.2 kg, which were provided by Beijing Jinmuyang Experimental Animal Breeding Co., Ltd. The experimental animal protocols were carried out following Beijing (China) Animal Experiment Guidelines (2010) and were authorized by the ethics committee of The Fifth Medical Center, Chinese PLA General Hospital (Approve number: 2023-X-19-91).

2.2. Preparation and microstructure analysis of the hydrogel

2.5 % hydrogel was prepared by mixing 3 mL 3 % HC with 1 mL 1 % Ald-PEG-Ald solutions at room temperature. The sol-gel transition was confirmed when no visual flow was observed after tilting the vial for 30 s, with Acid Orange 7 used to stain the hydrogel for visualization. To observe the microstructure, the hydrogel was freeze-dried to obtain dry



Scheme 1. Schematic illustration of the structure of self-healing chitosan hydrogel and the protocol: using a self-healing chitosan hydrogel for thermal protection, hemostasis, anti-metastasis, and anti-adhesion.

hydrogel sample. The sample were gold-plated and then imaged using a scanning electron microscope (SEM) (ZEISS, Supra 55, German) with an accelerating voltage of 5 kV.

2.3. Rheological analysis and injectability

The shear thinning behavior of hydrogel was assessed using a TA rotational rheometer (TA Discovery HR 30, USA). Tests were carried out on parallel plates with a diameter of 16.5 mm. The stability of the hydrogel was determined by frequency sweep tests at 25 °C, 1 % constant strain, and a frequency of 0.1–100 rad/s. The strain sweep tests were determined at 1 % rad/s, and a strain range of 1 %–1000 %. The step strain of the hydrogel was determined by the sequential passage through 1 %, and 600 % strain at a frequency of 1 rad/s for successive periods of 180 s. Additionally, the injectability of the hydrogel (stained with Acid Orange 7) was determined by injection using a 1 mL syringe (Needle 26G).

2.4. Adhesion property

The different substrates (nitrile gloves, petri dish, glass, liver) were used to assess the adhesion properties of the hydrogel.

2.5. Self-healing property

The hydrogel was extruded from the syringe to form a shattered structure and the healing behavior of the hydrogel was observed over a period of time. Photographs were taken to record their self-healing behavior.

2.6. Hemolysis experiment

Gradient concentration dispersions were prepared by dissolving the hydrogel powder with PBS and ultrasonication for 2 h. 1 mL of blood was added to 2 mL of PBS and centrifuged at 500 g for 10 min, followed by de-conditioning of the supernatant to 10 mL (RBC solution). 0.2 mL of the above-treated RBCs were added to 0.8 mL of the different concentrations of dispersions. The samples were incubated for 3 h at 37 °C followed by centrifugation for 5 min at 10,000 g. The mixture of PBS and deionized water with RBCs was used as negative and positive control. The absorbance values were then measured at 540 nm. The hemolysis rate was calculated according to the following formula:

$$Haemolysis\ rate\ (\%) = (ODsample - ODnegative)/(ODpositive - ODnegative) \times 100\%$$

2.7. Degradation performance

For the *in vitro* hydrogel degradation test, each set was processed with PBS at 37 °C, and the degradation performance of the hydrogel was evaluated by the weight loss method. The samples were removed at a set time, dried with filter paper and weighed. The experiment was repeated three times. The *in vivo* degradation of hydrogel was assessed *via* ultrasound. Under ultrasound guidance, 4 ml of hydrogel was injected around the thyroid gland of Beagle dog, bypassing structures such as blood vessels, trachea and nerves in the neck. After injection, a distinct hypoechoic region was produced on the ultrasound image. This region was then observed and recorded daily over a seven-day period to track the degradation of hydrogel.

2.8. Biosafety assay

The CCK-8 assay was used to assess the cell viability to detect the *in vitro* toxicity of the hydrogel. L929 cells were cultured in 96-well plates with 1×10^4 cells/well. The 3 % HC and 1 % Ald-PEG-Ald solution were added to the well plates. For 2.5 % hydrogel, the original medium was removed and 100 μL of the mixed hydrogel precursor solution was added to each well. The plate was left for approximately 10 min to allow complete gelation. Then, 50 μL of liquid culture medium was added on top of each gel to ensure nutrient exchange. Subsequently, the cells were placed in a cell culture incubator for co-incubation. After adding 10 μL of CCK-8, each sample was incubated for 3 h, and then the absorbance at 450 nm was measured.

2.9. In vitro sealing test

The ability to seal blood vessels of the hydrogel was assessed by sealing testing assay [39]. A collagen cannula (diameter: 16 mm) was used as a tissue matrix. A digital manometer (HANDPI, HP-10) was attached to the end of the collagen casing for pressure measurement. Initially, PBS was filled with collagen casings until the pressure reached 70 mmHg. Then, the hydrogel was adhered to the collagen casing, which was subsequently punctured with needles of different gauges (Needle 26G and 22G) against the underside to simulate blood loss. Pressure changes were recorded by a digital manometer.

2.10. Thermal analysis of the hydrogel

A copper block with heater was used to generate a stable uniform high-temperature surface (the top of the block). A hydrogel cube with dimensions of 20 mm × 20 mm was placed on the top of the cooper block. The hydrogel cube was surrounded by insulating material on all sides to minimize heat loss and ensure one-dimensional heat conduction. Four thermocouples (Omega, TT-T-36-SLE) were used to measure the block surface temperature and hydrogel inner temperatures. The distance between monitoring points 1 and 2 was set at 7 mm, between points 2 and 3 was 5 mm, with points 3 and 4 being identical. The thermal conductivity of the hydrogel can be calculated according to Fourier's law (1).

$$Q = A\lambda\, dT/dx \tag{1}$$

Dynamic thermography was employed to visually assess heat transfer in the hydrogel and saline. The hydrogel was formed in a petri dish and a central hole was created, with the diameter of the hole matching that of the iron block. The iron block, preheated to 120 °C, was placed into the artificial holes and thermal images were recorded using an infrared camera. The saline control group underwent the identical procedure.

2.11. Construction of rabbit VX2 transplanted liver tumor model

The VX2 tumor was made into a suspension and injected about 1 mL into the muscle of the lateral thigh of rabbits [40–42]. After 1 week, anesthetize tumor bearing rabbits with a dose of Midazolam Injection (Jiangsu Nhwa Pharmaceutical Co., Ltd.): Cyperazine Hydrochloride Injection (Jilin Huamu Animal Health Products Co., Ltd) =1:1, 0.10 mg/kg, the leg tumor tissues were peeled off under aseptic conditions. The greyish-white fish-like tissue at the edge of the tumor was clipped if possible, and then the tumor mass was sheared into tissue pieces about 1

to 2 mm in diameter. After the experimental rabbits were fully anaesthetized, their limbs were fixed and the skin was prepared, a longitudinal incision of about 3 cm in length was made layer by layer at the xiphoid process along the midline of the abdomen. The liver was grasped with toothless forceps and raised into the abdominal cavity, the liver tissue was punctured with ophthalmic forceps in the thicker left central lobe of the liver, 2 pieces of the clipped tumor were implanted in it. The needle was removed and immediately compressed with a gelatin sponge block. After confirming that no significant bleeding occurred, the liver was retracted into the abdominal cavity and closed layer by layer with abdominal sutures. Subsequently, the incision was cleaned with povidone-iodine, and penicillin was injected intramuscularly with 200,000 U/kg once a day after the operation.

2.12. In vivo percutaneous liver tumor ablation protocol

After anesthesia, the rabbits were placed in the supine position. A 1–2 mm cut was made into the skin of rabbit with a sharp knife and the microwave antenna was placed at the site indicated by the ultrasound. Saline or hydrogel was injected using a 20 mL syringe (needle: 22G) to provide an isolation zone. The total injection volume of normal saline accumulated to 15 mL before and during ablation, whereas the hydrogel required only a single injection of 4 mL before ablation. The ablation was performed for 2 min at 20 W microwave power output using a MWA therapist (KY-2000, Nanjing Kangyon Medical Technology Co., Ltd.). Based on the size of the tumor, 2–3 MWA treatment cycles (20 W, 2 min) are usually required. Doppler ultrasound was used to monitor the ablation process throughout the procedure, and the temperature during ablation were recorded. Postoperatively, 200 mL of saline was injected into the abdominal cavity of rabbits, and the ascites was collected after 15 min for blood count and free tumor cells count. Blood cell counts were performed by a hematology analyzer (Mindray, China). Meanwhile, tumor cells were labeled with 7-AAD dye (Beyotime, China) and subsequently observed using fluorescence confocal. All rabbits underwent postoperative ultrasonography to assess tumor metastasis after percutaneous ablation of liver tumors.

Since the *in vivo* degradation time of the hydrogel is within 7 days, the animals were sacrificed on day 6 to examine remaining hydrogel and harvest both target and non-target tissues from the thermal injury regions. Then, photographs were taken to describe the areas of ablative damage and areas of adhesions on the tissue. The adhesion levels were recorded according to the adhesion scoring criteria system. Score 0, no adhesions; score 1, 1 thin layer of adhesions; score 2, >1 thin layer of adhesions; score 3, thicker adhesions to the focal point; score 4, thicker adhesions attached to the pedicle, which can be separated with strong blunt dissection; score 5, very thick vascular adhesions, which require sharp dissection. Blood was collected on day 1, 4 and 6 postoperatively and samples was used for aspartate aminotransferase (AST), alanine aminotransferase (ALT), alkaline phosphatase (ALP), blood urea nitrogen (BUN) and creatinine (CREA) measurements to assess liver and kidney function. All procedures were performed by clinically experienced interventional ultrasonographers.

2.13. Animal sampling and histological examination

After the animals were sacrificed on day 6, normal and heat-damaged abdominal tissues, metastatic tumor tissues, and adherent tissues of rabbits were harvested and fixed in 4 % paraformaldehyde (PFA) solution. Tissue samples were further embedded in paraffin and subjected to hematoxylin and eosin (H&E) staining, Masson staining, Ki67 and MMP2 immunostaining evaluation to assess tissue damage. Sections were visualized with a Leica microscope.

2.14. ELISA assay

Different groups of abdominal wall tissue samples were added to 9 times the volume of homogenization medium. The 10 % homogenate was prepared by mechanical homogenization under ice water bath conditions. Subsequently centrifuged at 2500–3000 rpm for 10 min and the supernatant was taken for assay. TNF-α, IL-6, IL-4, and IL-10 levels in the tissues were measured using the relevant Rat ELISA Kit (Cloud-clone CORP. Wuhan, China). The saline-treated group was used as a positive control for the thermal injury response, and the hydrogel-treated group was used as the experimental group. All experiments were repeated three times.

2.15. Quantitative Rea-time PCR (qPCR) assay

To assess the extent of thermal injury to the abdominal tissues and abdominal adhesions after surgery, the mRNA levels of heat shock protein HSP70 in the locally injured tissues and TNF-α in the adherent tissues were examined. The experimental methods are as follows: An 80–100 mg of abdominal tissue from the thermal injury site was harvested. Total RNA was extracted with 1 mL Trizol reagent and cDNA was synthesized by reverse transcription using a reverse transcription kit (Servicebio, China). A reaction system containing cDNA, 2.5 μM gene-specific primers, 2× SYBR, and Water Nuclease-Free was assayed using a real-time fluorescence quantitative PCR instrument (Bio-rad, USA). GAPDH was used as the housekeeping gene and gene expression changes were calculated by the $2^{-\Delta\Delta CT}$ assay. The control group (tissue not treated for thermal injury) was used as a normalized baseline. The relevant primer sequences are as follows: The TNF-α primer sequences were 5′-CGTAGTAGCAAACCCGCAAGT-3′ and 5′-ACCTTGTTCGGGTAGGAGACG-3′; for HSP70 were 5′-AA-GCCAGACGACAATCAGGA-3′ and 5′-CATGGCTGCAAGAACCTC-TG-3′; for GAPDH were 5′-TTCCAGTATGATTCCACCCACG-3′ and 5′-GGGCTGAGATGATGA- CCCTTTT-3′.

2.16. Statistical analysis

Statistical analysis was performed by GraphPad Prism 8.0 and Microsoft Excel. Group differences were assessed using Student's *t*-test or one-way analysis of variance (ANOVA). Statistical significance was defined as $^{*}p < 0.05$, $^{**}p < 0.01$, and $^{***}p < 0.001$.

3. Results and discussion

3.1. Characterization of the hydrogel

For the self-healing chitosan hydrogel utilized in this study, HC, with a heavy average molecular weight of about 163,481 g/mol (Fig. S1), contributes the polymer backbone of the hydrogel, and the cross-linking reaction is a typical Schiff base reaction. The sol-gel transition occurs upon complete mixing of HC and Ald-PEG-Ald solutions, transforming the transparent liquid into a homogeneous hydrogel (Fig. 1a). The reaction conditions are mild and easy to prepare large quantities samples. The hydrogel can be extruded from a 1 mL syringe (Fig. 1b). Syringe shear dilutes the hydrogel, temporarily disrupting its structure, which then self-heals into a complete disc after 30 min (Fig. 1c). The hydrogel exhibits a porous morphology that facilitates the transfer and diffusion of nutrients and therapeutic agents across tissues (Fig. 1d). Oscillatory frequency sweep tests revealed a mechanical strength of 266 Pa for the hydrogel (Fig. 1e). Oscillatory strain tests meant that the hydrogel disintegrated its hydrogel morphology at high strain (>600 %, Fig. S2). Then, the step strain sweep tests confirmed its self-healing capability that the hydrogel could be restored under low strain (1 %) after disintegration under high strain (600 %, Fig. 1f). Such reversible connections can facilitate adaptation to dynamic and complex local environments. It also shows good adhesion to various synthetic materials and organs, such as nitrile gloves, petri dish, glass, and liver (Fig. 1g), allowing to serve as a protective barrier by adhering to the surface of the organs after injection.

The hemolysis rate of the hydrogel was found to be <1 % for all

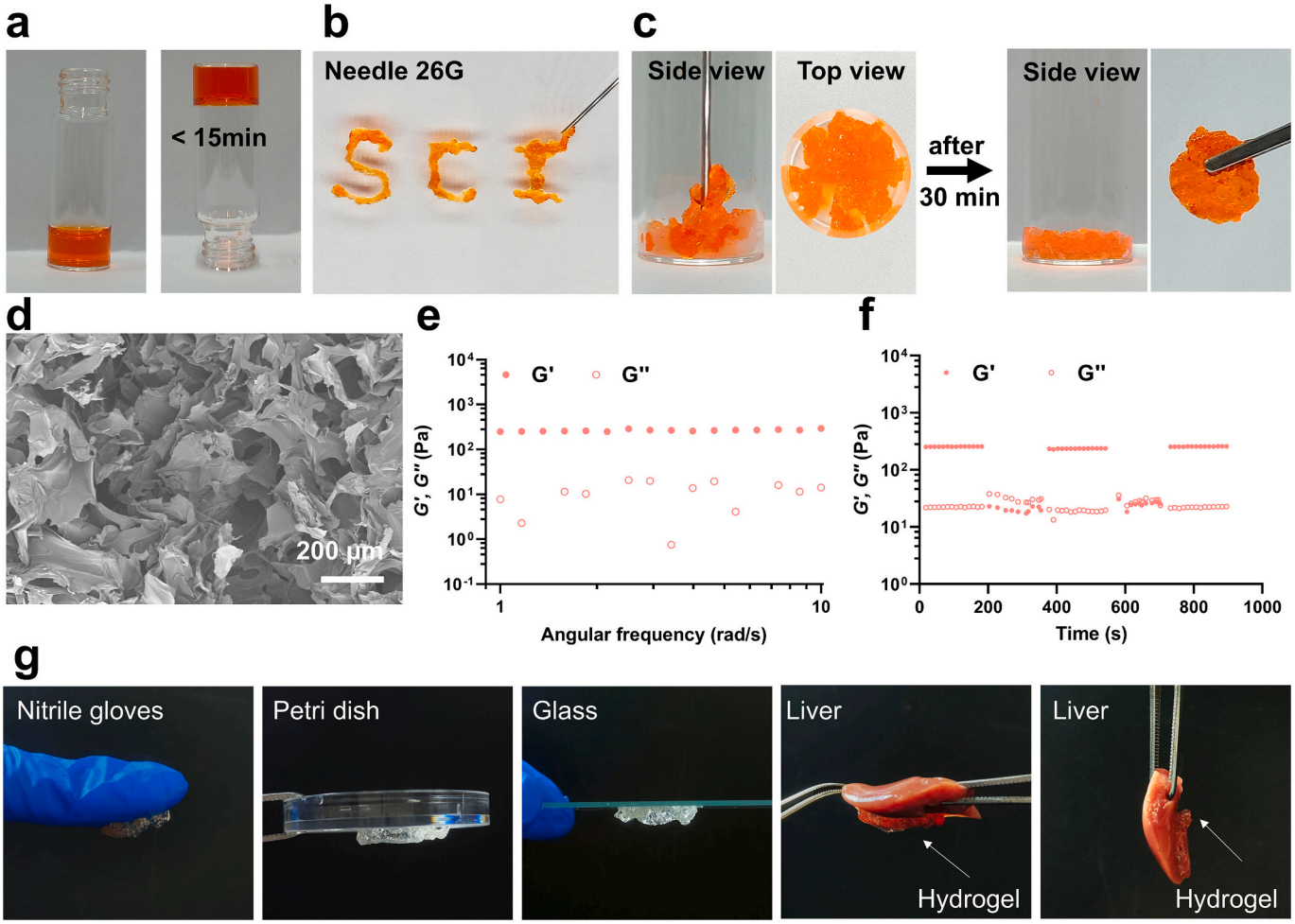


Fig. 1. Characterization of the hydrogel. (a) The formation of the hydrogel was observed by inversion of the vials. (b) Injection properties, (c) Macroscopic self-healing properties. (d) SEM images showing the microstructure of hydrogel. (e) Storage modulus G' and loss modulus G" of the hydrogel. (f) Oscillatory step-strain sweep tests of hydrogel. (g) Adhesion of the hydrogel to different substrates.

samples, which is well below the 5 % threshold for blood-contact materials in accordance with the international standard (ISO/TR7405) (Fig. S3). Cytotoxicity tests using the CCK-8 assay showed that the cell viability for both 1 % Ald-PEG-Ald solution, 3 % HC solution and 2.5 % hydrogel was above 80 % (Fig. S4), suggesting high cytocompatibility. Further, the hydrogel was sufficiently degraded within 40 h in a PBS environment simulating peritoneal ascites (Fig. S5), demonstrating rapid metabolism without burden to the organism. Furthermore, the *in vivo* degradation of the hydrogel was monitored by ultrasound (Fig. S6). The results showed that the hydrogel formed a hypoechoic region (d1:1 cm, d2:2.34 cm) around the thyroid gland on day 1. The hypoechoic region was seen to narrow significantly (d1:0.62 cm, d2:1.07 cm) on day 4. Eventually on day 7, no hypoechoic areas were observed, indicating that the hydrogel could be degraded within 7 days *in vivo*. Hence, the hydrogel is blood-compatible, non-cytotoxic, and degrade rapidly both *in vitro* and *in vivo*, supporting its safety and efficacy for *in vivo* applications.

3.2. *Thermal protection of the hydrogel in percutaneous ablation of tumors*

The thermal insulation efficacy was evaluated in an *in vivo* rabbit VX2 liver tumor model. Fig. 2a presents a schematic of the MWA protocol. The volume and morphology of VX2 transplanted liver tumors in rabbits were assessed using ultrasonography (US). Ultrasound images reveal a regular, spherical tumor shape in a diameter of 1.69 cm, with low blood flow within the tumor and abundant peripheral blood flow (Fig. 2b, Fig. S7). During percutaneous tumor ablation, saline (Video 1) and hydrogel (Video 2) were injected separately as physical barriers to provide thermal protection to the tissue around the ablation foci. A separation distance of 7.0 mm was achieved by injecting 4 mL of hydrogel, compared with only 3.6 mm after 15 mL of saline injection. The hydrogel achieves approximately 2-fold higher separation distances than saline *in vivo*, while requiring only 27 % volume fraction (Fig. S8, Video 3, Video 4). The area of the isolation zone formed by saline was about 0.99 cm^2, and the area of hydrogel was about 1.11 cm^2 (Fig. 2c, Fig. 2d). During the procedure, the area of saline was reduced to 0.98 cm^2, requiring constant replenishment and adding complexity to the surgical procedure. In contrast, the area of the hydrogel was reduced to 1.05 cm^2, and only 4 mL of hydrogel was injected at once before the operation without additional replenishment, greatly reducing the operation complexity. The hydrogel remains stable before, during and immediately after ablation, demonstrating excellent retention at the focal site. During the procedure, saline carried away part of the heat. However, the monitoring temperature of the abdominal wall tissue exceeded 55 °C with raised risk of abdominal wall injury and post-operative adhesions. (Fig. 2e). The temperature of the abdominal wall was controlled below 42 °C in the hydrogel group. There is virtually no thermal damage to the tissue at this temperature which confirmed by temperature monitor. The saline group gradually increased temperature with ablation time, while the hydrogel group stabilized at approximately 42 °C within 2 min of ablation (Fig. 2f). Thus, the hydrogel as a

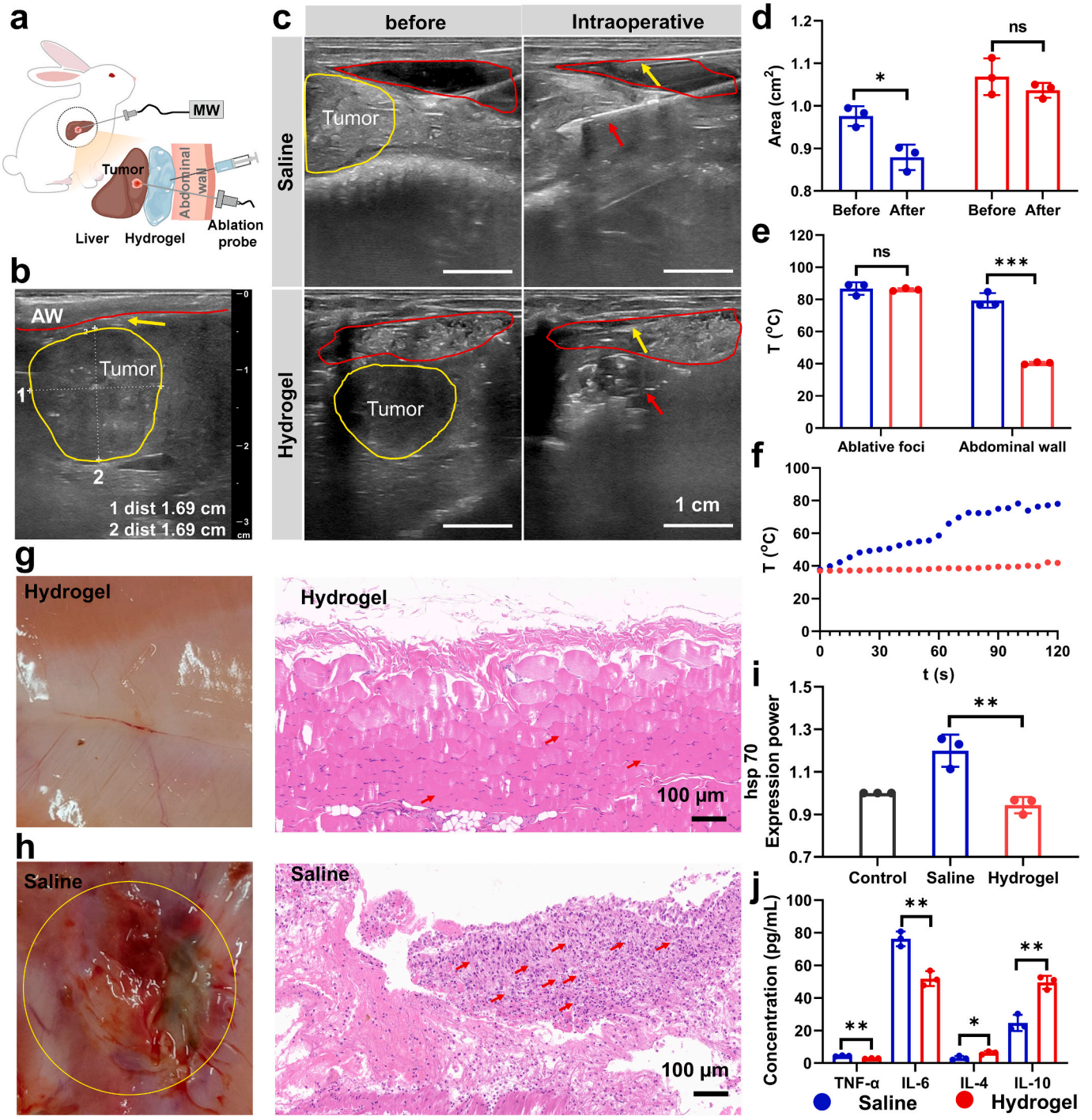


Fig. 2. Thermal protection of the hydrogel in percutaneous ablation of tumors. (a) Graphic illustration of the MWA therapy protocol. (b) Ultrasonic image of transplanted liver VX2 tumor. The tumor is denoted by the yellow circle. The yellow arrow denotes the location of the isolation agent. The red area refers to the abdominal wall. (c) Ultrasonic images of injecting saline and hydrogel respectively between liver and abdominal wall before and during MWA therapy. The tumor is denoted by the yellow circle. The isolation zone is denoted by the red circle. The red arrow represents the ablation antenna. The yellow arrow represents the temperature antenna. Scale bar: 1 cm. (d) Statistics of isolation area for saline and hydrogel before and after MWA therapy. (e) Temperature statistics of the ablation foci and abdominal wall for saline and hydrogel during operation. (f) The process of temperature curve over time of the abdominal wall during surgery. Pictures and H&E staining of rabbit abdominal wall tissue postoperatively in the saline (g) and the hydrogel groups (h). The arrow shows the accumulation of inflammatory cells. Scale bar: 100 μm. (i) HSP70 mRNA expression levels in rabbit abdominal wall tissues after surgery. (j) ELISA analysis of relevant inflammatory factors (TNF-α, IL-6, IL-4, IL-10) in postoperative rabbit abdominal wall tissues. The results are expressed as the mean ± SD in all groups ($n = 3$). ns indicates no difference in data, $^{*}p < 0.05$, $^{**}p < 0.01$, $^{***}p < 0.001$.

physical barrier for percutaneous tumor thermal ablation significantly reduces the prognosis for abdominal wall injury.

After surgery, the experimental rabbits were immediately sacrificed and the abdominal wall tissue surrounding the ablation foci was harvested. No visible changes were observed in the abdominal wall tissue of the hydrogel group (Fig. 2g), whereas significant damage was noted in the saline group (Fig. 2h). Histological results displayed sparse and disorganized cell arrangement in the saline group tissue, with

substantial accumulation of inflammatory cells (denoted by arrows). HSP70 is typically expressed at low levels in cells but its expression increases significantly in response to elevated temperature and various harmful stresses. The expression levels of HSP70 in local tissue were detected by qPCR, revealing significantly higher levels in the saline group than the hydrogel group (Fig. 2i). The H_2S levels of the tissue corroborates this finding, as H_2S is a gaseous inflammatory signaling molecule [43,44]. The H_2S level was increased in the saline group, while there was no significant increment in the hydrogel group (Fig. S9). Following peritoneal damage, pro-inflammatory cytokines (TNF-α, IL-6) are released by injured mesothelial cells and inflammatory cells. The levels of inflammatory factors in the local tissues of the ablation foci were assessed by ELISA (Fig. 2j). The overall levels of pro-inflammatory cytokines TNF-α and IL-6 were significantly higher in the saline group. In comparison, the expression of anti-inflammatory cytokines (IL-4, IL-10) was increased after hydrogel treatment. In other words, the hydrogel effectively mitigates the surgery-induced inflammatory response, which is consistent with the thermal protection effect it plays as described above.

3.3. Heat transfer analysis of the hydrogel

The observed *in vivo* thermal protection efficacy prompted us to systematically investigate the intrinsic thermal conductivity of hydrogel as a potential key determinant of its performance. The heat transfer analysis setup is shown in the Fig. 3a. The hydrogel was filled in a cubic mold surrounded by insulating material on all sides (Fig. 3b), underneath the hydrogel was a heating table (Fig. 3b insert image) with a height of 3 mm (Fig.S10). The distance between monitoring points 1 and 2 was set at 7 mm, between points 2 and 3 was 5 mm, with points 3 and 4 being identical (Fig. 3c). In Fig. 3d, the upper surface of the copper block was heated and maintained at 100 °C, and the hydrogel cube was then placed on it. The temperature increased 14.4 °C at point 2 in 2 min. It did not exceed the limit temperature (42 °C) within 2 min (coinciding with

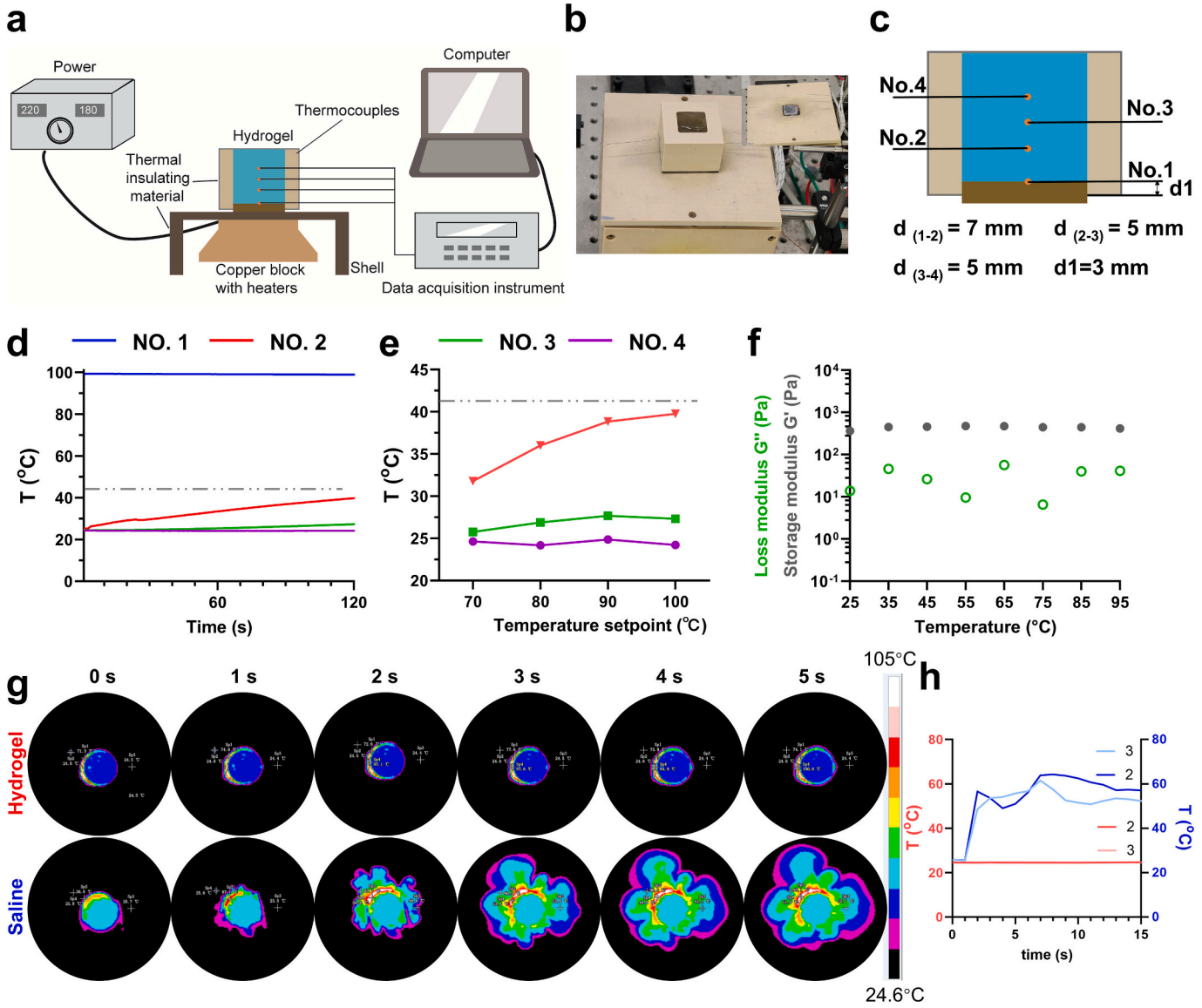


Fig. 3. Thermal analysis of the hydrogel. (a) Experimental schematic diagram of thermal properties of hydrogel. (b) Photographs of the experimental set-up and heating table (insert image). (c) Schematic of the location of the thermocouple line monitoring point inside the hydrogel. (d) Temperature variation at each monitoring points inside the hydrogel when the heater is 100 °C. (e) The steady-state temperatures at each monitoring point at 2 min under set temperatures of 70 °C, 80 °C, 90 °C, and 100 °C. The dashed gray line indicates the threshold of the 42 °C. (f) The average modulus corresponding to the temperature point of small-amplitude temperature sweep results. (g) Dynamic thermographic images of hydrogel/saline and (h) temperature profiles of monitoring points 2 and 3 of the hydrogel/saline group.

the time of the rabbit ablation procedure). The heater was maintained at 90 °C, 80 °C, and 70 °C respectively, and the temperature increases curves at each monitoring point of the hydrogel are shown in Fig. S11. As the externally set temperature decreased, heat conduction within the hydrogel slowed down, and the steady-state temperatures at 2 min of each monitoring point also decreased accordingly (Fig. 3e). In other words, the thermal insulation performance of the hydrogel is temperature dependent. The higher the external temperature, the higher the temperature inside the hydrogel, which likely related to the its high-water content. To investigate whether hydrogels can maintain their viscoelasticity when exposed to high temperatures. The rheological properties of hydrogels at different temperatures were investigated to gain insight into their performance under thermal stress (Fig. S12). Small-amplitude temperature step tests showed that the hydrogel maintained gel properties ($G'>G''$) as the temperature was increased from 25 to 95 °C (Fig. 3f). The entire test lasted 20–30 min, during which time the gel maintained its stability under thermal stress.

Dynamic thermography enables a more intuitive visualization of heat transfer in the hydrogel and saline, as illustrated in Fig. S13a. The two monitoring points were set at a distance of 7 mm from the edge of the iron block (Fig. S13b), which is comparable to the isolation distance created by the *in vivo* injection of the hydrogel. The hydrogel can maintain its morphology after placing a heated iron block (Fig. S13c,d), corroborating its thermal stability (Fig. 3f). In the hydrogel group (Fig. 3g, h; Fig. S13e, f), the images reveal that the hydrogel remains relatively cool: temperatures at No. 2 rose slowly from ~24 °C (0 s) to only ~29 °C (60 s), while No.3 likewise increased modestly to ~27 °C. The temperature curves exhibit a gradual, nearly linear incline over the full 60 s, without any abrupt jumps. By contrast, the saline group demonstrated rapid heat propagation (Fig. 3g, h; Fig. S13g, h). Both No. 2 and No. 3 temperatures surged to 60–70 °C within 5–6 s of heating. The images show a rapidly expanding “hot ring", indicating virtually unimpeded thermal conduction into the surrounding medium. Thus, hydrogel has superior insulating properties compared to saline.

When heated, the transfer of heat in water is mainly by thermal convection. The convective heat transfer coefficient of water is

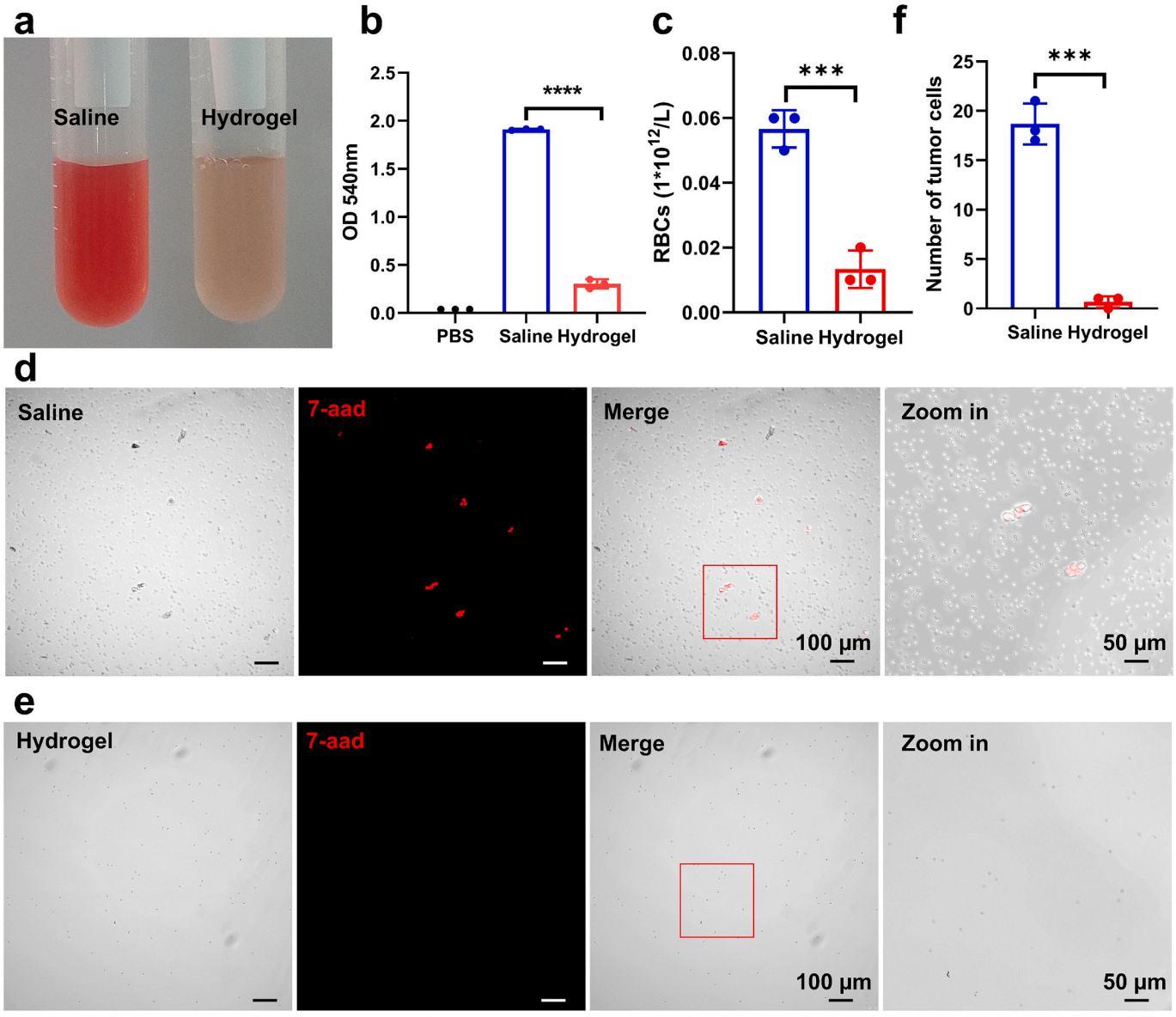


Fig. 4. Evaluation of the hemostatic properties of hydrogel. (a) Optical images of ascites collected postoperatively in the saline and the hydrogel groups. (b) Hemoglobin data of ascites at 540 nm using an enzyme marker. (c) Red blood cell counts in ascites detected by hematology analyzer. Fluorescence confocal images of (d)7-AAD labeled tumor cells and (e) normal red blood cells. (f) Quantitative data of tumor cells. The results are expressed as the mean ± SD in all groups ($n = 3$), where ns indicates no difference in data, $^{*}p < 0.05$, $^{**}p < 0.01$, $^{***}p < 0.001$.

estimated to be 100–1000 W/(m^2·K) for free convection, whereas it can range from 500 to 10,000 W/(m^2·K) for forced convection [45]. According to Fourier's law (1), the coefficient of thermal conductivity of hydrogel is 2.1621 W/(m•K). In fact, the heat transfer within the hydrogel may occur through thermal conduction accompanied with a minor thermal convection when heated. It is attributed to the 97.5 % water content of the hydrogel and the dynamic covalent bonding network. Therefore, the thermal conductivity calculated according to Fourier's formula is termed the "Equivalent Thermal Conductivity", a parameter encompassing both thermal conduction and convection. The thermoprotective properties of the hydrogel can also be explained by that PEG has a relatively high latent heat of fusion. In fact, the heat transfer within the hydrogel ought to be a pretty complicated variation, which might be a topic for in-depth research. In terms of this research, these results strongly support that the hydrogel is an exceptional alternative to saline isolator.

3.4. Evaluation of intraoperative hemostatic properties of the hydrogel

To verify the ability of the hydrogel to prevent leakage of blood cells and tumor cells, saline was injected intraperitoneally post-surgery and then ascites were collected for evaluation. Macroscopically, the saline group had significantly darker colored ascites (Fig. 4a) and a 6.29-fold increase in OD values compared to the hydrogel group (Fig. 4b). Hemoglobin analysis indicated a 4.25-fold higher hematocrit level in the saline group than in the hydrogel group (Fig. 4c). The levels of erythrocytes and tumor cells in the ascites were further assessed by staining. Free tumor cells with nuclei were labeled with 7-AAD, whereas erythrocytes remained unstained. A significantly higher number of erythrocytes and tumor cells in the saline group (Fig. 4d), with few free tumor cells observed in the hydrogel group (Fig. 4e). The count of tumor cells showed an 18.7-fold higher number of free tumor cells in the saline group than in the hydrogel group (Fig. 4f). The liquid saline can carry blood cells and tumor cells to other parts of the abdominal cavity during needle extraction with increased risk of tumor metastasis. Conversely, the hydrogel adheres to the surface of the liver while greatly reducing the leakage of blood cells and tumor cells during the procedure. This resulted in a lowered threat of tumor metastasis and improving substantial prognosis after thermal ablation. Considering the adhesive and self-healing properties of hydrogels, we believe that the function of hemostasis is mainly attributed to the self-healing property of hydrogel. In the process of needle extraction, the hydrogel can self-heal and seal the pinhole caused by the needle, thus physically sealing the bleeding produced during the puncture without assistance of medicines (*e.g.* hemostatic enzymes, *etc.*).

3.5. In vitro sealing test

Building on these findings, the sealing property of the hydrogel which is responsible for their hemostatic performance is evaluated. A

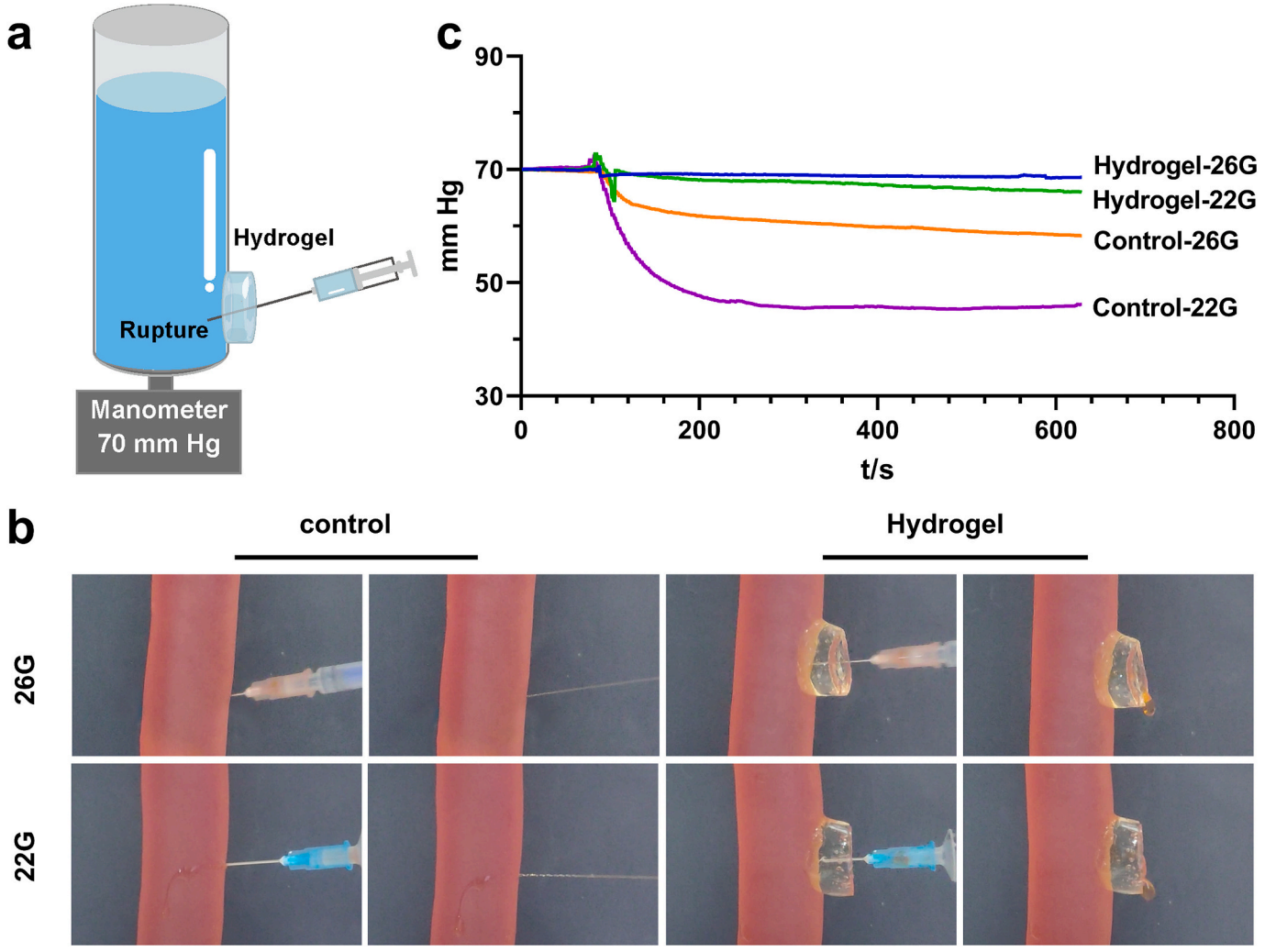


Fig. 5. *In vitro* sealing test. (a) *In vitro* sealing test model. (b) Images of the *in vitro* sealing test with control and hydrogel group, respectively. (c) Quantitative curves of pressure.

device based on a collagen shell was used for performing *in vitro* vascular simulation experiments (Fig. 5a). The collagen enteric coating was filled with PBS stained by acid orange 7 until the pressure reaches 70 mmHg. The shell was then punctured vertically in a downward position using needles of different gauges (Needle 22G and 26G). As shown in Fig. 5b, fluid immediately jetted out upon needle withdrawal in the unprotected group, while fluid leakage slowed significantly when the hydrogel was applied to the puncture site. This finding is corroborated by the manometer results (Fig. 5c) where unprotected collagen tubes exhibited an abrupt initial pressure drop, followed by gradual fluid loss over time. In contrast, hydrogel-protected tubes maintained pressure more effectively, with significantly slower fluid loss. The degree and rate of fluid leakage correlated closely with needle diameter, with the larger 22G needle (outer diameter 0.71 mm) causing faster and more extensive leakage compared to the smaller 26G needle (outer diameter 0.45 mm). Notably, even after puncture with the 22G needle, the hydrogel group only exhibited a minor pressure drop, underscoring the exceptional self-healing capacity of hydrogel. By rapidly sealing the puncture site and protecting the surrounding tissue, the hydrogel effectively reduces fluid loss and demonstrates outstanding protective performance. This sealing ability is particularly valuable in the context of *in vivo* puncture procedures, where it is expected to significantly mitigate the leakage of blood and tumor cells, thereby reducing the risk of abdominal adhesion and tumor metastasis. Moreover, it is worth noting that in clinical tumor puncture thermal ablation, large vessels are typically avoided, and bleeding is primarily caused by injury to the Glisson's capsule or small branches of the portal vein (pressure range: 5–10 mmHg) [46]. Given the relatively low pressures involved, the self-healing capability of hydrogel is sufficient to achieve effective sealing and hemostasis during puncture. This highlights the practical relevance of the hydrogel's sealing performance, reinforcing its potential as an efficient protective barrier during minimally invasive procedures.

3.6. In vivo evaluation of the hydrogel for postoperative anti-tumor metastasis

During the tumor ablation, cells leakage from the needle passage inevitably leads to tumor implantation. Conventional liquid saline is insufficient to prevent the dissemination of tumor cells into surrounding tissues and uncontrollable sites. The experiments on hemostasis have demonstrated that the sealing properties of the hydrogel can effectively mitigate this issue. To further evaluate the protective effect of hydrogel against tumor implantation, ultrasonography and histological evaluation of the postoperative ablation site were performed. Before the ablation procedure *in vivo*, no tumor implantation at the abdominal wall in either the saline or the hydrogel groups (Fig. S14). However, by the 6th postoperative day, an evident abdominal wall metastasis with a diameter of approximately 0.55 cm in the saline group was observed (Fig. 6a), whereas no tumor was detected in the hydrogel group (Fig. 6b). Subsequent dissection of the animal confirmed consistency with the ultrasound results.

Histological assessment, including H&E, Ki67, and MMP2 staining, was conducted on the metastatic tumor and abdominal wall tissue. H&E staining revealed numerous cells organized in nested clusters in the metastatic tumor tissue, displaying heterogeneous nuclei, high nucleoplasm ratios, prominent nucleoli, numerous mitotic figures (yellow arrows), and necrotic foci (red arrows) (Fig. 6c). In contrast, tissues from the hydrogel group displayed normal histological architecture with no evidence of tumor infiltration. High Ki67 expression is typically associated with high proliferative activity of tumor cells and worse prognosis. Thus, positive Ki67 staining indicated a malignant proliferative state and confirmed metastasis in the saline group (Fig. 6d). Additionally, MMP2, a key matrix metalloproteinase involved in extracellular matrix degradation and tumor cell invasion, was diffusely and strongly expressed in the saline group, while no significant expression was observed in the hydrogel group (Fig. S15). These findings collectively highlight the ability of hydrogel to act as an effective physical barrier, significantly reducing tumor cell leakage and subsequent implantation during thermal ablation. By minimizing the risk of postoperative metastasis and preserving tissue integrity, the hydrogel not only enhances the safety of thermal ablation but also contributes to improved long-term prognosis. This demonstrates the considerable potential of hydrogel as a multifunctional protective agent in oncological interventions, combining hemostatic sealing with anti-metastatic benefits.

3.7. In vivo evaluation of the hydrogel for postoperative anti-adhesion

Postoperative tissue adhesions are a common complication following thermal ablation, particularly at surgical contact sites such as the interfaces between the liver and intestine or the liver and peritoneum. Therefore, evaluating the anti-adhesive efficacy of the hydrogel after ablation is essential to assess its potential clinical benefits. On the 6th postoperative day, anatomical examination revealed extensive adhesions in the saline group, with firm connections formed between the abdominal wall and liver, as well as between the liver and intestinal wall (Fig. 7a); whereas no adhesions were observed in the hydrogel group (Fig. 7b). Consistently, the adhesion score in the saline group was significantly higher, reaching a score of 4, while the hydrogel group maintained a score of 0 (Fig. 7c). The major tissues were obtained and analyzed using H&E staining and Masson staining. There are multiple rhabdomyolysis (brown arrows) and massive connective tissue hyperplasia (green arrows) in the muscle layer; accompanied by minor inflammatory cell infiltration dominated by lymphocytes and granulocytes (blue arrows) in the saline group (Fig. 7d). While the hydrogel group displayed well-organized muscle fibers (yellow arrows), predominantly round cells, and an intact peritoneum (red arrows) without any pathological abnormalities. Masson staining can futher clearly show the presence of collagen deposition in the adhesion tissues involving the injured abdominal wall. The saline group had extensive collagen deposition, with significant connective tissue hyperplasia, inflammatory cell infiltration, and a larger fibrotic lesion area (Fig. 7e, f). Moreover, the adhesion band structure was loose, with visible capillaries (Fig. S16), reflecting more severe peritoneal adhesions. No obvious adhesion bands were observed in the hydrogel group, showing a well-preserved mesothelial structure with no evidence of adhesion band formation, indicating effective prevention of postoperative adhesions. Furthermore, abdominal wall injury can activate the NF-κB signaling pathway, leading to higher levels of excessive release of pro-inflammatory cytokines such as TNF-α. qPCR was performed to quantify TNF-α mRNA levels in locally adherent tissues (Fig. 7g). The TNF-α mRNA expression levels were remarkably 8.45-fold higher in the saline group than in the hydrogel group. Accordingly, the hydrogel effectively suppressed the inflammatory response triggered by thermal ablation-induced injury. Taken together, these findings demonstrate that the hydrogel not only serves as a physical barrier to prevent tissue adhesion, but also reduces excessive inflammatory responses at the injury site. This dual protective mechanism highlights the potential of hydrogel as an effective anti-adhesive and anti-inflammatory material, offering significant advantages for improving postoperative outcomes after thermal ablation procedures.

In addition, venous blood samples were collected to assess renal and hepatic function by measuring biomarkers, such as serum alanine aminotransferase (ALT), aspartate aminotransferase (AST), blood urea nitrogen (BUN) and creatinine (CREA). Compared to pre-treatment levels, ALT and AST levels in all groups postoperative were peaked on day 1, decreased on day 4 and decreased to normal levels on day 6 (Fig. 8a, b, Table S1 [47]). The peaks are due to the thermal impact and tumor ablation caused by MWA. The heat generated by MWA inevitably effects liver function while ablating the tumor cells. The slower decrease in ALT levels in the hydrogel group may relate to the metabolism of polymeric materials *in vivo* (Fig. 8a). Comparatively, the absorption of saline is very rapid. ALT levels have decreased to normal on day 6 in the

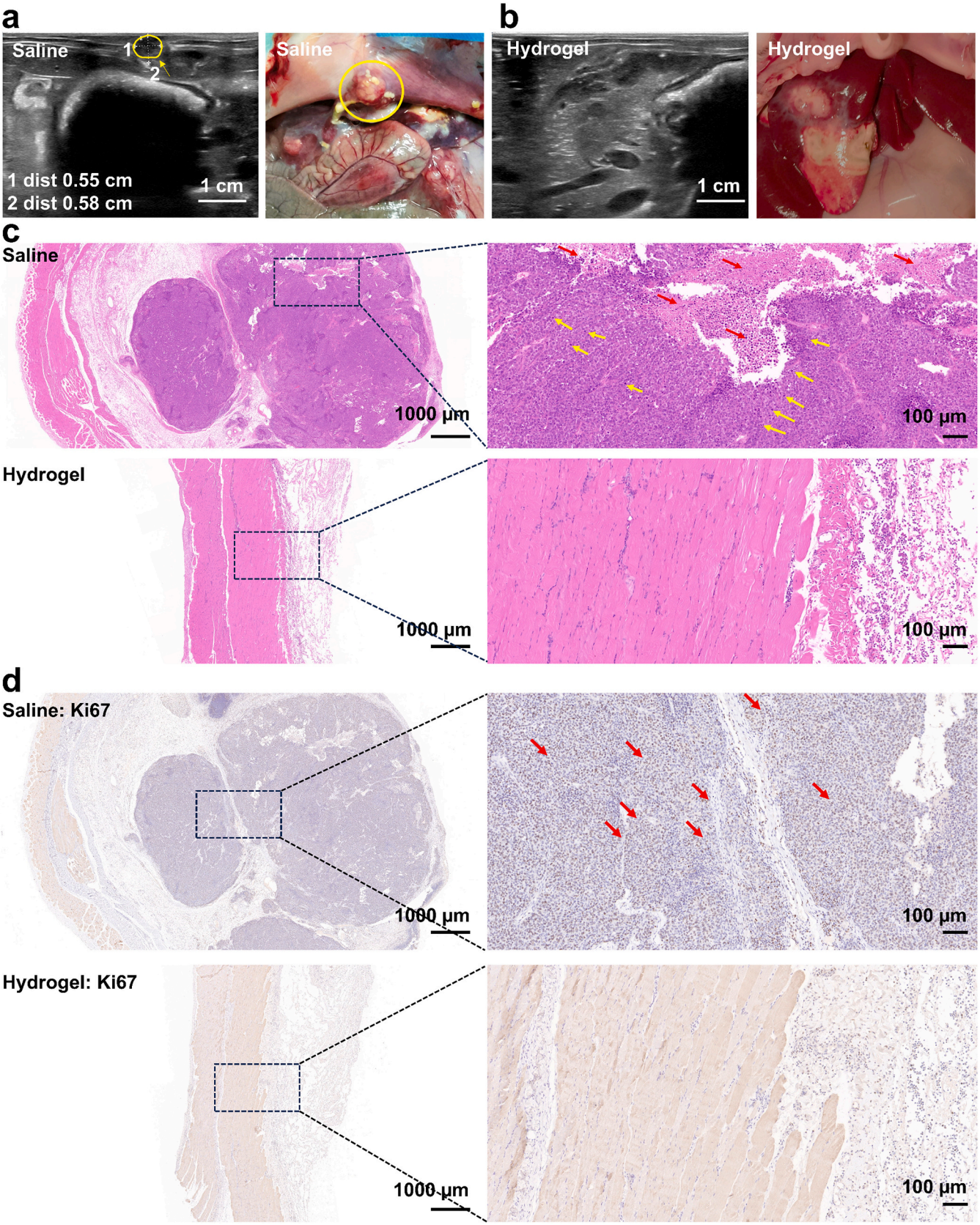


Fig. 6. The hydrogel prevents tumor metastasis in MWA therapy. Ultrasonic and optical images of (a) metastatic tumor on abdominal wall in the saline group, and (b) the normal abdominal wall in the hydrogel group. Scale bar:1 cm. (c) H&E staining of metastatic tumor in the saline group and the normal abdominal wall in the hydrogel group. (d) Ki67 immunostaining of metastatic tumor in the saline group and abdominal wall in the hydrogel group.

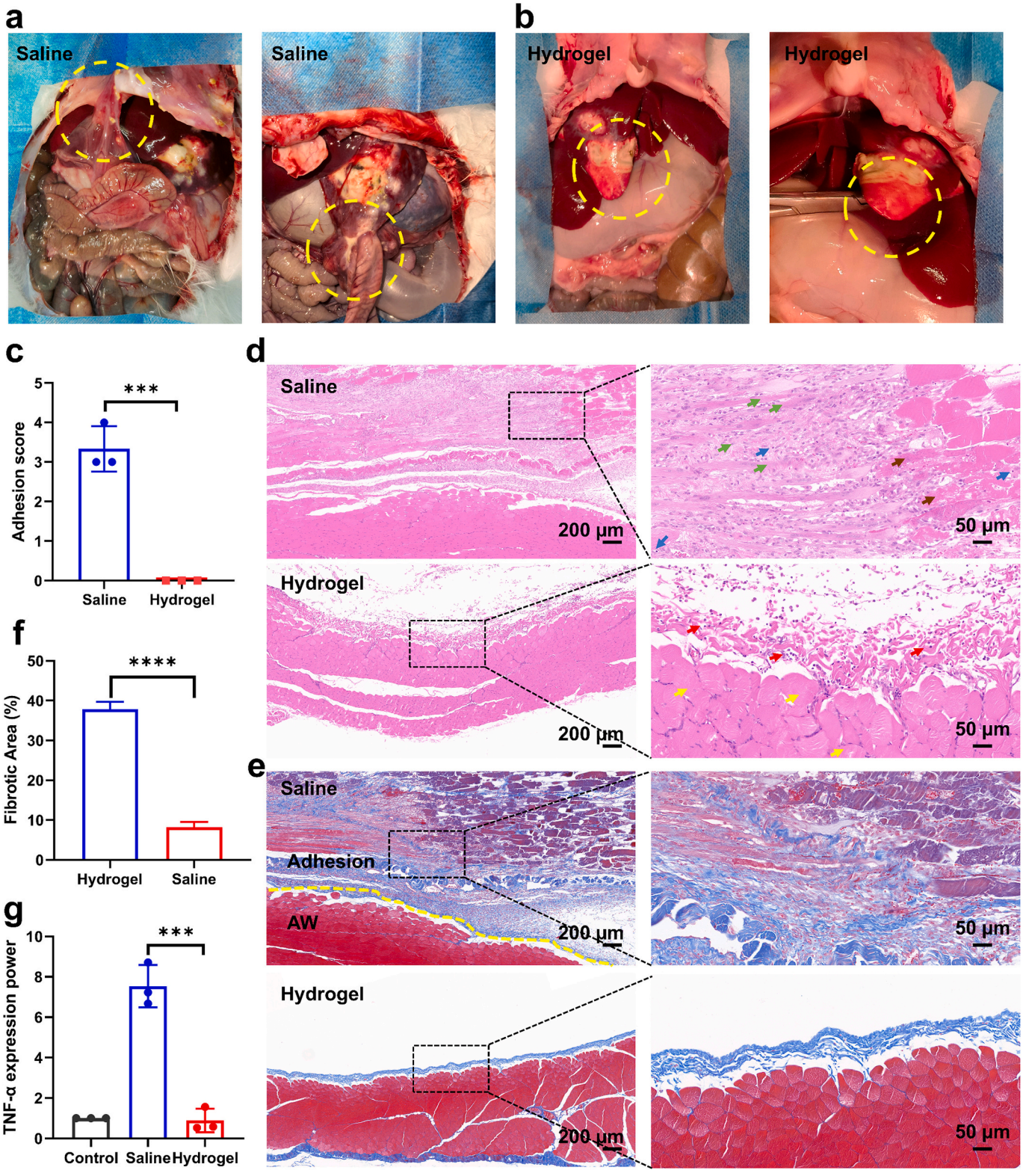


Fig. 7. The hydrogel prevents adhesions after MWA therapy. Optical images of the postoperative abdominal cavity in the saline group (a) and hydrogel group (b). (c) Scoring of the degree of adhesions. The results are expressed as the mean ± SD in all groups ($n = 3$). (d) H&E staining of abdominal wall tissue of saline group and hydrogel group. (e) Masson staining of abdominal wall tissue of saline group and hydrogel group. (f) Quantitative percentage of fibrotic tissue area. The results are expressed as the mean ± SD in all groups (n = 3). (g) The expression level of TNF-α mRNA in abdominal wall tissue. The results are expressed as the mean ± SD in all groups (n = 3). *$p < 0.05$, **$p < 0.01$, ***$p < 0.001$.

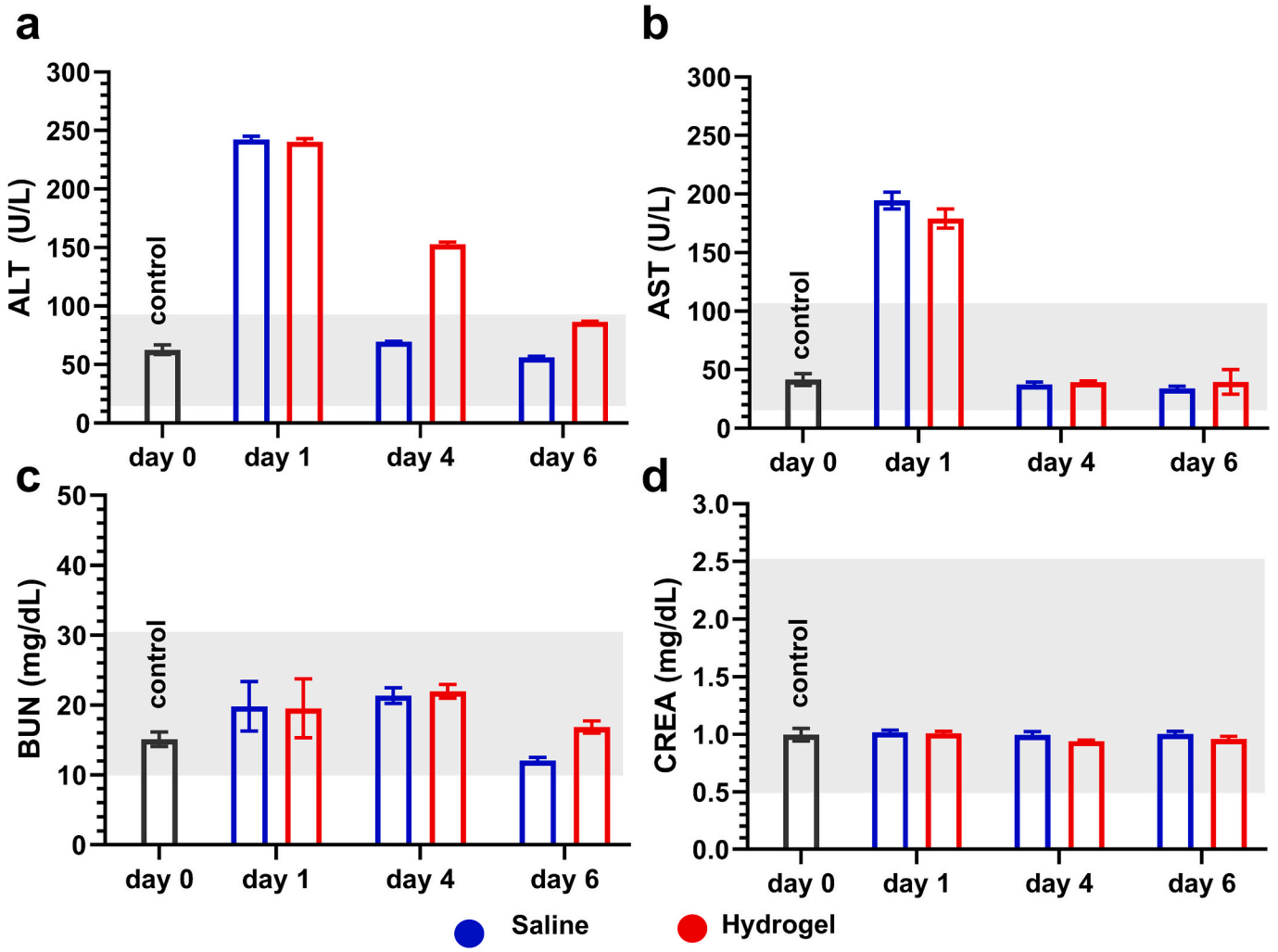


Fig. 8. Blood biochemical analysis of rabbits after MWA treatment. Biomarkers include (a) alanine aminotransferase (ALT), (b) aspartate aminotransferase (AST), (c) urea (BUN) and (d) creatinine (CREA). The gray shading indicates the normal interval of the biochemical values. The results are expressed as the mean ± SD in all groups (Control, $n = 6$, other group, $n = 3$).

hydrogel group. BUN and CREA are often used to evaluate renal function. BUN levels fluctuated in both groups, but remained within normal ranges (Fig. 8c), likely influenced by factors such as circadian rhythms, diet, liver function, hydration and intestinal absorption. CREA had no significantly change in either group (Fig. 8d), suggesting that renal function was not impaired in the treated rabbits. To sum up, these results demonstrate that the hydrogel not only provides effective thermal protection, hemostasis, anti-metastasis, and anti-adhesion benefits during MWA, but also does so without inducing detectable hepatic or renal toxicity. This comprehensive safety profile, combined with its multifunctional therapeutic effects, highlights the significant potential of hydrogel as a superior alternative to saline for improving the safety and efficacy of thermal ablation procedures.

4. Conclusion

We prepared a chitosan-PEG-based self-healing chitosan hydrogel and validated its versatile roles in a thermal ablation model of highly metastatic VX2 tumors, including thermoprotection, hemostasis, anti-tumor metastasis and anti-adhesion, which called “one stone, four birds” strategy. The hydrogel exhibited injectability, good self-healing, shape adaptation, hemocompatibility and cytocompatibility. Especially, the dynamic Schiff base imparts a solid yet dynamic state that is superior to flowing saline. It adhered stably to the surface of the damaged tissue, thus providing superior thermal protection in percutaneous liver tumor ablation of rabbits, and effectively preventing blood and tumor cell leakage. These performances hence reduce abdominal tumor metastasis and potently avoid intraperitoneal adhesions. This hydrogel greatly optimizes clinical treatment strategies for highly metastatic tumors and reduces the rate of local tumor recurrence. Hence, the self-healing chitosan hydrogel is a promising thermal protective agent, which can also play the important roles of postoperative anti-tumor metastasis and anti-tissue adhesion after thermal ablation treatment to improve postoperative prognosis and allow for clinical practice. Future comprehensive large-animal studies and further optimization of the adhesion and sealing of hydrogels are expected to move toward clinical translation. Additionally, it has high potential to further carry anesthetics, painkillers, and anticancer agents in clinical, providing

analgesic and anti-tumor effects postoperatively, thereby contributing to improved postoperative management.

Supplementary data to this article can be found online at https://doi.org/10.1016/j.ijbiomac.2025.144187.

CRediT authorship contribution statement

Lifei Huang: Writing – original draft, Visualization, Methodology, Investigation, Data curation. **Erpeng Qi:** Methodology, Investigation, Data curation. **Zhihan Liu:** Validation, Investigation. **Quanrui Zhang:** Validation, Investigation. **Shuo Wang:** Data curation. **Shaowei Zheng:** Data curation. **Wensheng Xie:** Formal analysis. **Guofeng Li:** Methodology, Formal analysis. **Xue Chen:** Methodology, Formal analysis. **Hui Sun:** Supervision, Resources, Conceptualization. **Fangyi Liu:** Supervision, Resources, Funding acquisition, Conceptualization. **Xing Wang:** Writing – review & editing, Supervision, Funding acquisition, Conceptualization.

Declaration of competing interest

The authors declare that they have no known competing financial interests or personal relationships that could have appeared to influence the work reported in this paper.

Acknowledgments

This work was supported by Key Program of Beijing Natural Science Foundation (grant number Z200025), National Natural Science Foundation of China (grant number 52273118, grant number 22275013, grant number 82171940), and Fundamental Research Funds for the Central Universities (grant number QNTD2023-01).

Data availability

Data will be made available on request.

References

[1] M. Ahmed, C.L. Brace, F.T. Lee, et al., Principles of and advances in percutaneous ablation[J], Radiology 258 (2) (2011) 351–369.
[2] F. Zhu, H. Rhim, Thermal ablation for hepatocellular carcinoma: what's new in 2019: 6[J], Chin. Clin. Oncol. 8 (6) (2019) 58.
[3] L. Crocetti, T. De Baére, P.L. Pereira, et al., CIRSE standards of practice on thermal ablation of liver tumours[J], Cardiovasc. Intervent. Radiol. 43 (7) (2020) 951–962.
[4] H. Takahashi, E. Berber, Role of thermal ablation in the management of colorectal liver metastasis[J], Hepatobiliary Surg. Nutr. 9 (1) (2020) 49–58.
[5] Y. Choi, S.-L. Jung, Efficacy and safety of thermal ablation techniques for the treatment of primary papillary thyroid microcarcinoma: a systematic review and meta-analysis[J], Thyroid® 30 (5) (2020) 720–731.
[6] F. Izzo, V. Granata, R. Grassi, et al., Radiofrequency ablation and microwave ablation in liver tumors: an update[J], Oncologist 24 (10) (2019) e990–e1005.
[7] S. Shiina, K. Sato, R. Tateishi, et al., Percutaneous ablation for hepatocellular carcinoma: comparison of various ablation techniques and surgery[J], Can. J. Gastroenterol. Hepatol. 1 (2018) 4756147.
[8] N.V. Violi, R. Duran, B. Guiu, et al., Efficacy of microwave ablation versus radiofrequency ablation for the treatment of hepatocellular carcinoma in patients with chronic liver disease: a randomised controlled phase 2 trial[J], Lancet Gastroenterol. Hepatol. 3 (5) (2018) 317–325.
[9] Y. Zhou, Y. Yang, B. Zhou, et al., Challenges facing percutaneous ablation in the treatment of hepatocellular carcinoma: extension of ablation criteria[J], J. Hepatocell. Carcinoma 8 (2021) 625–644.
[10] Y. Min, X. Wang, H. Chen, et al., Thermal ablation for papillary thyroid microcarcinoma: how far we have come?[J], Cancer Manag. Res. 12 (2020) 13369–13379.
[11] K. Leuchte, E. Staib, M. Thelen, et al., Microwave ablation enhances tumor-specific immune response in patients with hepatocellular carcinoma[J], Cancer Immunol. Immunother. 70 (4) (2021) 893–907.
[12] B. Radjenović, M. Sabo, L. Šoltes, et al., On efficacy of microwave ablation in the thermal treatment of an early-stage hepatocellular carcinoma: 22[J], Cancers 13 (22) (2021) 5784.
[13] S. Nieuwenhuizen, M. Dijkstra, R.S. Puijk, et al., Microwave ablation, radiofrequency ablation, irreversible electroporation, and stereotactic ablative body radiotherapy for intermediate size (3–5 cm) unresectable colorectal liver metastases: a systematic review and meta-analysis[J], Curr. Oncol. Rep. 24 (6) (2022) 793–808.
[14] J. Zhao, Q. Li, M. Muktiali, et al., Effect of microwave ablation treatment of hepatic malignancies on serum cytokine levels[J], BMC Cancer 20 (1) (2020) 812.
[15] N.H. Shaheen, A.D. Hardie, Approach to hepatic tumor ablation: choosing the right tool for the job[J], Acad. Radiol. 31 (4) (2024) 1302–1303.
[16] K.B. Gala, N.S. Shetty, P. Patel, et al., Microwave ablation: how we do it?[J], Indian J. Radiol. Imaging 30 (2) (2020) 206–213.
[17] T.J. Vogl, N.-E.A. Nour-Eldin, R.M. Hammerstingl, et al., Microwave ablation (MWA): basics, technique and results in primary and metastatic liver neoplasms–review article[J], RöFo-Fortschritte auf dem Gebiet der Röntgenstrahlen und der bildgebenden Verfahren 189 (11) (2017) 1055–1066.
[18] P. Liang, Y. Wang, X. Yu, et al., Malignant liver tumors: treatment with percutaneous microwave ablation—complications among cohort of 1136 patients [J], Radiology 251 (3) (2009) 933–940.
[19] R.Z. Swan, D. Sindram, J.B. Martinie, et al., Operative microwave ablation for hepatocellular carcinoma: complications, recurrence, and long-term outcomes[J], J. Gastrointest. Surg. 17 (4) (2013) 719–729.
[20] C. Fang, K. Cortis, G.T. Yusuf, et al., Complications from percutaneous microwave ablation of liver tumours: a pictorial review[J], Br. J. Radiol. 92 (1099) (2019) 20180864.
[21] W. Tan, Q. Deng, S. Lin, et al., Comparison of microwave ablation and radiofrequency ablation for hepatocellular carcinoma: a systematic review and meta-analysis[J], Int. J. Hyperth. 36 (1) (2019) 263–271.
[22] S. Zensen, A. Bücker, M. Meetschen, et al., Current use of percutaneous image-guided tumor ablation for the therapy of liver tumors: lessons learned from the registry of the German Society for Interventional Radiology and Minimally Invasive Therapy (DeGIR) 2018–2022[J], Eur. Radiol. 34 (5) (2024) 3322–3330.
[23] Z. Yanna, Jun Liu, H. Li, et al., Safety of normal saline isolation zone: an experimental study on laser, radiofrequency and microwave thyroid thermal ablation[J], J. Surg. Concept Pract. 25 (05) (2020) 432.
[24] J. Wu, Z.-L. Zhao, X.-J. Cao, et al., A feasibility study of microwave ablation for papillary thyroid cancer close to the thyroid capsule[J], Int. J. Hyperth. 38 (1) (2021) 1217–1224.
[25] A. Pfannenstiel, J. Sebek, H. Fallahi, et al., Directional microwave ablation: experimental evaluation of a 2.45-ghz applicator in ex vivo and in vivo liver[J], J. Vasc. Interv. Radiol. 31 (7) (2020), 1170–1177.e2.
[26] M. Ozen, D. Raissi, Current perspectives on microwave ablation of liver lesions in difficult locations[J], J. Clin. Imaging Sci. 12 (2022) 61.
[27] J. Garnon, R.L. Cazzato, J. Caudrelier, et al., Adjunctive thermoprotection during percutaneous thermal ablation procedures: review of current techniques[J], Cardiovasc. Intervent. Radiol. 42 (3) (2019) 344–357.
[28] G. Tsoumakidou, X. Buy, J. Garnon, et al., Percutaneous thermal ablation: how to protect the surrounding organs[J], Tech. Vasc. Interv. Radiol. 14 (3) (2011) 170–176.
[29] A. Radosevic, R. Quesada, C. Serlavos, et al., Microwave versus radiofrequency ablation for the treatment of liver malignancies: a randomized controlled phase 2 trial[J], Sci. Rep. 12 (1) (2022) 316.
[30] L. Feng, Y. Wang, L.J. Niu, Ultrasound-guided percutaneous thermal ablation assisted by artificial ascites and soft tissue edema in the treatment of special-region hepatic tumors[J], Zhonghua Zhong liu za zhi [Chinese Journal of Oncology] 46 (2) (2024) 155–160.
[31] P. Namakshenas, A. Mojra, Optimization of polyethylene glycol-based hydrogel rectal spacer for focal laser ablation of prostate peripheral zone tumor[J], Physica Medica 89 (2021) 104–113.
[32] K. Liu, M. Russo, J.S. Ellis, et al., Transient, image-guided gel-dissection for percutaneous thermal ablation[J], Adv. Healthc. Mater. (2024) 2400272.
[33] L. Huang, S. Yang, M. Bai, et al., Thermal shielding performance of self-healing hydrogel in tumor thermal ablation[J], Colloids Surf. B: Biointerfaces 213 (2022) 112382.
[34] T. Narukawa, A. Fujihara, A. Ochiai, et al., Role of hydrogel spacer to protect the rectum from thermal injury in focal therapy of prostate cancer: preclinical study in cadaver model[J], Int. J. Urol. 30 (1) (2023).
[35] L.-L. Zhang, G.-M. Xia, Y.-J. Liu, et al., Effect of a poloxamer 407-based thermosensitive gel on minimization of thermal injury to diaphragm during microwave ablation of the liver[J], World J. Gastroenterol. 23 (12) (2017) 2141–2148.
[36] Y. Cao, Y. Zhou, J. Pan, et al., A general strategy towards an injectable microwave-sensitive immune hydrogel for combined percutaneous microwave ablation and immunotherapy[J], Chem. Eng. J. 422 (2021) 130111.
[37] B. Zheng, P. Zhang, Q. Lv, et al., Development and preclinical evaluation of multifunctional hydrogel for precise thermal protection during thermal ablation [J], Bioact. Mater. (31) (2024) 119–135.
[38] Y. Fu, Y. Li, B. Deng, et al., Spatiotemporally dynamic therapy with shape-adaptive drug-gel for the improvement of tissue regeneration with ordered structure[J], Bioact. Mater. (8) (2022) 165–176.
[39] S.H. Kim, K. Kim, B.S. Kim, et al., Fabrication of polyphenol-incorporated anti-inflammatory hydrogel via high-affinity enzymatic crosslinking for wet tissue adhesion[J], Biomaterials 242 (2020) 119905.
[40] F. Pascale, J.P. Pelage, M. Wassef, et al., Rabbit VX2 liver tumor model: a review of clinical, biology, histology, and tumor microenvironment characteristics[J], Front. Oncol. 12 (2022) 871829.
[41] X. Duan, G. Zhou, C. Zheng, et al., Heat shock protein 70 expression and effect of combined transcatheter arterial embolization and radiofrequency ablation in the rabbit vx2 liver tumour model[J], Clin. Radiol. 69 (2) (2014) 186–193.

[42] H. Li, P. Chen, M. Wang, et al., Liposome quercetin enhances the ablation effects of microwave ablation in treating the rabbit vx2 liver tumor model[J], Int. J. Hyperth. 39 (1) (2022) 162–172.
[43] H. Kimura, N. Shibuya, Y. Kimura, Hydrogen sulfide is a signaling molecule and a cytoprotectant[J], Antioxid. Redox Signal. 17 (1) (2012) 45–57.
[44] H. Kimura, Signaling molecules: hydrogen sulfide and polysulfide[J], Antioxid. Redox Signal. 22 (5) (2015) 362–376.
[45] P.K. Jain, Taking the heat off of plasmonic chemistry[J], J. Phys. Chem. C 123 (40) (2019) 24347–24351.
[46] A.L. Baert, Portal Hypertension: Diagnostic Imaging and Imaging-Guided Therapy, Springer Science & Business Media, 2012.
[47] M. Washington I, G. Van Hoosier, Clinical biochemistry and hematology[M]//The laboratory rabbit, guinea pig, hamster, and other rodents, Academic Press (2012) 57–116.

Published on 03 November 2022. Downloaded by Beijing University of Chemical Technology on 9/1/2025 2:07:42 PM.

Journal of Materials Chemistry B

ROYAL SOCIETY OF CHEMISTRY

REVIEW

View Article Online
View Journal | View Issue

Check for updates

Cite this: *J. Mater. Chem. B*, 2022, **10**, 9735

Multicomponent carrier-free nanodrugs for cancer treatment

Lifei Huang, Shuyang Hu, Ya-nan Fu, Yan Wan, Guofeng Li* and Xing Wang *

Received 23rd September 2022,
Accepted 27th October 2022

DOI: 10.1039/d2tb02025d

rsc.li/materials-b

Nanocarriers can be used to deliver insoluble anticancer drugs to optimize therapeutic efficacy. However, the potential toxicity of nanocarriers cannot be ignored. Carrier-free nanodrugs are emerging safe drug delivery systems, which are composed of multiple components, such as drugs, bioactive molecules and functional ingredients, avoiding the usage of inert carrier materials and offering advantages that include high drug loading, low toxicity, synergistic therapy, versatile design, and easy surface functionalization. Therefore, how to design multicomponent carrier-free nanodrugs is becoming a priority. In this review, the common strategies for rapid construction of multicomponent carrier-free nanodrugs are briefly explored from the perspective of methodology. The properties of organic–organic, organic–inorganic and inorganic–inorganic multiple carrier-free nanosystems are analyzed according to wettability and in-depth understanding is provided. Further advances in the applications of multiple carrier-free nanodrugs are outlined in anticipation of grasping the intrinsic nature for the design and development of carrier-free nanodrugs.

1. Introduction

The mortality and monetary burden caused by cancer is enormous.[1] Clinically, the main therapy for most cancers involves surgery,[2,3] chemotherapy[4,5] and radiotherapy.[6] However, most anticancer drugs exhibit limitations such as poor water solubility, low bioavailability, high toxicity, limited stability, and rapid blood clearance, thus causing serious obstacles to cancer treatment.[7] As nanotechnology develops in leaps and bounds, nanodrug systems have been applied to cancer diagnosis and treatment due to their versatility, targeting, enhanced permeability and accumulation in tumors. Nanoparticles (NPs) are usually generated by loading drugs within nanocarrier materials or stabilizing with nonpharmaceutical excipients.[8–10] However, the potential side effects and biodegradation problems of carriers will impose a potential burden on patients.[11,12]

Carrier-free nanodrugs emerge as nanodrug delivery platforms without additional carrier materials during the assembly process. Commonly, carrier-free nanodrugs are mainly pure drug nanocrystals or multicomponent carrier-free nanodrugs. Although pure drug nanocrystals without matrix materials can be simply prepared by nanotechnology,[13–15] they suffer from limitations such as a lack of versatility, and unstable crystal quality and stability. Multicomponent carrier-free nanodrugs refer to those nanodrugs with a certain assembled shape composed of drugs (such as the usual molecular drugs and homo dimer or hetero dimer drugs), bioactive molecules (such as carbohydrates and peptides), and functional ingredients (such as targeting agents, photosensitizers, photothermal agents, and imaging agents), without adding inert substances and stabilizers. This endows them with some desirable advantages over drug-carrier systems. First, the assembly process is simple and green, exhibiting brilliant performance in tumor synergistic treatment.[16–18] Second, each component of carrier-free nanodrugs can act as both the therapeutic agent and "carrier", leading to high drug-loading efficiency, synergistic therapy and avoiding the toxicity caused potentially by carrier materials. Third, in contrast to pure drug nanocrystals, multicomponent carrier-free nanodrugs are easily designed as drug self-delivery systems with targeting, controllability and sensitivity. Therefore, multicomponent carrier-free nanodrugs are considered to be a promising strategy for cancer diagnosis and treatment.

To date, the definitions of carrier-free nanodrugs are ambiguous. Herein, carrier-free nanodrugs are defined in general and special meanings, thus delimiting the boundary and avoiding any misunderstanding. Carrier-free nanodrugs have both general and special meanings. Carrier-free nanodrugs in the general meaning contain both drugs and non-pharmaceutical ingredients that enable targeted delivery, an extended long circulation time and reinforced therapeutic efficacy. They are versatile combinations that exert a synergistic therapeutic effect. Nowadays, many reported carrier-free nanodrugs are obtained by assembling drugs and small molecules or active ingredients. Whereas, the incorporation of bioactive molecules

State Key Laboratory of Organic–Inorganic Composites, Beijing Laboratory of Biomedical Materials, Beijing University of Chemical Technology, Beijing 100029, China. E-mail: ligf@mail.buct.edu.cn, wangxing@mail.buct.edu.cn

Published on 03 November 2022. Downloaded by Beijing University of Chemical Technology on 9/1/2025 2:07:42 PM.

and functional ingredients tends to confer carrier-free nanodrugs with diverse therapy, such as targeted therapy, photodynamic therapy, photothermal therapy and synergistic chemotherapy, and it is also defined as a carrier-free nanodrug. This should be categorized as the general meaning of carrier-free nanodrugs due to the composition of non-drug components. Correspondingly, the special meaning of carrier-free nanodrugs is based on subtle design of multiple combinations of pure drugs or homo dimer drugs. It is in favor of changing the drug delivery pathway, enabling multidrug synergy and meeting clinical needs. In this paper, we review the above all carrier-free nanodrugs, with focus on providing an overview of the most researched general meaning of carrier-free nanodrugs. Recently, some teams have reviewed the preparation and application of carrier-free nanodrugs.[19–25] Most classifications are based on assembled modules, emphasizing the significant anti-tumour effects generated by carrier-free nanodrugs assembled from different therapeutic agents, while the basic properties of their constituent substances are less discussed. Hence exploring the construction of a system from the basic properties is a novel perspective for comprehending carrier-free nanodrugs.

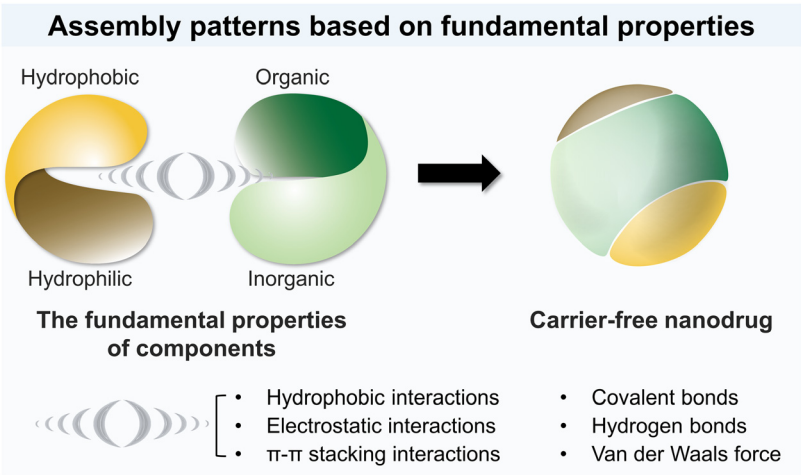
The components of various carrier-free nanodrugs have certain basic properties, including organic or inorganic, and hydrophilic or hydrophobic. Based on these properties, different components are assembled into a nanodrug through several interactions and bonds. In other words, multi-forces drive the assembly of multicomponents with different properties into carrier-free nanodrugs (Scheme 1). According to the components of organic/inorganic, carrier-free nanodrugs can be divided into "organic–organic", "organic–inorganic", and "inorganic–inorganic" nanodrugs. Each classification can be further discussed in terms of "hydrophobic–hydrophobic" and "hydrophilic–hydrophobic" based on the wettability of components. There are no "hydrophilic–hydrophilic" assembled drugs due to their good solubility and few assembled structures.

In this review, the constructed methods based on the fundamental properties of multicomponent carrier-free nanodrugs are systematically summarized. Further study of the properties and functions of the assembled modules may be instructive to the development of novel, multifunctional, safe, and efficient nanodrugs. Then, the challenges faced by carrier-free nanodrugs are discussed and future prospects for their application are envisaged. Collectively, we hope that this review will help to better dissect multicomponent carrier-free nanodrugs based on the fundamental properties of their constituent substances and provide a novel construction strategy toward achieving rational design, multifunctional synergy and optimal therapeutics of carrier-free nanodrugs.

2. Multicomponent carrier-free nanodrugs

2.1 "Organic–organic" components

2.1.1 "Hydrophobic–hydrophobic" assemblies. Most organic anticancer drugs are hydrophobic compounds. In general, "hydrophobic–hydrophobic" assemblies have two co-assembly patterns: (i) the hydrophobic drugs and therapeutic agents are directly aggregated together through hydrophobic interactions, π–π stacking interactions, and electrostatic interactions; (ii) the hydrophobic drugs are first combined into interconnected dual (homo or hetero dimer) or multicomponent small molecules, and then assembled into nano-assemblies. The assembled forces include covalent bonds, hydrogen bonds, hydrophobic interactions, π–π stacking interactions, and electrostatic interactions.[26,27] The difference between the two modes is that the assembly force of the latter involves intermolecular bonds. Intermolecular bonds are often designed to stimulate a response and release the drug components in carrier-free nanodrugs on demand.



Scheme 1 Overview of the composition of multicomponent carrier-free nanodrugs based on the fundamental properties of their constituent substances.

 This journal is © The Royal Society of Chemistry 2022

Published on 03 November 2022. Downloaded by Beijing University of Chemical Technology on 9/1/2025 2:07:42 PM.

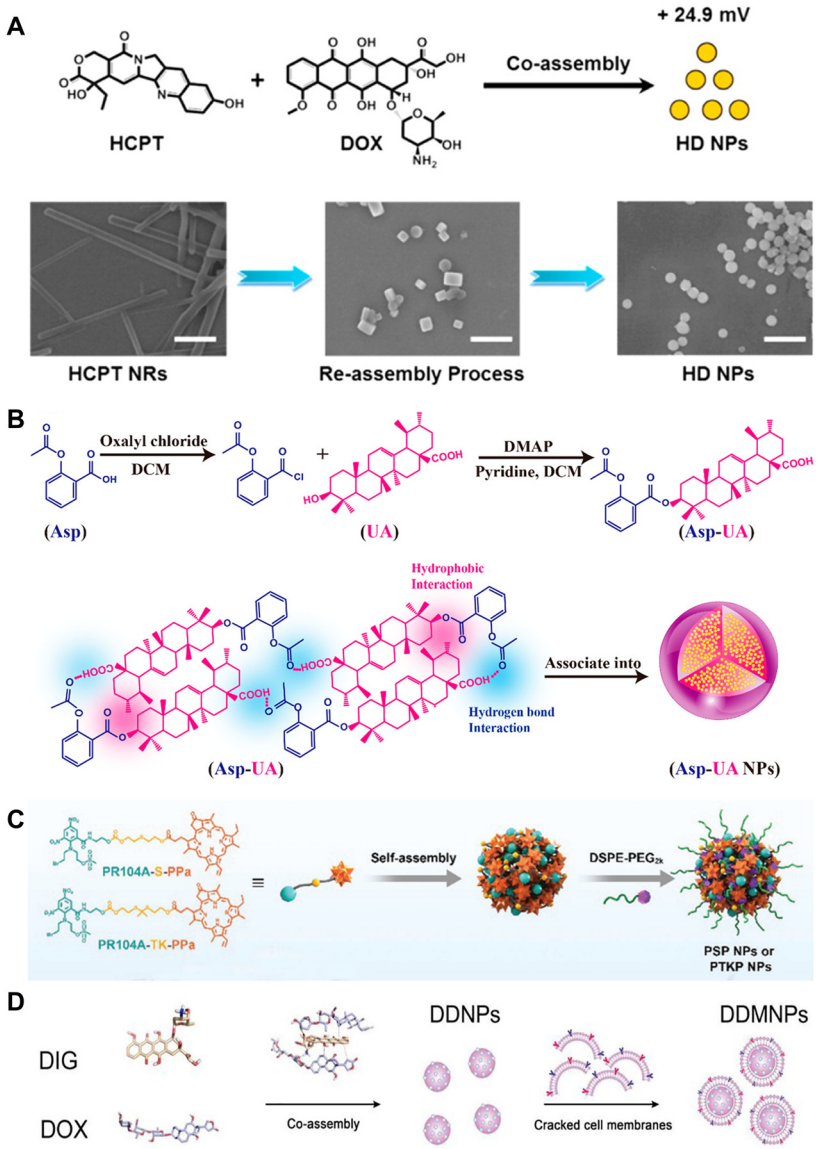


Fig. 1 (A) Schematic illustration of the preparation of HD (HCPT/DOX) NPs. Reproduced with permission from ref. 30. Copyright 2015, American Chemical Society. (B) Co-assembly of Asp-UA NPs associated with the hydrogen bond and hydrophobic interactions. Reproduced with permission from ref. 34. Copyright 2018, American Chemical Society. (C) Self-assembly of heterodimer prodrugs-NPs. Reproduced with permission from ref. 46. Copyright 2020, The Royal Society of Chemistry. (D) Preparation of cracked cancer cell membranes camouflaged DIG (digoxin)/DOX carrier-free NPs. Reproduced with permission from ref. 47. Copyright 2021, Elsevier.

Hydrophobic drug molecules can be transformed into NPs with smaller dimensions by reprecipitation. Previously, reprecipitation was used for the simple preparation of carrier-free pure drug nanocrystals.[28,29] Subsequently, this method has been used for the preparation of multi-component carrier-free nanosystems.[30,31] For instance, hydroxycamptothecin (HCPT) and doxorubicin (DOX) were assembled into a carrier-free dual drug delivery system by reprecipitation through hydrophobic interactions (Fig. 1A).[30] Compared with the physical mixing of HCPT and DOX at high concentrations, the NPs showed excellent synergistic chemotherapy and inhibited tumor resistance due to its stable assembly structure. The NPs were assembled through the high hydrophobic properties between different components, rather than connected by chemical bonds.[32,33] Meanwhile, aspirin (Asp) and ursolic acid (UA) NPs were prepared based on an ester bond and hydrophobic interaction (Fig. 1B).[34] The sensitive chemical bonds endowed the NPs with pH sensitivity, thus they had an effective anti-tumor metastasis effect when internalized by tumor cells.

"Hydrophobic–hydrophobic" assemblies can be utilized as carriers for other drugs in the assemblies. For example, an indomethacin dimer (IND-OE) based on an orthoester bond was prepared.[35] Subsequently, the dimer was successfully loaded with DOX and assembled into carrier-free composite NPs (IND-OE/DOX). The orthoester bond in the assembly could respond to the weakly acidic environment of tumors to release drugs. Then, the IND mediated the P-gp downregulation to reduce the DOX efflux, resulting in the effective intracellular

Published on 03 November 2022. Downloaded by Beijing University of Chemical Technology on 9/1/2025 2:07:42 PM.

accumulation of DOX. Thus, a carrier-free nanodrug as ''carriers'' for hydrophobic drugs can be a very promising way to improve the hydrophobicity of drugs.

In addition to the assembly of pure drugs, the incorporation of functional ingredients such as photosensitizers and photothermal agents confers the assemblies with more therapeutic effects.[33,36–42] Most organic photosensitizers and photothermal agents are hydrophobic. For example, chlorin e6 (Ce6) is a hydrophobic photosensitizer with high efficiency in generating singlet oxygen, but tends to aggregate in solution. Ce6 and 7-ethyl-10-hydroxycamptothecin (SN38) were assembled into carrier-free NPs (SN38/Ce6 NPs) under hydrogen bonds and hydrophobic interactions,[37] enabling the combination of chemotherapy and photodynamic therapy (PDT). It follows that photosensitizers endow assemblies with PDT and photothermal therapy (PTT), which greatly enhance the anti-tumor effect. Another novel design is that Yang *et al.* co-assembled bortezomib (BTZ, a proteasome inhibitor) and pyropheophorbide a (PPa) into a precisely engineered nanoassembly (BTZ@PPa) for proteasome inhibition-mediated PDT sensitization.[42] BTZ inhibited the ubiquitin-proteasome pathway (UPP) and synergized with PPa to significantly enrich ROS-damaged proteins in tumor cells. Clearly, the diverse drug mechanisms allow for a versatile design of the drug-photosensitizer assembly.

Nano-prodrug, as a special self-delivery nanosystem, was generally synthesized by coupling an active drug to other drugs or active ingredients through cleavable bonds, resulting in an inactive conjugate. Currently, it has received increasing attention due to their high selectivity, low toxicity and strong permeability, which can evade the aggregation-caused quenching (ACQ) effect of photosensitizers and greatly improve the photodynamic efficiency.[43–46] For instance, Zhao and coworkers designed new heterodimeric prodrugs (PR104A-S-PPa and PR104A-TK-PPa) by conjugating PPa to hypoxia-activated prodrugs PR104A *via* thioketal bonds (Fig. 1C).[46] The formation of alkyl cations and sulfur radicals by C–S cleavage is one of the most studied sulfur radical cation decomposition pathways that can be used to initiate drug release. C–S cleavage under light to form alkyl cations and sulfur-free radicals, with the excited PPa preferentially reacting directly with adjacent S-containing bonds. PR104A was released by photoinduced electron transfer. PPa gradually escaped the trap of the ACQ effect and produced singlet oxygen, which further promoted the sensitive release of reactive oxygen species (ROS). Simultaneously, PDT consumed oxygen and produced severe hypoxia, which promoted the activation of PR104A. This unique prodrug aims to overcome a series of obstacles in the combination of PDT and hypoxia activation therapy, providing insights into the development of a multi-response carrier-free nanodrug platform.

To evade the recognition of biological defense systems, the concept of ''bionics'' was thus derived for the design of carrier-free nanodrugs. Cell membranes are used to modify the surface of NPs to improve the rapid elimination of NPs *in vivo*.[47,48] The selection of natural cell membranes includes erythrocyte membranes, cancer cell membranes, and macrophage membranes. Surface modifications of natural cell membranes confer immune escape and long-term circulation of NPs in the body. For example, Zhang and coworkers combined DNA damage repair inhibitor digoxin (DIG) and DNA damage agent DOX to prepare carrier-free NPs (DDNP), and then further embedded them into the membrane framework of the NSCLC cell line A549 (DDMNP) (Fig. 1D).[47] The DDMNPs were specifically internalized into A549 cells rather than prostate cancer DU145 and macrophage RAW264.7 cells. Compared to free drugs, the bionic DDMNP system could cause cell apoptosis, enhance DNA damage, exhibit a more effective anti-tumor effect *in vivo*, and improve safety. In a similar manner, Zhang *et al.* used erythrocyte membranes to disguise NPs assembled with dual-mode photosensitizers including 1,1′-dioctadecyl-3,3,3′,3′-tetramethylindotricarbocyanine iodide (DiR) and Ce6.[48] After being camouflaged by the erythrocyte membrane, the circulation time in the blood was prolonged, the accumulation in tumors was increased, and the penetration in tumors was deepened. In this system, Ce6 as the Förster Resonance Energy Transfer (FRET) donor, and DiR as the FRET acceptor, both form a FRET pair. Under the cascade local laser irradiation, Ce6 was quenched by DiR, and the photosensitivity of Ce6 was ''turned off''. Thus, the phototoxicity of Ce6 induced by ROS was effectively reduced. Ce6 could be unlocked by PDT only when DiR was bleached with an 808 nm laser. The results showed that the phototoxicity caused by Ce6 could be well controlled, and the biomimetic nano-assembly demonstrated synergistic PTT/PDT. Therefore, disguising cell membranes on NPs to achieve ''bionics'' is an effective strategy to reduce undesirable non-specific interactions while increasing target-specific interactions. The ''bionic'' drug delivery systems are well targeted and have low immunogenicity. Presently, the combination of ''bionic'' and carrier-free nanodrugs has become the spotlight with great prospects for development and application.

2.1.2 ''Hydrophilic–hydrophobic'' assemblies. Improving the hydrophilicity of nanodrugs can enhance their bioavailability. Attention has gradually shifted to hydrophilic components. Combining hydrophilic and hydrophobic components can form excellent assemblies and easily maintain stability. Thus, the ''hydrophilic–hydrophobic'' assemblies are in general adopted due to their excellent amphiphilicity. For ''hydrophilic–hydrophobic'' assemblies, two co-assembly patterns were included: (i) the hydrophilic drugs and hydrophobic drugs are simply aggregated together, (ii) the hydrophilic drugs and hydrophobic drugs are first formed as amphiphilic conjugates and then self-assembled into carrier-free nanodrugs. The latter is widely used due to its stable nanostructures. In general, covalent bonds (disulfide bonds and ester bonds) and secondary bonds (hydrogen bonds, Van der Waals forces, hydrophobic interactions, π–π stacking, and electrostatic interactions) are involved.[26,27]

Attractively, a drug–drug conjugate (DDC) could remarkably enhance the drug loading capacity and improve the therapeutic efficacy. For example, Zhang *et al.* linked the hydrophilic drug fluorouracil (FdU) and the hydrophobic drug bendamustine (BDM) into an amphiphilic drug-drug conjugate (ADDC) through hydrolyzable ester bonds (Fig. 2A).[49] A stable amphiphilic

 This journal is © The Royal Society of Chemistry 2022

Published on 03 November 2022. Downloaded by Beijing University of Chemical Technology on 9/1/2025 2:07:42 PM.

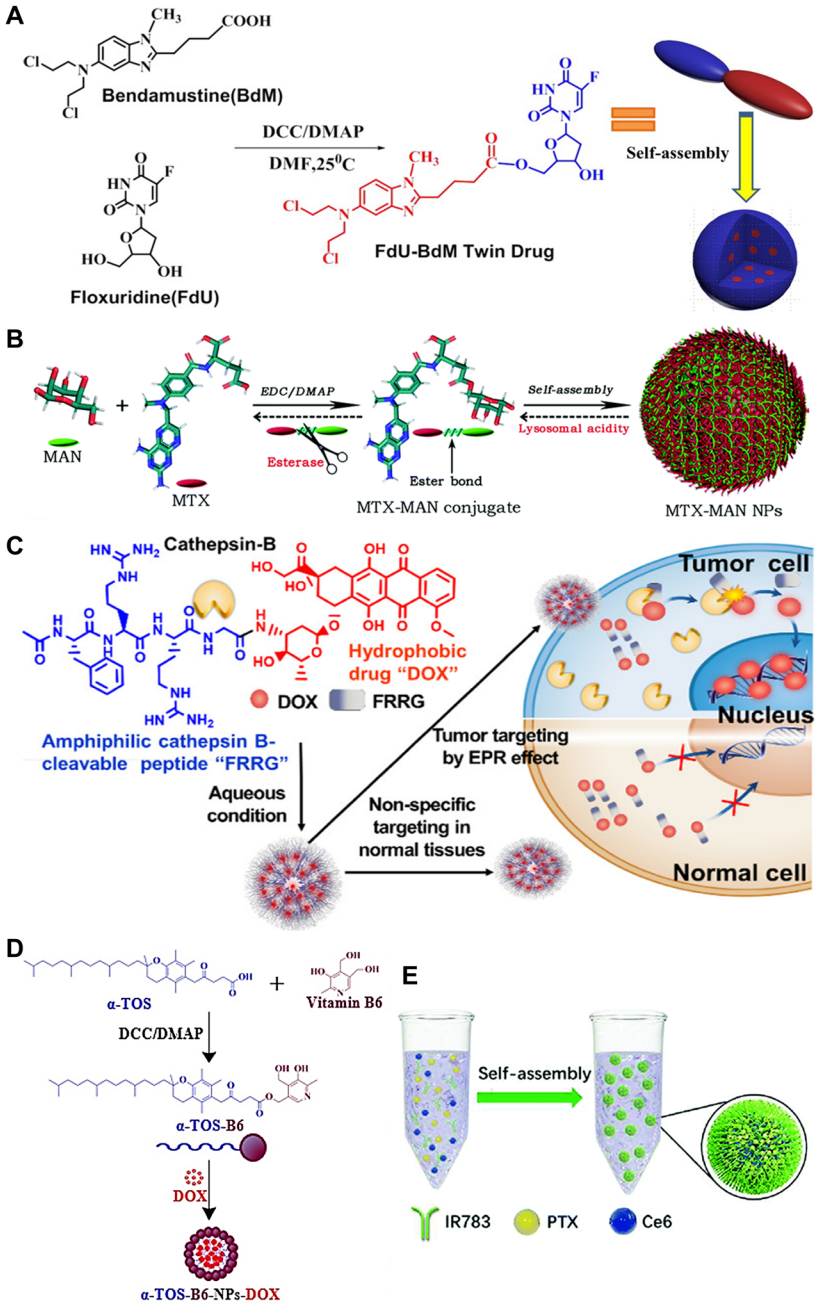


Fig. 2 (A) Self-assembly of FdU–BdM dual drug NPs for cancer therapy. Reproduced with permission from ref. 49. Copyright 2015, American Chemical Society. (B) Co-assembly of carrier-free MTX–MAN NPs with dual-self-recognizing, stimulus-responsive, and MAN-enhanced anti-tumor activity. Reproduced with permission from ref. 61. Copyright 2020, The Royal Society of Chemistry. (C) Preparation and self-assembly of FRRG-DOX NPs for cancer targeting treatment. Reproduced with permission from ref. 62. Copyright 2019, Elsevier. (D) Schematic of the preparation of pH-sensitive nanodrug (α-TOS-B6-NPs-DOX). Reproduced with permission from ref. 67. Copyright 2020, Elsevier. (E) Preparation of Ce6-PTX@IR783 NPs for cancer chemo–sonodynamic therapy *in vivo*. Reproduced with permission from ref. 69. Copyright 2020, The Royal Society of Chemistry.

conjugate could be self-assembled in an aqueous solution. After the FdU–BdM dual-drug NPs were dissociated in the cell, the two pharmacologically active molecules were released; the expression of the caspase-3 protein was greatly activated. The cancer cells were then induced to apoptosis. Similarly, Huang and coworkers synthesized an ADDC from the hydrophilic irinotecan (Ir) and the hydrophobic chlorambucil (Cb) *via* an ester linkage for enhanced cancer synergistic chemotherapy.[50] In another novel idea, inspired by the "Watson–Crick G≡C" base pairing, Chen and coworkers developed a dual-drug,[51] methotrexate (MTX) and 5-fluorouracil (5-FU), which was assembled into amphiphilic MTX-5-FU NPs based on "Watson–Crick G≡C" bonds. The synthesized PEG was modified on the surface of nanodrugs to temporarily shield the targeting function of MTX. Otherwise, hydrophilic drugs and hydrophobic drugs are linked through acid-sensitive amide bonds, Schiff base

Published on 03 November 2022. Downloaded by Beijing University of Chemical Technology on 9/1/2025 2:07:42 PM.

bonds, and disulfide bonds, which have also been widely studied.[45,52–60]

The conjugates of drugs and other small bioactive molecules (carbohydrates, peptides) have also attracted attention, besides pure DDC.[54,61–65] The carbohydrate modification on the surface of NPs can facilitate tumor specific recognition.[66] Mannose (MAN) and MTX are tumor-targeting ligands with an anti-tumor effect. The conjugate of MAN and chemotherapeutic drugs has been extensively studied.[61,64] For example, Fan *et al.* conjugated the hydrophobic anticancer drugs MTX and hydrophilic MAN into MTX-MAN assembly through an esterification reaction (Fig. 2B).[61] The carrier-free nanodrug prepared by a dual-ligand targeting strategy has simple assembly components, powerful functions and excellent anti-tumor effects. Conjugating MAN and different chemotherapeutic drugs can achieve synergistic efficacy. Similarly, Zuo and coworkers connected MAN and DOX through a ROS-sensitive thioketal linker.[64] During the assembly process, indocyanine green (ICG) was wrapped, and the optical/ROS cascade response was realized.

In addition to carbohydrates, the conjugation of short peptides enriches the assembly of carrier-free nanodrugs.[62,65] As small molecules, short peptides have become a research spotlight, which can be modified to drugs to serve as cleavage sites for the assembly. This means that peptide–drug conjugates are an emerging assembly to form nanodrugs. For instance, Shim *et al.* coupled short peptide Phe–Arg–Arg–Gly (FRRG) with DOX to prepare DOX prodrug conjugates (FRRG-DOX) (Fig. 2C).[62] The amphiphilic FRRG-DOX prodrug conjugates self-assembled into NPs. Cathepsin B could cleave the short peptide FRRG. Cathepsin B is highly expressed in tumor cells, which could specifically cleave the FRRG-DOX prodrug. The cleaved DOX entered the tumor nucleus and killed it. As another example, Hu *et al.* chose MMP-2 as the cleavable peptide (GPLGVRGDK, pepA) to develop MMP-2 cleavable self-delivery NPs (MA-pepA-Ce6 NPs) by conjugating an acidic-sensitive small-molecule PD-L1 inhibitor (Metformin, MET) with photosensitizer Ce6.[65] Binding of peptides can alter the physical and chemical properties of drugs and target tumor-specific receptors as cleavage sites, adding functionality to the design of conjugates. Based on these advantages, the carrier-free peptide–drug conjugates will be a promising cancer targeting therapy.

Undoubtedly, amphiphilic carrier-free assemblies can be utilized as carriers and surfactants for other hydrophobic drugs due to their superior amphiphilic properties.[63,67,68] For example, water-soluble vitamin B6 and fat-soluble vitamin E succinate (α-TOS) were coupled into an amphiphilic single molecule, which then self-assembled into nanocarriers (α-TOS-B6-NPs) for the hydrophobic drug DOX (Fig. 2D).[67] A single amphiphilic drug can also be used as a surfactant for another drug. For example, the amphiphilic drug irinotecan hydrochloride (CPT11) is a prodrug of the active parent drug (SN38). Hu and coworkers dissolved the two drugs together in an organic solvent and added water to form a stable nano-dispersion.[68] They found that CPT11, as a surfactant, self-assembled with insoluble SN38 to form stable water-dispersed NPs, which increased the water solubility of SN38 by thousands of times. Thus, amphiphilic carrier-free nanodrugs as carriers or surfactants exhibit new insight into the construction of carrier-free nanodrug platforms.

Furthermore, the conjugate of drugs and organic dyes confers the nanodrugs a highly synergistic chemotherapy/phototherapy.[69–72] Two combination patterns are included: (i) hydrophilic dyes and hydrophobic drugs, and (ii) hydrophilic drugs and hydrophobic dyes. For the first pattern, ICG is one of the near-infrared (NIR) imaging dyes used in medical imaging and clinical diagnosis. Lin *et al.* developed carrier-free nanodrugs (PTX/ICG NDs) composed of paclitaxel (PTX) and ICG.[16] The PTX/ICG NDs exhibited chemo-photothermal synergistic therapy in tumors. For the second pattern, the hydrophobic drug PTX, the hydrophilic dye IR783, and the hydrophobic dye Ce6 were assembled into a nanodrug system (Ce6-PTX@IR783) (Fig. 2E).[69] Organic dye IR783 could realize photoacoustic imaging in sonodynamic therapy (SDT). Ce6 acted as the photosensitizer and sound sensitizer. They endowed the system with the synergistic effect of chem-sonodynamic and photoacoustic imaging performance. The ''hydrophilic–hydrophobic'' carrier-free nanodrugs are the most researched due to their superior amphiphilicity and easy operation. They have shown excellent applications in drug response release, controlled release, and inhibition of multidrug resistance.

2.2 ''Organic–inorganic'' components

Since cisplatin was developed and utilized as an anticancer drug, inorganic anticancer drugs have aroused great interest as a new class of anticancer drugs.[73–75] The anti-tumor activity of compounds of platinum, ruthenium, gallium, copper and other metal elements has gradually been discovered. Moreover, selenium, known as the ''king of anti-cancer'' in human trace elements, also has excellent anti-cancer effects.[76–81] Although inorganic anti-cancer drugs have marvelous anti-cancer effects, some problems such as strong toxic and side effects, poor targeted drug delivery and targeted release ability still inevitably exist. In order to solve these problems, their delivery usually relies on polymeric carrier materials or porous materials first, which make the problem much more complicated as the inevitable potential toxicity of carrier materials. Consequently, the assembly of inorganic anti-cancer drugs into carrier-free nanodrugs has become a new delivery system. Inorganic agents can integrate with organic agents to form ''organic–inorganic'' carrier-free nanodrugs, reducing the negative effects of inorganic agents and enhancing the therapeutic effect of cancer.

2.2.1 ''Hydrophobic–hydrophobic'' assemblies. Inorganic anticancer components are usually hydrophobic, thus combining with hydrophobic organic anticancer drugs to form ''hydrophobic–hydrophobic'' conjugates is a general strategy.[82–87] Two patterns are involved: (i) formation of metal complexes between inorganic metal ions and organic drugs through metal ligands; (ii) direct assembly of inorganic anticancer agents with organic drugs.

Platinum drugs are very common inorganic metal complexes in anti-tumor therapy. In clinical practice its potent anti-tumor effects coexist with significant toxic side effects.[88] Carrier-free nanodrugs may be a potential strategy to mitigate their toxic

 This journal is © The Royal Society of Chemistry 2022

Published on 03 November 2022. Downloaded by Beijing University of Chemical Technology on 9/1/2025 2:07:42 PM.

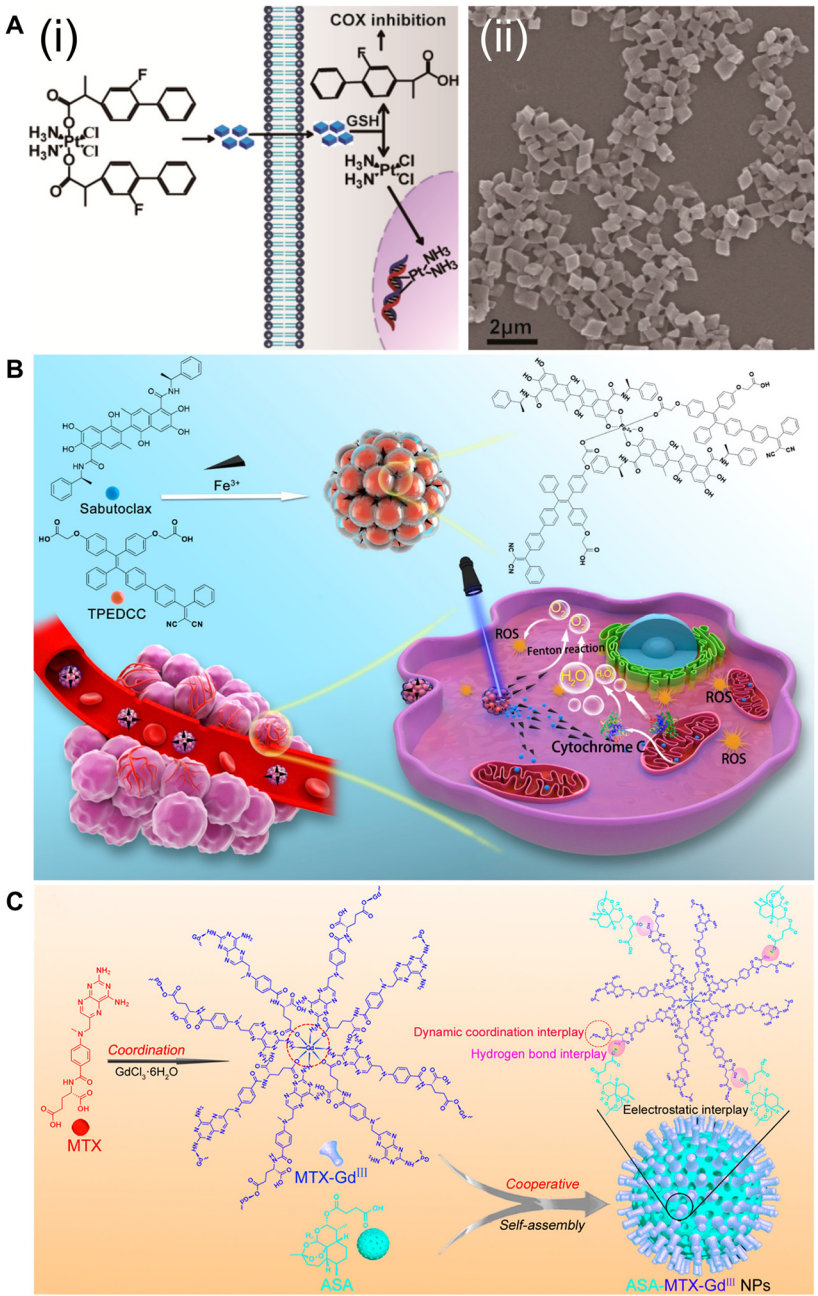


Fig. 3 (A) (i) Preparation of platin-FP. (ii) SEM of platin-FP. Reproduced with permission from ref. 82. Copyright 2018, American Chemical Society. (B) Formation of hybrid nanospheres (TPEDCC, sabutoclax, Fe^{3+}). Reproduced with permission from ref. 83. Copyright 2020, American Chemical Society. (C) Preparation of carrier-free Gd-coordinated theranostic nanoplatforms for amplification of ROS and enhanced chemodynamic chemotherapy. Reproduced with permission from ref. 84. Copyright 2020, American Chemical Society.

effects and enable synergistic therapy. Tan and coworkers reported carrier-free platinum(IV) prodrug NPs self-assembled in an aqueous solution (Fig. 3A).[82] The SEM showed the size and morphology of platin-FP (Fig. 3A). The hydrophobic COX inhibitor flurbiprofen (FP) and *cis*, *cis*, *trans*-[Pt(IV)$(NH_3)_2Cl_2(OH)_2$] axially coordinated to form a new conjugate, which could be spontaneously assembled into carrier-free NPs in water.[82] The conjugate had significantly enhanced cytotoxicity and apoptosis-inducing ability of all tumor cell lines including cisplatin-resistant cells. This indicates that the conjugation of organic drugs with platinum drugs greatly improve the bioavailability of inorganic hydrophobic drugs, resulting in better anti-tumor efficacy.

Additionally, the Fenton inorganic chemical reaction is undoubtedly an effective option for assembling inorganic anti-cancer drugs into carrier-free nanodrugs. Chemodynamic therapy (CDT) has emerged as an effective strategy for cancer treatment, which focuses on killing cancer cells by converting internal H_2O_2 into highly toxic ROS through the Fenton inorganic chemical reaction.[89] However, the efficiency of CDT is

Published on 03 November 2022. Downloaded by Beijing University of Chemical Technology on 9/1/2025 2:07:42 PM.

still limited by endogenous H_2O_2 deficiency and Fenton reaction conditions in the tumor microenvironment. Herein, how to increase the drug payload, improve tumor targeting, and expand ROS are important challenges. For example, Shi and coworkers designed hybrid nanospheres containing Fe^{3+}, aggregation-induced emission (AIE) PS, and Bcl-2 inhibitors (Fig. 3B).[83] The assembly mechanism was the self-assembly of aqueous media driven by iron ion coordination. This hybrid nanosphere is a "three-pronged" combination of chemotherapy, phototherapy and CDT in anti-tumor treatment. After the NPs were ingested by tumor cells, Fe^{3+} drove the Fenton reaction, and the intracellular O_2 concentration increased. With the increase of solute concentration, the aggregation of the new photosensitizer AIE-PS increased and the luminescence was gradually enhanced. Sabutoclax inhibited the overexpression of Bcl-2. The hybrid nanosphere solved the problems of the inherent ACQ effect of traditional photosensitizers, the existence of anti-apoptotic proteins in cells, and the severe hindrance of PDT efficiency caused by hypoxia in the tumor microenvironment. In a similar manner, Fan and coworkers developed supermolecular self-assembly through metal coordination for ROS amplification and enhancing chemotherapy (Fig. 3C).[84] MTX, Gadolinium (Gd) and Artesunate (ASA) were assembled into a self-targeting carrier-free organometallic nanodrug (ASA–MTX–Gd^{III}). In the assembly, Gd was used as a magnetic resonance contrast agent to achieve magnetic resonance imaging (MRI). This metal nanodrug effectively realizes MRI and tumor targeted chemotherapy. In addition to Gd, Fe can also be used for MRI.[85] Tu *et al.* synthesized a metal–organic intermediate (MTX–Fe^{III}) with a network structure through the coordination of MTX and Fe^{III} ions.[85] Fe^{III} ions endowed nanodrugs with the properties of MRI. Another common metal coordination ion is Cu^{2+}.[86] Hence, the co-assembly of photosensitizers and chemotherapeutics through metal coordination to construct "organic–inorganic" carrier-free nanodrugs has great potential in cancer treatment.

Recently, many researches have been devoted to the development of other transition metal complexes with more efficient and new mechanisms. The conjugation of metal complexes and carrier-free nanodrugs may become the central theme of bioinorganic chemistry.

2.2.2 "Hydrophilic–hydrophobic" assemblies. Few carrier-free nanodrugs with "hydrophilic–hydrophobic" systems have been reported, which is determined by the hydrophobic properties of most organic anticancer drugs and inorganic anticancer ingredients. Nevertheless, the conjugation of organic and inorganic in "hydrophilic–hydrophobic" carrier-free nanodrugs is still under investigation.[90–92]

Inorganic nonmetallic selenium works through forming specific diselenium bonds. Li *et al.* added a typical luminous substance, tetrastyrene (TPE) with AIE properties, to a diselenide system (Fig. 4A).[90] They developed a carrier-free selenium-containing assembly with AIE properties. The diselenide bond in the assembly could be cleaved to form selenic acid under γ-radiation. Selenic acid increased the level of ROS in cancer cells and had anticancer activity. The conjugation of the AIE group further endowed the bioimaging capability of the selenium-containing assembly, and realized the combination of cancer radiotherapy and chemotherapy.

Cisplatin cross-linked PA (CPPA) NPs were generated by reacting the cisplatin hydrolysis product *cis*-dihydrate imine platinum(II) with the phosphate group on PA (Fig. 4B).[91] The residual phosphoric acid group on CPPA could achieve bone-targeted therapy by chelating with bone tissue, especially the calcium ion on the surface of bone resorption. CPPA NPs released *cis*-dihydrate platinum(II) and PA under acidic conditions. Cancer cells were effectively killed. Tumor-related osteolysis was inhibited by down-regulating the production of osteoclasts. This strategy proposes insights on carrier-free nanodrugs conjugating organic and inorganic drugs.

Moreover, the remaining novel inorganic components have been designed as carrier-free drugs. As an illustration, Li *et al.* proposed a novel PDA-coated NIR-responsive "bomb-like" carrier-free nanosystem (DNPs/N@PDA).[92] DOX NPs (DNPs) were prepared and then polydopamine film (PDA) was coated on the surface to achieve a long cycle and a near infrared light and heat response. At the same time, NH_4HCO_3 was introduced into the NPs. Under NIR radiation, CO_2 and NH_3 produced by the photothermal decomposition of NH_4HCO_3 can damage the PDA membrane. Then, due to the strong NIR absorption of the PDA film and high light-to-heat conversion efficiency, the loaded DOX is released in a "bomb-like" manner, and the system thus realizes the synergistic effect of chemotherapy and photothermal therapy.

Inorganic anti-cancer drugs such as platinum and ruthenium have defects when acting alone due to their hydrophobicity and toxicity. Organic active ingredients have the merits of designability, versatility and responsiveness. Inorganic drugs and some hydrophilic or hydrophobic drugs, organic photosensitizers, and targeting ligands are co-assembled into "organic–inorganic" carrier-free nanodrugs, which is an encouraging assembly strategy for the synergistic treatment. Fe and Cu mainly form metal complexes with organic drugs or organic active ingredients (organic photosensitizers, organic targeting agents, peptides, carbohydrates). Although few researches on the assembly of hydrophilic organic components and inorganic components are involved, we believe that the strategy has great merits and will attract widespread attention. It will provide more methodologies for the development of novel carrier-free nanodrugs containing inorganic components.

2.3 "Inorganic–inorganic" components

Further research on the mechanism of action of inorganic antitumor drugs, the design and synthesis of new high-efficiency and low-toxicity anti-tumor compounds are the current focus. With the ceaseless research of "organic–organic" and "organic–inorganic" carrier-free nanodrugs, new types of carrier-free nanodrugs are explored. "Inorganic–inorganic" carrier-free nanodrugs are composed of multiple "inorganic" drugs. For instance, Xin and coworkers developed a multi-drug nanocomposite (PtAs) synthesized from cisplatin (CDDP) and arsenic trioxide (ATO) prodrugs through the reverse microemulsion method (Fig. 5).[93] To improve the water solubility and

 This journal is © The Royal Society of Chemistry 2022

Published on 03 November 2022. Downloaded by Beijing University of Chemical Technology on 9/1/2025 2:07:42 PM.

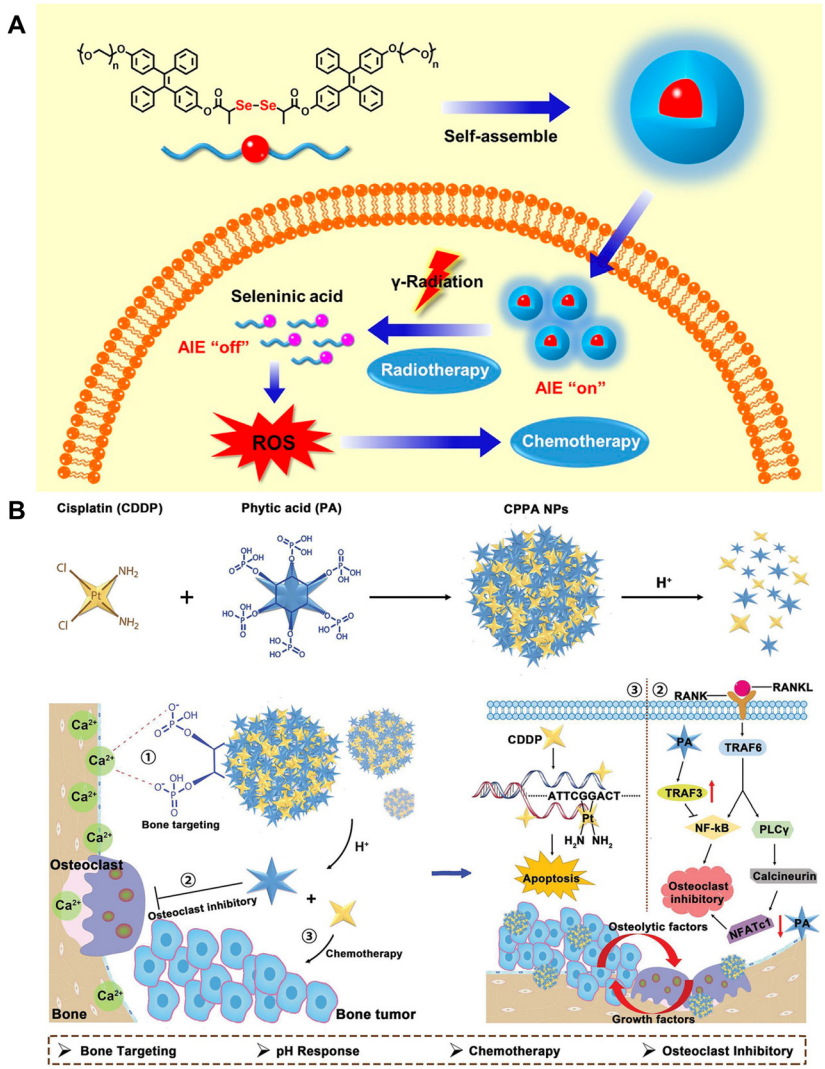


Fig. 4 (A) Preparation of selenium-containing AIE assemblies for cancer radiotherapy and chemotherapy. Reproduced with permission from ref. 90. Copyright 2020, American Chemical Society. (B) Preparation of CPPA NPs with bone targeting, anti-cancer and anti-osteoclastogenesis activities for cancer treatment. Reproduced with permission from ref. 91. Copyright 2020, Wiley.

biocompatibility of the nanocomposite, the system adopted layer-by-layer assembly technology to coat the oppositely charged polyelectrolyte molecules on the nanocomposite. Although organic polymer coatings are used, they are still catalogued under inorganic–organic carrier-free nanodrugs because we wanted to give an incentive for this item. This research has opened a way for enriching the "inorganic–inorganic" carrier-free nanodrugs. The construction of "organic–organic" and "organic–inorganic" carrier-free nanodrugs will provide sufficient experience and methods for "inorganic–inorganic" carrier-free nanodrugs.

As more and more inorganic anti-tumor drugs are being developed, carrier-free nanodrugs are increasingly being studied. More inorganic drugs will be applied to "inorganic–inorganic" carrier-free nanodrugs. Inspired by the secondary classification of "organic–organic" and "organic–inorganic" system, we believe that "inorganic–inorganic" carrier-free nanodrugs will introduce more mature ideas in the future. Although there is still a gap in the clinical application of inorganic drugs, a second classification based on the hydrophilic/hydrophobic nature of the inorganic components might be possible to make the carrier-free nanosystem more comprehensive.

2.4 Application of carrier-free nanodrugs

Carrier-free nanodrugs are widely utilized in anti-tumor therapy. Chemotherapy has the merits of systemic therapy and high efficacy, but the multiple drug resistance (MDR) of tumor cells and the toxic and side effects of chemotherapy drugs on normal cells cannot be ignored. Carrier-free nanodrugs enable synergistic chemotherapy to be achieved and inhibit the multi-drug resistance of tumors or reduce the toxic side effects of chemotherapy toward normal cells. For example, the hydrophobic drug PTX and the hydrophilic anti-tumor tyrosine peptide (YSV) were combined into a Taxol-EYSV conjugate connected by an ester bond.[94] The conjugate was self-hydrolyzed to form a carrier-free hydrogel. Experiments showed that the Taxol-EYSV

Published on 03 November 2022. Downloaded by Beijing University of Chemical Technology on 9/1/2025 2:07:42 PM.

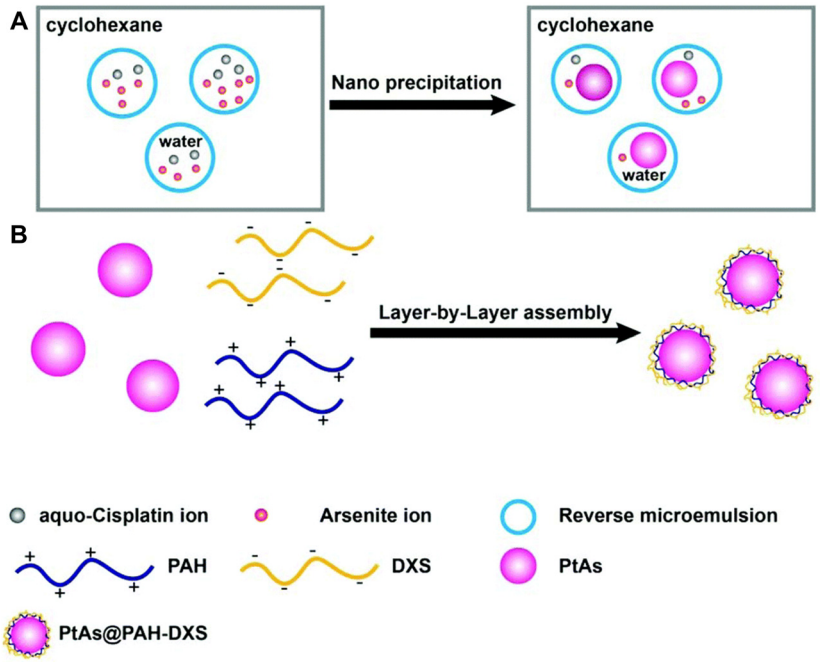


Fig. 5 Formation of (A) PtAs NPs and (B) PtAs@PAH-DXS nanodrugs. Reproduced with permission from ref. 93. Copyright 2019, The Royal Society of Chemistry.

hydrogel had an enhanced anti-tumor effect and conquered tumor multi-drug resistance.

For NPs, the hydrophilic anticancer drug irinotecan (Ir) and hydrophobic anticancer drug MMB were linked by a carbonate bond to prepare an ADDC, which showed synergistic chemotherapy in tumor cells.[52] Similarly, celastrol (CST) and DOX were assembled into carrier-free nanodrugs for synergistic chemotherapy (Fig. 6A).[32] In addition, tumor targeting ligands and chemotherapeutic drugs can be conjugated to achieve synergistic targeted chemotherapy. Commonly used targeting ligands include folic acid (FA), hyaluronic acid (HA), transferrin, RGD peptides, and monoclonal antibodies.[91,95–103] There are many targets at the tumor site, and choosing the right target is crucial for constructing carrier-free nanodrugs.

PDT, PTT, and SDT are emerging therapies for cancer. The combined therapy strategy with chemotherapy is considered to be encouraging.[37–41,72,104] Organic NIR dyes (such as ICG, IR-780, IR-820) as photothermal agents are doped into carrier-free nanodrugs to develop photothermal effects.[105] In the study of He *et al.*, IR-780 and CPT were modified to IR780-LA and CPT-ss-CPT respectively to overcome the disadvantage that the original drug cannot be co-assembled.[106] IR780-LA and CPT-ss-CPT are co-assembled into IR780-LA/CPT-ss-CPT-NPs with a good synergistic PTT/chemotherapy effect. Moreover, in Fig. 2E, a carrier-free nanodrug (Ce6-PTX@IR783) assembled by Ce6, PTX, and IR783 for synergistic chemo–sonodynamic cancer therapy.[69] Ce6 was a commonly used photosensitizer and SDT sensitizer. Extracorporeal ultrasonic irradiation decomposed nanodrug to release PTX and Ce6, and the synergistic treatment of chemotherapy and SDT was realized.[69]

NIR photothermal dyes can be used as fluorescent agents to achieve NIR imaging of tumors *in vivo* as well as being a photothermal agent. *In vivo* imaging provides a new approach for early detection and treatment monitoring of tumor lesions and makes sense for clinical diagnosis and treatment of cancer patients.[107–111] Photoacoustic imaging (PAI) is a rapidly developing non-invasive and non-radiation imaging method.[112,113] IR783 can realize PAI (Fig. 2E). Ce6-PTX@IR783 combines the high resolution of optical imaging and the high penetration of ultrasonic imaging.[69] The mix of hydrophobic fluorescent dyes is more universal.[16,85,114–116] MTX-CPT nanoparticles doped with the NIR fluorescent dye DiR (Fig. 6B).[116] NPs became effective probes for NIR/PAI. Tumor self-monitoring with a fluorescent "switch" effect was realized.[116] At normal pH, the self-assembled structure of MTX-CPT NPs inhibited the fluorescence of DiR, which had an "off" effect. When the NPs entered the low pH tumor environment, the ester bonds of the NPs were broken, and the self-assembled structure was disassembled. The fluorescence of DiR was no longer suppressed and had an "on" effect. Therefore, MTX-CPT NPs became the "switch" of fluorescence. Drug release was monitored in real-time by tumor imaging. This strategy, which can monitor drug release in real-time or track cancer cells through the nanodrug itself, will become a spotlight. The prominent effect of PTT has also attracted much attention. The photosensitizers or luminophores with AIE characteristics were incorporated into carrier-free nanodrugs to achieve PTT and synergistic therapy.[83,90]

"Organic–inorganic" and "inorganic–inorganic" carrier-free nanodrugs contain inorganic assemblies. Most of them are utilized in synergistic chemotherapy, phototherapy, tumor imaging and overcoming multidrug resistance. Metal ions (Gd, Fe, Cu) form metal complexes with drugs to endow nanodrugs with nuclear MRI.[84,85] The application of carrier-free nanodrugs in

 This journal is © The Royal Society of Chemistry 2022

Published on 03 November 2022. Downloaded by Beijing University of Chemical Technology on 9/1/2025 2:07:42 PM.

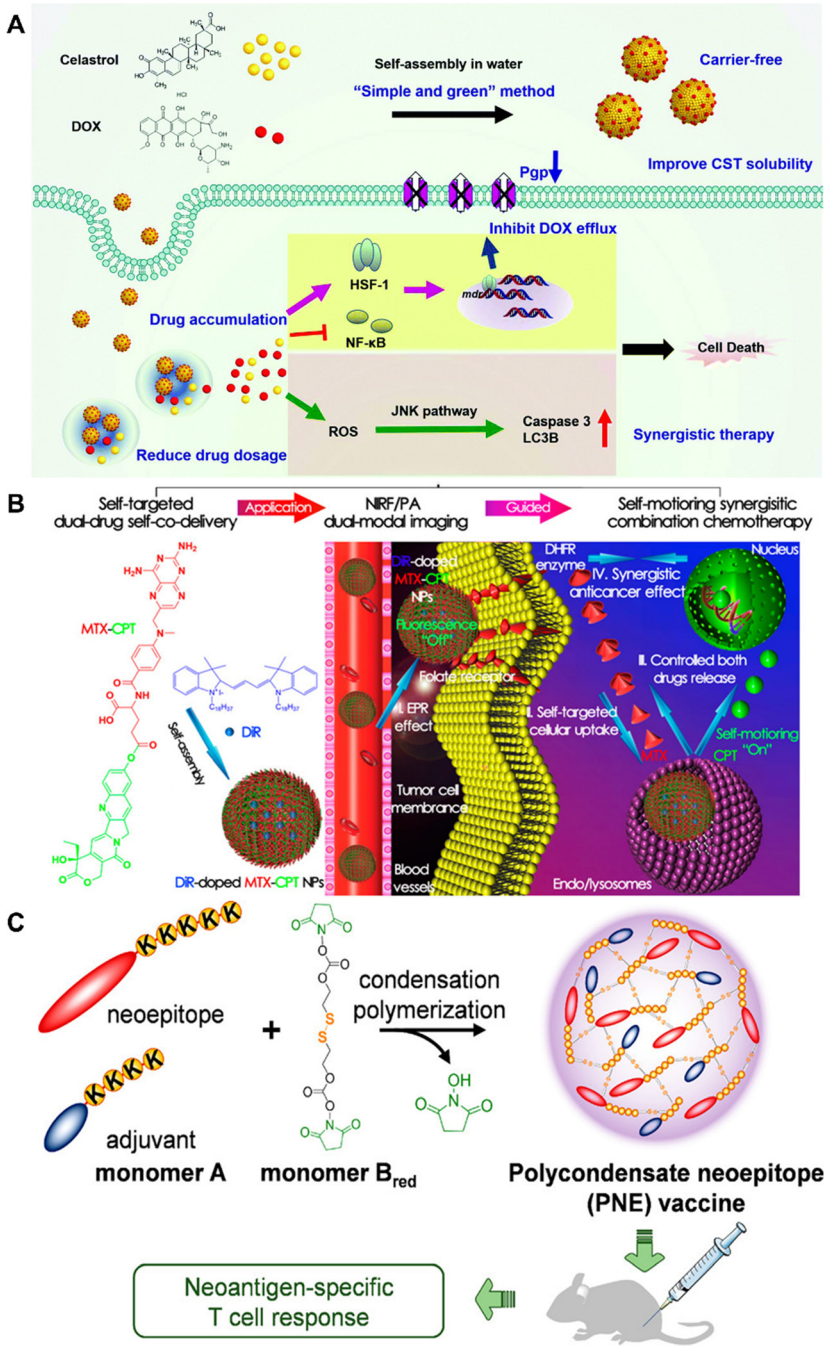


Fig. 6 (A) Self-assembly of the Celastrol (CST)/DOX NPs reverse drug resistance in MCF-7/ADR cells. Reproduced with permission from ref. 32. Copyright 2018, The Royal Society of Chemistry. (B) Co-assembly of DiR-doped MTX-CPT NPs. Reproduced with permission from ref. 116. Copyright 2017, American Chemical Society. (C) Synthesis, responsive release, and *in vivo* fate of polycondensate neoepitope (PNE) vaccines. Reproduced with permission from ref. 124. Copyright 2020, American Chemical Society.

tumor imaging, real-time monitoring and synergistic treatment effect provides strong support for its development. The excellent effect of inorganic components may increase its participation in carrier-free nanodrugs in the future, which will be a new trend.

Immunotherapy has been highly investigated in recent years. It effectively kills tumor cells by activating the immune system and preserves the long-term memory of tumor antigens.[65,117–121] Cancer immunotherapy mainly includes cancer vaccines, immune checkpoint inhibitors, adoptive cellular immunotherapy and monoclonal antibodies.[122,123] A PNE vaccine delivery platform was developed through a reversible polycondensation reaction (Fig. 6C).[124] The platform used a synthetic long peptide (SLP) containing a new epitope and multiple amino groups as a monomer (monomer A) to mix with another reactive bifunctional monomer (monomer B). PNE quickly released new epitopes in response to intracellular

Published on 03 November 2022. Downloaded by Beijing University of Chemical Technology on 9/1/2025 2:07:42 PM.

reducing activity after entering the body and being internalized by antigen-presenting cells (APCs). The endosomes of peptide antigens were promoted to escape and transfer to the cytoplasm. Experiments showed that the PNE vaccine could significantly promote the functional expression of effector cells and had a significantly enhanced anti-tumor effect. This vaccine delivery platform will be a powerful boost in the field of precise and personalized vaccine design and cancer treatment. Moreover, co-delivery of chemotherapeutics and immunostimulant for chemoimmunotherapy is a novel strategy in tumor therapy. As an example, Du *et al.* loaded polyriboinosinic:polyribocytidylic acid (Poly I:C) onto the PTX nanorods (PNRs) and then coated D-mannuronic acid (MA) to form MA-PNRplex for mannose-receptor targeting.[125] MA-PNRplex was internalized *via* cavesomes bypassing endo-lysosomes, then release PTX and Poly I:C. Subsequently, poly I:C stimulated the secretion of chemokines and cytokines through the RIG-I pathway and recruited immune cells to poison cancer cells. Ultimately, two pathways synergistically enabled chemoimmunotherapy. As such, this strategy is highly effective and potentially maximises chemoimmunotherapy.

At present, carrier-free nanodrugs are mainly applied to anti-tumour therapy, with anti-bacteria and anti-inflammatory gradually gaining ground. For instance, Teng and coworkers loaded anti-miR155 onto baicalein nanorods, and then coated them with sialic acid to target macrophages.[126] Using the targeted co-delivery of anti-miR155 and anti-inflammatory baicalein to polarize macrophages from the M1 phenotype to the M2 phenotype for alleviating inflammatory response and treating atherosclerosis (AS). M1 macrophages are pro-inflammatory cells that induce inflammatory activities by secreting pro-inflammatory cytokines and ROS. M2 macrophages are an anti-inflammatory phenotype characterized by high expression of scavenging molecules, mannose and galactose receptors, ornithine and polyamines. The active protein and miRNA reach the cell by bypassing the lysosome to treat AS. Recently, metal-NSAIDS (nonsteroidal anti-inflammatory drugs) based tumor treatment strategies have achieved considerable results. Xing *et al.* exerted synergistic anti-tumour and anti-inflammatory effects by mediating the inflammatory microenvironment in solid tumours to repair the tumor inflammatory environment and enhance tumour cell chemotherapy sensitivity (Fig. 7A).[127] The carrier-free self-delivered nanoprodrug (named Tolfplain) is constructed based on platinum(II) coordination bonding coupled with tolfenamic acid (Tolf). Cisplatin-based sequential chemotherapy can further increase inducible COX-2 expression in tumours

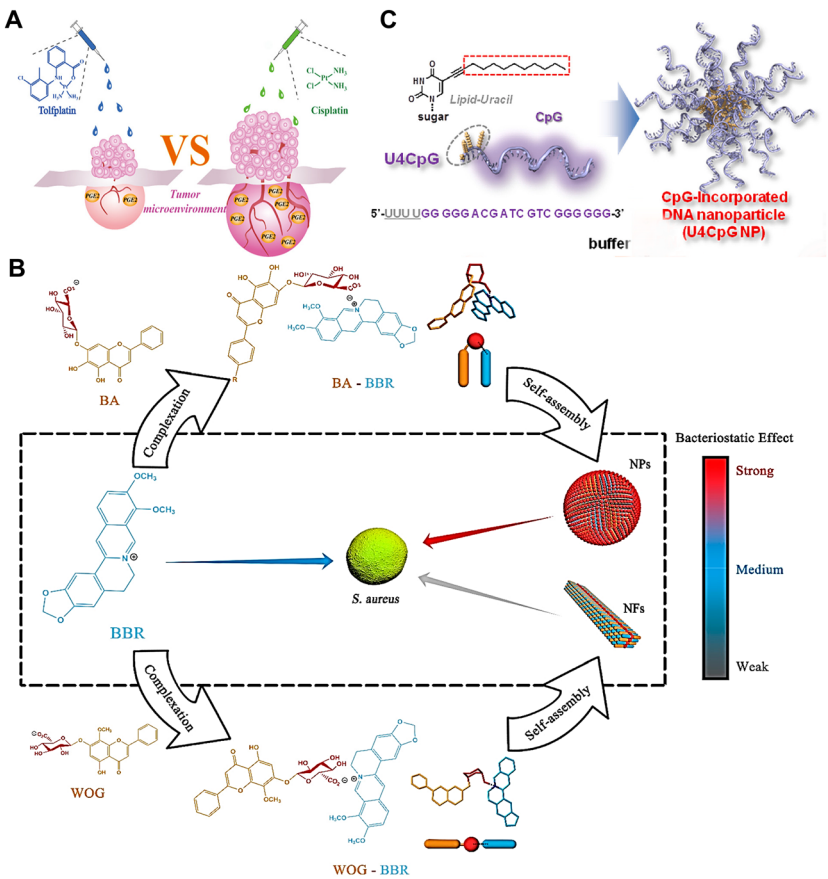


Fig. 7 (A) Comparison of the therapeutic effects of carrier-free self-delivered nanoprodrug Tolfplain and Cisplatin. Reproduced with permission from ref. 127. Copyright 2021, Elsevier. (B) Self-assembly of BA-BBR (berberine) NPs and WOG-BBR NPs. Reproduced with permission from ref. 129. Copyright 2019, American Chemical Society. (C) Schematic process for CpG-ODN incorporation into DNA-based NP (U4CpG) for promoting anti-HIV immunity. Reproduced with permission from ref. 131. Copyright 2021, Elsevier.

 This journal is © The Royal Society of Chemistry 2022

Published on 03 November 2022. Downloaded by Beijing University of Chemical Technology on 9/1/2025 2:07:42 PM.

Table 1 Summary of the compositions and applications of carrier-free nanodrugs

Carrier-free nanodrug		Drug components	Surface functionalize	Force	Target	Trigger	Application	Ref.
"Organic–organic"	Hydrophobic-Hydrophobic	PTX, ICG	—	Hydrophobic interactions, π–π stacking interactions	EPR	pH	NIR bioimaging, chemo-photothermal synergistic therapy	16
		HCPT, DOX	—	Hydrophobic interactions	EPR	pH	Synergistic chemotherapy	30
		HCPT, DOX	—	Hydrophobic interactions, π–π stacking interactions	EPR	pH	Inhibit drug resistance	31
		CST, DOX	—	Electrostatic, hydrophobic interactions, π–π stacking interactions	EPR	pH	Synergistic chemotherapy, reverse multidrug resistance	32
		HCPT, Ce6	—	Hydrophobic interactions, π–π stacking interactions	EPR	Laser	Chemo-photodynamic therapy	33
		Asp, UA	—	Hydrogen bond, hydrophobic interactions	EPR	pH	Cancer Metastasis Therapy	34
		IND-OE, DOX	—	Ester bond	EPR	pH	Chemotherapy, reverse multidrug resistance	35
		DOX, Ce6	—	Electrostatic, hydrophobic interactions, π–π stacking interactions	EPR	pH	Chemo-photodynamic therapy	36
		SN38, Ce6	—	Hydrophobic interactions, π–π stacking interactions, hydrogen bonds	EPR	pH	Chemo-photodynamic therapy	37
		DOX, Ce6	mPEG-PC	Electrostatic, hydrophobic interactions, π–π stacking interactions	EPR	Light	Chemo–photodynamic therapy	38
		ATO, Ce6	—	Hydrophobic interactions, π–π stacking interactions	EPR	pH	Photodynamic therapy	39
		ICG, SN38, PTX	—	Hydrophobic interactions, π–π stacking interactions	Endocytosis, micropinocytosis	pH	Chemo-photo therapy	40
		Cur, perylene, and H_2TPyP	—	π–π stacking interactions	EPR		Chemo-photodynamic therapy	41
		Bortezomib (BTZ), PPa	DSPE-PEG	π-Cation interaction, π–π stacking interaction, hydrophobic force and hydrogen bond	EPR	pH	Photodynamic therapy	42
		PTX, citronellol (CIT)	DSPE-PEG	Disulfide bond	EPR	GSH, ROS	Chemotherapy	43
		Docetaxel (DTX), Oleic acid (OA)	—	Disulfide bond	EPR	GSH	Chemotherapy	45
		PR104A, PPa	DSPE-PEG	Thioether or thioketal linkage	EPR	Light	Photodynamic, hypoxia-activated therapy	46
		DOX, digoxin (DIG)	Cancer cell membranes	Hydrophobic interactions	EPR, A549 cells	pH	Synergistic chemotherapy	47
		Ce6, DiR	Red blood cell membranes	π–π stacking interactions, charge interactions	EPR	Laser	PTT/PDT	48
		DOX, UA	HER2 aptamer	Electrostatic interactions	HER2 over-expressing cancer cells	pH	Chemotherapy	99
		EPI, ICG	DSPE-MPEG	Electrostatic, hydrophobic interactions, π–π stacking interactions	EPR	pH, laser	Chemo-photothermal therapy	114
		Rapamycin (Rapa), (+)-JQ1, IR783	—	Protein–protein interaction	EPR	Laser	Chemo-immunotherapy, PTT/PDT	120
"Organic–organic"	Hydrophilic–hydrophobic	FdU, BdM	—	Ester bonds	EPR	pH	Synergistic chemotherapy, overcome the multidrug resistance (MDR)	49
		Irinotecan (Ir), chlorambucil (Cb)	—	Ester bonds	EPR	pH	Synergistic chemotherapy, overcome MDR	50
		MTX, 5-FU	mPEG	Watson–Crick G ≡ C, hydrogen bond	FA	pH	Synergistic chemotherapy	51

This journal is © The Royal Society of Chemistry 2022

Published on 03 November 2022. Downloaded by Beijing University of Chemical Technology on 9/1/2025 2:07:42 PM.

Table 1 (*continued*)

Carrier-free nanodrug	Drug components	Surface functionalize	Force	Target	Trigger	Application	Ref.
	Ir, Melampomagnolide B (MMB),	—	Carbonate bond	EPR	pH	Combination chemotherapy	52
	MTX, CPT	—	Ester bonds, hydrogen bonds	EPR, FA	pH	Combination chemotherapy	53
	Ir, vitamin E succinate (VES)	—	Ester bonds	EPR	pH, esterase	Synergistic chemotherapy	54
	CPT, floxuridine (FUDR)	—	Ester bonds	EPR	pH	Synergistic chemotherapy	55
	FUDR, pseudolaric acid B (PAB)	—	Ester bonds	EPR	pH	Synergistic chemotherapy	56
	Gemcitabine (Gem), Cb, Ir	—	Ester bonds	EPR	pH	Synergistic chemotherapy	57
	Melampomagnolide B (MMB), CPT,	—	Carbonate bonds	EPR	pH	Synergistic chemotherapy	58
	MTX, ICG	clofarabine (CA)	Watson-Crick A = T	EPR, FA	pH, laser	NIR-II imaging-guided photo-chemotherapy	59
	PTX, succinic acid (SA)	PEG	Ester bonds	EPR	pH	Chemotherapy	60
	MTX, MAN	—	Ester bonds	FA, MAN-6-phosphate	pH	Cancer targeting therapy	61
	FRRG, DOX	—	Amide bonds	EPR, cathepsin B	pH, cathepsin B	Cancer targeting therapy	62
	PTX, tetrandrine (Tet), succinic acid (SA), RGD (arginine–glycine–aspartic acid)	—	Ester bonds	EPR, $\alpha_V\beta_3$ integrin	pH	Chemotherapy	63
	ICG, MAN, DOX, thioketal (TK)	MAN	Amide bond, carbohydrate–protein interactions	Lectin	Light, ROS	Photo-chemotherapy	64
	Metformin (MET), Ce6,	—	MMP-2 cleavable peptide (GPLGVRGDK, pepA), Schiff base bonds, imine bonds.	Tumor integrin αvβ3 receptor	pH	Photodynamic-immunotherapy	65
	Borondipyrromethenes (BODIPYs), lactose (LAC)	—	Disulfide bonds	Galactose	GSH, light	Dual phototherapy	66
	DOX, vitamin B6, α-tocopheryl succinate (α-TOS)	—	Charge interaction	EPR, VTC	pH	Cancer synergistic targeted therapy	67
	SN38, CPT11, PTX, CPT	—	π–π stacking interactions	EPR	pH	Chemotherapy	68
	Ce6, PTX, IR783	—	—	EPR	pH	Chemo–sonodynamic cancer therapy, PAI	69
	Gambogic acid (GA), Ce6, FA	—	π–π stacking interactions, electrostatic interactions, hydrophobic interactions	EPR, FA	pH	Chemotherapy-photodynamic therapy	70
	H2TPPS (tetra sodium meso-tetra(sulfonatophenyl)-porphyrin), DOX	—	π–π stacking interactions, electrostatic interactions, hydrophobic interactions	EPR	pH	Reverse multidrug resistance, photodynamic-chemotherapy	71
	Etoposide (VP-16), PPa	DSPE-PEG	Hydrophobic interaction, π–π stacking interaction, hydrogen bonds	EPR	Laser	Photodynamic therapy, DNA damage-augmented	72
	Curcumin (CCM), erlotinib (ELT)	PEG	Ester bonds	EPR, EGFR	pH	Cancer targeting therapy	102
	MTX, HCPT	PEG	π–π stacking interactions, electrostatic interactions, hydrophobic interactions	EPR, FA	pH	Synergistic chemotherapy	103
	FA, DOX	—	Hydrazone bonds	FA	pH	Chemotherapy, cancer targeting therapy	101

This journal is © The Royal Society of Chemistry 2022

Published on 03 November 2022. Downloaded by Beijing University of Chemical Technology on 9/1/2025 2:07:42 PM.

Table 1 (*continued*)

Carrier-free nanodrug		Drug components	Surface functionalize	Force	Target	Trigger	Application	Ref.
		MTX, CPT, DiR	—	Ester bonds	EPR, FA	pH, easterase	NIR fluorescence, PAI, self-active targeted and synergistic chemotherapy	116
"Organic–organic"	Hydrophilic–hydrophobic	DOX, siRNA	PEG	π–π stacking interactions, electrostatic interactions	EPR, PD-L1	pH, easterase	Chemoimmunotherapy, reversing immunosuppression	121
		Synthetic long peptide (SLP), reactive bifunctional monomer (monomer B_{red})	—	—	Lymph nodes (LNs) targeting	Intracellular reduction activity	Cancer Vaccine, immunotherapy	124
		Poly-riboinosinic:*p*olyr-ibocytidylic acid (poly I:C), PTX, β-LG	D-Mannuronic acid	Electrostatic interaction	Mannose-receptor	pH	Chemoimmunotherapy	125
		anti-miR155, baicalein	Sialic acid	Electrostatic interaction	Macrophages	pH	Anti-inflammation	126
		CpG-ODN, lipid-uracil (U)	—	Van der Waals interactions	Cell membrane	—	Anti-virus	131
"Organic–inorganic"	Hydrophobic–hydrophobic	Flurbiprofen, platinum(IV)	—	Ester bonds	EPR	GSH	Enhances cellular uptake and cytotoxicity	82
		Fe^{3+}, TPEDCC, Bcl2-inhibitor (sabutoclax)	—	π–π stacking interactions, coordination bond, hydrogen bond	EPR	pH	Photodynamic therapy	83
		MTX, Gd, ASA	—	Dynamic coordination bond, hydrogen bond	EPR, FA	pH	MRI imaging and tumor theranostics.	84
		ICG, MTX, Fe^{III}	—	Coordination, π–π stacking, electrostatic, hydrophobic interactions	EPR	pH	Magnetic resonance/photoacoustic/fluorescence imaging, photo-chemotherapy	85
		ICG, PhA, Cu^{2+}	—	Electrostatic, π–π stacking, hydrophobic interactions	EPR	pH	Fluorescence/photoacoustic imaging-guided tumor phototherapy	86
		Cur, OA, zinc phthalocyanine (ZnPc)	VE-TPGS	Hydrophobic interactions, π–π stacking interactions	EPR	Light	Chemo-photodynamic therapy	87
	Hydrophilic–hydrophobic	TPE, Se	—	Diselenide bonds	EPR	γ-Radiation	Radiotherapy, chemotherapy	90
		CDDP, PA	—	Hydrophobic interactions	EPR, bone	pH	Cancer targeting therapy, osteoclast inhibitory	91
		DOX, NH_4HCO_3	PDA	Hydrophobic interactions	EPR	Laser, pH	*In situ* on-demand drug release, chemotherapy	92
		Tolfenamic acid (Tolf), platinum(II)	—	Coordination bond	EPR	pH	Anti-inflammation, anti-tumor	127
"Inorganic–inorganic"	Hydrophilic–hydrophobic	CDDP, arsenic trioxide (ATO)	PAH, DXS	—	EPR	pH	Overcome drug resistance, combination therapy	93

This journal is © The Royal Society of Chemistry 2022

Published on 03 November 2022. Downloaded by Beijing University of Chemical Technology on 9/1/2025 2:07:42 PM.

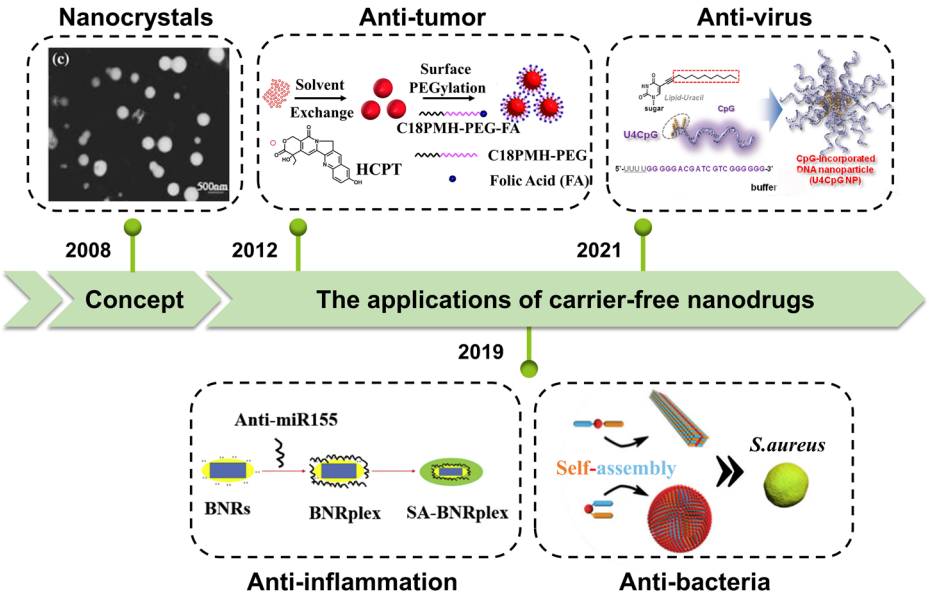


Fig. 8 A schematic overview of the development of carrier-free nanodrugs, including the concept of the "carrier-free" and the progress of carrier-free nanodrug applications. Left to right: Reproduced with permission from ref. 15 Copyright 2008, Springer. The Royal Society of Chemistry. Reproduced with permission from ref. 18. Copyright 2012, The Royal Society of Chemistry. Reproduced with permission from ref. 131. Copyright 2021, Elsevier. Reproduced with permission from ref. 129. Copyright 2019, American Chemical Society.

through NF-κB activation. After internalization, Tolf released by Tolfplain inhibits COX-2 and down-regulates anti-apoptotic and metastasis-related proteins, enhancing cisplatin-induced apoptosis and inhibiting tumour metastasis.

Carrier-free nanodrugs also show surprising effects in antibacterial therapies. A hydrophobic D-α-tocopherol succinate (TS) and a hydrophilic vancomycin (VCM) were prepared into a carrier-free self-assembled drug delivery system *via* supramolecular complexation.[128] It extremely enhanced the anti-bacteria activity against *Staphylococcus aureus* (SA) and Methicillin-resistant *Staphylococcus aureus* (MRSA). Moreover, Li *et al.* prepared a carrier-free nanosystem through a supramolecular self-assembly strategy for anti-bacterial activity (Fig. 7B).[129] Berberine (BBR) is a hydrophobic antibacterial cation derived from natural medicinal plants. The flavonoid glycoside baicalin (BA) and wogonoside (WOG) are also natural medicinal ingredients. BBR was formed with BA and WOG separately into BA-BBR NPs (BA-BBR NPs) and WOG-BBR nanofibers (WOG-BBR NFs). The results displayed that BA-BBR NPs significantly enhanced the antibacterial and biofilm removal abilities. Feng's group developed a carrier-free nanosystem combined silver and antimicrobial photodynamic therapy as well.[130] The photosensitizer 4,4′,4″,4‴-(porphine-5,10,15,20-tetrayl) tetrakis (benzoic acid) (TCPP), MTX, gallic acid (GA) and Poloxamer 407 (Pluronic F127) were composed into a supermolecular nanosystem (TCPP-MTX-NP), then Ag was doped into TCPP-MTX-NP. It showed an excellent antibacterial effect against *Escherichia coli* (*E. coli*) and SA.

To date, carrier-free nanodrugs have been utilized in antivirus therapies. Kim prepared a nano immunostimulant for enhancing immunity against HIV (Fig. 7C).[131] This nucleic acid-based delivery system is a self-assembled CpG nanostructure (U4CpG) formed by a CpG oligodeoxyribonucleotide (ODN) with multiple hydrophobic portions. Interferon (IFN) and IFN-γ in human peripheral blood mononuclear cells (PBMC). The ability of U4CpG to eradicate HIV-1 by enhancing immunity and reversing latency makes it a potential candidate for clinical studies dealing with viral infections.

Given all of that, we summarize and compare the composition and applications of carrier-free nanodrugs, as shown in Table 1. The carrier-free nanodrugs in our review have various application areas (Fig. 8) such as tumor-targeted therapy, CDT, PDT, anti-bacteria, and anti-inflammatory, showing tremendous benefits of combination therapy. Since carrier-free nanodrugs can integrate targeting, imaging, PTT and chemotherapy and excel in overcoming biological barriers, synergistic therapy and reducing adverse effects, it has gradually gained ground in anti-bacteria, anti-inflammation and anti-virus areas. In the antibacterial field, carrier-free nanodrugs will exhibit potential merits in visualizing bacteria, targeting the removal of biofilms, removing drug-resistant bacteria and persistent bacteria, and removing intracellular bacteria. In the field of anti-inflammation, we believe that carrier-free nanodrugs will also manifest the favorable ability to target inflammation, modulate inflammation and synergistic immunity. Moreover, carrier-free nanodrugs can be developed into novel nanobodies with mutation resistance, targeting, low immunogenicity and specificity, showing enormous anti-viral potential. The future development of carrier-free nanodrugs will be more diversified and will showcase enhanced strengths in many medical fields, such as apoplexy, brain infection or tumor, and potential tissue engineering.

3. Conclusion and perspectives

In summary, based on the organic, inorganic, hydrophilic and hydrophobic properties of the assembly module, the

 This journal is © The Royal Society of Chemistry 2022

Published on 03 November 2022. Downloaded by Beijing University of Chemical Technology on 9/1/2025 2:07:42 PM.

construction method and recent research progress of multi-carrier-free nanodrugs is outlined. An overview of the methods for the assembly of multicomponent carrier-free nanodrugs from substances with different properties is presented, helping researchers grasp the characteristics of each carrier-free nanodrug, recognizing its variability and the construction rules. This property-based classification provides additional insight for exploring carrier-free nanodrugs.

Carrier-free nanodrugs have become an encouraging strategy for tumor diagnosis and treatment with the advantages of easy preparation, safety, versatility, high biocompatibility, excellent biodegradability, high drug loading and synergistic therapy. Despite its advantages, it still has limitations due to insufficient research:

(i) Although multiple assembly components bring the effect of synergistic therapy that brings enhanced effects, whether it increases the antagonism, metabolic burden and potential side effects still lack reliable research.

(ii) Active targeting still has restrictions. Most multicomponent carrier-free nanodrugs passively target tumor sites by the EPR effect. However, EPR is greatly affected by the dense extracellular matrix (ECM) and interstitial fluid pressure (IFP). Therefore, how to improve the active targeting of carrier-free nanodrugs or enhance the EPR effect of tumors to promote passive targeting is a challenge.

(iii) Some carrier-free nanodrugs have short blood circulation times and require appropriate surface modifications, such as PEGylation, to extend the circulation time and improve distribution *in vivo*. One should note that the content of surface modification is kept to a minimum. The obtained nanodrugs are suggested to be categorized in the general meaning.

(iv) Multi-functional, multicomponent carrier-free nanodrugs are constantly being developed. Maintaining the multi-functionality of carrier-free nanodrugs without complicating the assembly is the issue that requires attention.

(v) The applications of carrier-free nanodrugs are currently focused on anti-tumor therapies. Still few carrier-free nanodrugs are used in anti-bacterial fields. We believe that the excellent performance of carrier-free nanodrugs in anti-tumor therapy can be extended to anti-bacterial fields. Dual or multi-drug compounds, PDT, SDT, and fluorescence imaging, can all be adopted into antibacterial carrier-free nanodrugs, which will undoubtedly bring new perspectives on anti-bacteria, anti-inflammatory and anti-viral fields. Hence, extensive and further research is necessary to expand the application of carrier-free nanodrugs.

(vi) From laboratory research to clinical diagnosis and treatment is another challenge. Although the preparation of multicomponent carrier-free nanodrugs is simple and green, its preparation process has not been industrially scaled up.

We advocate that carrier-free nanodrugs have both a general meaning and special meaning. What remains clear is that the two meanings provide different perspectives for recognizing carrier-free nanodrugs. Carrier-free nanodrugs in the general meaning have versatile, diversified design enabling active targeting and synergistic therapeutic efficacy due to the content of active and functional ingredients. Carrier-free nanodrugs in the special meaning are assembled by one or more FDA-approved pure drug molecules that can be easily tailored for clinical needs. Overall, it is anticipated that with the continuous development of science and technology, more ingenious, more effective and easy-to-assemble carrier-free nanodrugs are promising, and will undoubtedly become a powerful candidate for clinical medicine.

Author contributions

Lifei Huang: investigation, conceptualization, and writing – original draft, Shuyang Hu: investigation and Ya-nan Fu: supervision, Yan Wan: investigation, Guofeng Li: supervision and writing –review & editing, Xing Wang: conceptualization, supervision, writing –review & editing, and funding acquisition. All authors have read and agreed to the final version of the manuscript.

Conflicts of interest

There are no conflicts to declare.

Acknowledgements

This work was supported by the National Natural Science Foundation of China (52273118), and the Key Program of Beijing Natural Science Foundation (Z200025).

References

1 R. L. Siegel, K. D. Miller and A. Jemal, *CA-Cancer J. Clin.*, 2019, **69**, 7–34.
2 O. Strobel, J. Neoptolemos, D. Jäger and M. W. Büchler, *Nat. Rev. Clin. Oncol.*, 2019, **16**, 11–26.
3 L. Huang, S. Yang, M. Bai, Y. Lin, X. Chen, G. Li, L.-G. Cui and X. Wang, *Colloids Surf., B*, 2022, **213**, 112382.
4 K. Bukowski, M. Kciuk and R. Kontek, *Int. J. Mol. Sci.*, 2020, **21**, 3233.
5 S.-Y. Qin, Y.-J. Cheng, Q. Lei, A.-Q. Zhang and X.-Z. J. B. Zhang, *Biomaterials*, 2018, **171**, 178–197.
6 M. Jarosz-Biej, R. Smolarczyk, T. Cichoń and N. Kułach, *Int. J. Mol. Sci.*, 2019, **20**, 3212.
7 T. O. Olusanya, R. R. Haj Ahmad, D. M. Ibegbu, J. R. Smith and A. A. Elkordy, *Molecules*, 2018, **23**, 907.
8 J. K. Patra, G. Das, L. F. Fraceto, E. V. R. Campos, M. D. P. Rodriguez-Torres, L. S. Acosta-Torres, L. A. Diaz-Torres, R. Grillo, M. K. Swamy, S. Sharma, S. Habtemariam and H. S. Shin, *J. Nanobiotechnol.*, 2018, **16**, 71.
9 S. Y. Qin, A. Q. Zhang, S. X. Cheng, L. Rong and X. Z. Zhang, *Biomaterials*, 2017, **112**, 234–247.
10 S. Guo and L. Huang, *Biotechnol. Adv.*, 2014, **32**, 778–788.
11 S. Hossen, M. K. Hossain, M. K. Basher, M. N. H. Mia, M. T. Rahman and M. J. Uddin, *J. Adv. Res.*, 2019, **15**, 1–18.
12 A. Wicki, D. Witzigmann, V. Balasubramanian and J. Huwyler, *J. Controlled Release*, 2015, **200**, 138–157.
13 J. P. Moschwitzer, *Int. J. Pharm.*, 2013, **453**, 142–156.

Published on 03 November 2022. Downloaded by Beijing University of Chemical Technology on 9/1/2025 2:07:42 PM.

14 R. M. Mirza, S. P. Ahirrao and S. J. Kshirsagar, *J. Appl. Pharmaceutical Res.*, 2017, **5**, 1–13.
15 L. Gao, D. Zhang and M. Chen, *J. Nanopart. Res.*, 2008, **10**, 845–862.
16 J. Lin, C. Li, Y. Guo, J. Zou, P. Wu, Y. Liao, B. Zhang, J. Le, R. Zhao and J. W. Shao, *J. Mater. Chem. B*, 2019, **7**, 6914–6923.
17 W. Ma, H. Su, A. G. Cheetham, W. Zhang, Y. Wang, Q. Kan and H. Cui, *J. Controlled Release*, 2017, **263**, 102–111.
18 W. Li, Y. Yang, C. Wang, Z. Liu, X. Zhang, F. An, X. Diao, X. Hao and X. Zhang, *Chem. Commun.*, 2012, **48**, 8120–8122.
19 M. Y. Yang, R. R. Zhao, Y. F. Fang, J. L. Jiang, X. T. Yuan and J. W. Shao, *Int. J. Pharm.*, 2019, **570**, 118663.
20 X. Zhang, N. Li, S. Zhang, B. Sun, Q. Chen, Z. He, C. Luo and J. Sun, *Med. Res. Rev.*, 2020, **40**, 1754–1775.
21 Y. Wang, P. Yang, X. Zhao, D. Gao, N. Sun, Z. Tian, T. Ma and Z. Yang, *Int. J. Mol. Sci.*, 2018, **19**, 2963.
22 H. Mei, S. Cai, D. Huang, H. Gao, J. Cao and B. He, *Bioact. Mater.*, 2022, **8**, 220–240.
23 S. Karaosmanoglu, M. Zhou, B. Shi, X. Zhang, G. R. Williams and X. Chen, *J. Controlled Release*, 2021, **329**, 805–832.
24 L. Huang, S. Zhao, F. Fang, T. Xu, M. Lan and J. Zhang, *Biomaterials*, 2021, **268**, 120557.
25 S. Fu, G. Li, W. Zang, X. Zhou, K. Shi and Y. Zhai, *Acta Pharm. Sin. B*, 2022, **12**, 92–106.
26 W. R. Zhuang, Y. Wang, P. F. Cui, L. Xing, J. Lee, D. Kim, H. L. Jiang and Y. K. Oh, *J. Controlled Release*, 2019, **294**, 311–326.
27 W. Ma, A. G. Cheetham and H. Cui, *Nano Today*, 2016, **11**, 13–30.
28 H. Kasai, T. Murakami, Y. Ikuta, Y. Koseki, K. Baba, H. Oikawa, H. Nakanishi, M. Okada, M. Shoji, M. Ueda, H. Imahori and M. Hashida, *Angew. Chem., Int. Ed. Engl.*, 2012, **51**, 10315–10318.
29 K. Baba, H. E. Pudavar, I. Roy, T. Y. Ohulchanskyy, Y. Chen, R. K. Pandey and P. N. Prasad, *Mol. Pharm.*, 2007, **4**, 289–297.
30 F. Chen, Y. Zhao, Y. Pan, X. Xue, X. Zhang, A. Kumar and X. J. Liang, *Mol. Pharm.*, 2015, **12**, 2237–2244.
31 Y. Zhao, F. Chen, Y. Pan, Z. Li, X. Xue, C. I. Okeke, Y. Wang, C. Li, L. Peng, P. C. Wang, X. Ma and X. J. Liang, *ACS Appl. Mater. Interfaces*, 2015, **7**, 19295–19305.
32 Y. Xiao, J. Liu, M. Guo, H. Zhou, J. Jin, J. Liu, Y. Liu, Z. Zhang and C. Chen, *Nanoscale*, 2018, **10**, 12639–12649.
33 Y. Wen, W. Zhang, N. Gong, Y. F. Wang, H. B. Guo, W. Guo, P. C. Wang and X. J. Liang, *Nanoscale*, 2017, **9**, 14347–14356.
34 C. Li, J. Lin, P. Wu, R. Zhao, J. Zou, M. Zhou, L. Jia and J. Shao, *Bioconjugate Chem.*, 2018, **29**, 3495–3502.
35 X. Wang, X. Cheng, L. He, X. Zeng, Y. Zheng and R. Tang, *ACS Appl. Mater. Interfaces*, 2019, **11**, 28597–28609.
36 R. Zhang, R. Xing, T. Jiao, K. Ma, C. Chen, G. Ma and X. Yan, *ACS Appl. Mater. Interfaces*, 2016, **8**, 13262–13269.
37 Y. Zhao, Y. Zhao, Q. Ma, H. Zhang, Y. Liu, J. Hong, Z. Ding, M. Liu and J. Han, *Colloids Surf., B*, 2020, **188**, 110722.
38 M. Zhao, S. Wan, X. Peng, B. Zhang, Q. Pan, S. Li, B. He and Y. Pu, *J. Mater. Chem. B*, 2020, **8**, 1235–1244.
39 L. P. Zhao, R. R. Zheng, H. Q. Chen, L. S. Liu, X. Y. Zhao, H. H. Liu, X. Z. Qiu, X. Y. Yu, H. Cheng and S. Y. Li, *Nano Lett.*, 2020, **20**, 2062–2071.
40 S. Hu, C. Dong, J. Wang, K. Liu, Q. Zhou, J. Xiang, Z. Zhou, F. Liu and Y. Shen, *J. Controlled Release*, 2020, **324**, 250–259.
41 J. Zhang, Y. C. Liang, X. Lin, X. Zhu, L. Yan, S. Li, X. Yang, G. Zhu, A. L. Rogach, P. K. Yu, P. Shi, L. C. Tu, C. C. Chang, X. Zhang, X. Chen, W. Zhang and C. S. Lee, *ACS Nano*, 2015, **9**, 9741–9756.
42 F. Yang, Q. Ji, R. Liao, S. Li, Y. Wang, X. Zhang, S. Zhang, H. Zhang, Q. Kan and J. Sun, *Chin. Chem. Lett.*, 2022, **33**, 1927–1932.
43 B. Sun, C. Luo, H. Yu, X. Zhang, Q. Chen, W. Yang, M. Wang, Q. Kan, H. Zhang, Y. Wang, Z. He and J. Sun, *Nano Lett.*, 2018, **18**, 3643–3650.
44 F. Jing, Q. Guo, W. Xu, H. Qu and Z. Sui, *Bioorg. Med. Chem. Lett.*, 2018, **28**, 826–830.
45 S. Zhang, J. Guan, M. Sun, D. Zhang, H. Zhang, B. Sun, W. Guo, B. Lin, Y. Wang, Z. He, C. Luo and J. Sun, *Drug Delivery*, 2017, **24**, 1460–1469.
46 D. Zhao, W. Tao, S. Li, L. Li, Y. Sun, G. Li, G. Wang, Y. Wang, B. Lin, C. Luo, Y. Wang, M. Cheng, Z. He and J. Sun, *Nanoscale Horiz.*, 2020, **5**, 886–894.
47 Z. Zhang, Y. Wang, Q. Ma, S. Zhang, H. Liu, B. Zhao, R. Liu, W. Wang, B. Du, Y. Zhong and D. Kong, *Chem. Eng. J.*, 2021, **406**, 126801.
48 X. Zhang, J. Xiong, K. Wang, H. Yu, B. Sun, H. Ye, Z. Zhao, N. Wang, Y. Wang, S. Zhang, W. Zhao, H. Zhang, Z. He, C. Luo and J. Sun, *Bioact. Mater.*, 2021, **6**, 2291–2302.
49 T. Zhang, P. Huang, L. Shi, Y. Su, L. Zhou, X. Zhu and D. Yan, *Mol. Pharm.*, 2015, **12**, 2328–2336.
50 P. Huang, D. Wang, Y. Su, W. Huang, Y. Zhou, D. Cui, X. Zhu and D. Yan, *J. Am. Chem. Soc.*, 2014, **136**, 11748–11756.
51 M. Chen, S. Chen, F. Zhu, F. Wang, H. Tian, Z. Fan, S. Ke, Z. Hou and Y. Li, *J. Mater. Chem. B*, 2020, **8**, 3829–3841.
52 W. Qu, Q. Yang, G. Wang, Z. Wang, P. Huang, W. Huang, R. Zhang and D. Yan, *RSC Adv.*, 2020, **10**, 8958–8966.
53 M. Pakdel, H. Raissi and S. T. Hosseini, *J. Comput. Chem.*, 2020, **41**, 1486–1496.
54 L. Ling, M. Ismail, Z. Shang, Y. Hu and B. Li, *Int. J. Pharm.*, 2020, **577**, 119049.
55 M. Hu, P. Huang, Y. Wang, Y. Su, L. Zhou, X. Zhu and D. Yan, *Bioconjugate Chem.*, 2015, **26**, 2497–2506.
56 M. Sun, Q. Qian, L. Shi, L. Xu, Q. Liu, L. Zhou, X. Zhu, J.-M. Yue and D. Yan, *Sci. China: Chem.*, 2020, **63**, 35–41.
57 P. Huang, J. Ao, L. Zhou, Y. Su, W. Huang, X. Zhu and D. Yan, *Bioconjugate Chem.*, 2016, **27**, 1564–1568.
58 W. Qu, Q. Yang, G. Wang, Z. Wang, P. Huang, W. Huang, R. Zhang and D. Yan, *RSC Adv.*, 2020, **10**, 8958–8966.
59 K. Xue, H. Tian, F. Zhu, F. Wang, Z. Fan, Q. Zhao, Z. Hou and Y. Li, *ACS Appl. Mater. Interfaces*, 2020, **29**, 32477–32492.
60 N. Yu, J. Li, Y. Zhang, D. Ding, X. Li and H. Xu, *RSC Adv.*, 2020, **10**, 12999–13005.

 This journal is © The Royal Society of Chemistry 2022

Published on 03 November 2022. Downloaded by Beijing University of Chemical Technology on 9/1/2025 2:07:42 PM.

61 Z. Fan, Y. Wang, S. Xiang, W. Zuo, D. Huang, B. Jiang, H. Sun, W. Yin, L. Xie and Z. Hou, *J. Mater. Chem. B*, 2020, **8**, 1922–1934.
62 M. K. Shim, J. Park, H. Y. Yoon, S. Lee, W. Um, J. H. Kim, S. W. Kang, J. W. Seo, S. W. Hyun, J. H. Park, Y. Byun, I. C. Kwon and K. Kim, *J. Controlled Release*, 2019, **294**, 376–389.
63 X. Li, N. Yu, J. Li, J. Bai, D. Ding, Q. Tang and H. Xu, *ACS Appl. Mater. Interfaces*, 2020, **12**, 10096–10106.
64 W. Zuo, D. Chen, Z. Fan, L. Chen, Z. Zhu, Q. Zhu and X. Zhu, *Acta Biomater.*, 2020, **111**, 327–340.
65 C. Hu, X. He, Y. Chen, X. Yang, L. Qin, T. Lei, Y. Zhou, T. Gong, Y. Huang and H. Gao, *Adv. Funct. Mater.*, 2021, **31**, 2007149.
66 W. Feng, Y. Lv, Z. Chen, F. Wang, Y. Wang, Y. Pei, W. Jin, C. Shi, Y. Wang, Y. Qu, W. Ji, L. Pu, X.-W. Liu and Z. Pei, *Chem. Eng. J.*, 2021, **417**, 129178.
67 G. Yan, R. Chen, N. Xiong, J. Song, X. Wang and R. Tang, *Colloids Surf., B*, 2020, **191**, 111000.
68 S. Hu, E. Lee, C. Wang, J. Wang, Z. Zhou, Y. Li, X. Li, J. Tang, D. H. Lee, X. Liu and Y. Shen, *J. Controlled Release*, 2015, **220**, 175–179.
69 C. Dong, Q. Jiang, X. Qian, W. Wu, W. Wang, L. Yu and Y. Chen, *Nanoscale*, 2020, **12**, 5587–5600.
70 J.-S. Lan, L. Liu, R.-F. Zeng, Y.-H. Qin, J.-W. Hou, S.-S. Xie, S. Yue, J. Yang, R. J. Y. Ho, Y. Ding and T. Zhang, *Chem. Eng. J.*, 2020, **407**, 127212.
71 L. Liu, Y. Bao, J. Wang, C. Xiao and L. Chen, *Dyes Pigm.*, 2020, **177**, 107922.
72 S. Li, F. Yang, X. Sun, Y. Wang, X. Zhang, S. Zhang, H. Zhang, Q. Kan, J. Sun, Z. He and C. Luo, *Chem. Eng. J.*, 2021, **426**, 130838.
73 X. Kang, Y. Yu, Z. Chen, Y. Wu, D. Wei, Y. Zhao, F. Wang and H. J. Xiao, *J. Mater. Chem. B*, 2019, **7**, 3346–3350.
74 X. Kang, Y. Wang, Z. Chen, Y. Wu, H. Chen, X. Yang and C. Yu, *Chem. Commun.*, 2020, **56**, 11271–11274.
75 Q. Hao, Y. Chen, Z. Huang, J.-F. Xu, Z. Sun and X. Zhang, *ACS Appl. Mater. Interfaces*, 2018, **10**, 5365–5372.
76 D. Gibson, *J. Inorg. Biochem.*, 2019, **191**, 77–84.
77 S. M. Meier-Menches, C. Gerner, W. Berger, C. G. Hartinger and B. K. Keppler, *Chem. Soc. Rev.*, 2018, **47**, 909–928.
78 A. Di Martino, O. A. Guselnikova, M. E. Trusova, P. S. Postnikov and V. Sedlarik, *Int. J. Pharm.*, 2017, **526**, 380–390.
79 E. Alessio and Z. Guo, *Eur. J. Inorg. Chem.*, 2017, 1539–1540.
80 R. R. Ramoutar and J. L. Brumaghim, *Cell Biochem. Biophys.*, 2010, **58**, 1–23.
81 B. B. Caravieri, N. A. M. de Jesus, L. K. de Oliveira, M. D. Araujo, G. P. Andrade and E. F. Molina, *ACS Appl. Bio Mater.*, 2019, **2**, 1875–1883.
82 J. Tan, C. Li, Q. Wang, S. Li, S. Chen, J. Zhang, P. C. Wang, L. Ren and X. J. Liang, *Mol. Pharm.*, 2018, **15**, 1724–1728.
83 L. Shi, F. Hu, Y. Duan, W. Wu, J. Dong, X. Meng, X. Zhu and B. Liu, *ACS Nano*, 2020, **14**, 2183–2190.
84 Z. Fan, B. Jiang, Q. Zhu, S. Xiang, L. Tu, Y. Yang, Q. Zhao, D. Huang, J. Han, G. Su, D. Ge and Z. Hou, *ACS Appl. Mater. Interfaces*, 2020, **12**, 14884–14904.
85 L. Tu, Z. Fan, F. Zhu, Q. Zhang, S. Zeng, Z. Chen, L. Ren, Z. Hou, S. Ye and Y. Li, *J. Mater. Chem. B*, 2020, **8**, 5667–5681.
86 L. Chen, W. Zuo, Z. Xiao, Q. Jin, J. Liu, L. Wu, N. Liu and X. Zhu, *J. Colloid Interface Sci.*, 2021, **600**, 243–255.
87 Z. Zhang, R. Wang, X. Huang, R. Luo, J. Xue, J. Gao, W. Liu, F. Liu, F. Feng and W. Qu, *ACS Appl. Mater. Interfaces*, 2020, **12**, 5680–5694.
88 R. Oun, Y. E. Moussa and N. J. Wheate, *Dalton Trans.*, 2018, **47**, 6645–6653.
89 W. Xie, G. Zhang, Z. Guo, J. Lu, J. Ye, W. Xu, X. Gao, K. Yue, Y. Wei and L. Zhao, *Adv. Funct. Mater.*, 2022, **32**, 2107518.
90 T. Li, S. Pan, H. Zhuang, S. Gao and H. Xu, *ACS Appl. Bio Mater.*, 2020, **3**, 1283–1292.
91 C. Wang, L. Li, S. Zhang, Y. Yan, Q. Huang, X. Cai, J. Xiao and Y. Cheng, *Small*, 2020, **16**, e2004829.
92 M. Li, X. Sun, N. Zhang, W. Wang, Y. Yang, H. Jia and W. Liu, *Adv. Sci.*, 2018, **5**, 1800155.
93 J. Xin, K. Zhang, J. Huang, X. Luo, X. Gong, Z. Yang, H. Lin, H. Shan and J. Gao, *Biomater. Sci.*, 2018, **7**, 262–271.
94 C. Ren, Y. Gao, Y. Guan, Z. Wang, L. Yang, J. Gao, H. Fan and J. Liu, *ACS Appl. Mater. Interfaces*, 2019, **11**, 33706–33715.
95 Q. Mou, Y. Ma, X. Zhu and D. Yan, *J. Controlled Release*, 2016, **230**, 34–44.
96 Y. Liu, K. Li, Y. Wu, J. Ma, P. Tang, Y. Liu and D. Wu, *Biomater. Sci.*, 2019, **7**, 3662–3674.
97 Y. Li, J. Lin, G. Liu, J. Ma, L. Xie, F. Guo, X. Zhu and Z. Hou, *Int. J. Pharm.*, 2016, **512**, 194–203.
98 Y. Li, J. Lin, Y. Huang, Y. Li, X. Yang, H. Wu, S. Wu, L. Xie, L. Dai and Z. Hou, *ACS Appl. Mater. Interfaces*, 2015, **7**, 25553–25559.
99 K. Jiang, L. Han, Y. Guo, G. Zheng, L. Fan, Z. Shen, R. Zhao and J. Shao, *J. Mater. Chem. B*, 2017, **5**, 9121–9129.
100 Y. Chen, Q. Chen, Q. Zhu, J. Liu, Y. Li, X. Gao, D. Chen and X. Zhu, *Mol. Pharm.*, 2019, **16**, 2470–2480.
101 Z. Xu, X. Shi, M. Hou, P. Xue, Y. E. Gao, S. Liu and Y. Kang, *Colloids Surf., B*, 2017, **150**, 50–58.
102 C. Cheng, B. Sui, M. Wang, X. Hu, S. Shi and P. Xu, *Adv. Healthcare Mater.*, 2020, **9**, e2001128.
103 Y. Li, J. Lin, Z. Cai, P. Wang, Q. Luo, C. Yao, Y. Zhang, Z. Hou, J. Liu and X. Liu, *J. Controlled Release*, 2020, **321**, 222–235.
104 Z. Tang, Y. Liu, M. He and W. Bu, *Angew. Chem., Int. Ed. Engl.*, 2019, **58**, 946–956.
105 V. Shanmugam, S. Selvakumar and C. S. Yeh, *Chem. Soc. Rev.*, 2014, **43**, 6254–6287.
106 W. He, Y. Jiang, Q. Li, D. Zhang, Z. Li and Y. Luan, *Acta Biomater.*, 2019, **84**, 356–366.
107 J. Zhao, G. Jin, G. Weng, J. Li, J. Zhu and J. Zhao, *Drug Discovery Today*, 2017, **22**, 1367–1374.
108 Y. Wei, L. Kong, H. Chen, Y. Liu, Y. Xu, H. Wang, G. Fang, X. Shao, F. Liu and Y. Wang, *Chem. Eng. J.*, 2022, **429**, 132134.
109 J. Dong, M. Liu, R. Jiang, H. Huang, Q. Wan, Y. Wen, J. Tian, Y. Dai, X. Zhang and Y. Wei, *J. Colloid Interface Sci.*, 2018, **528**, 192–199.

Published on 03 November 2022. Downloaded by Beijing University of Chemical Technology on 9/1/2025 2:07:42 PM.

110 C. Ma, G. Xie, X. Zhang, L. Yang, Y. Li, H. Liu, K. Wang and Y. Wei, *Dyes Pigm.*, 2017, **139**, 672–680.
111 Q. Guo, Y. Wang, L. Zhang, P. Zhang, Y. Yu, Y. Zhang, C. Li, S. Jiang and X. Zhang, *Chem. Sci.*, 2019, **10**, 7878–7886.
112 S. Mallidi, G. P. Luke and S. Emelianov, *Trends Biotechnol.*, 2011, **29**, 213–221.
113 M. Xu and L. V. Wang, *Rev. Sci. Instrum.*, 2006, **77**, 041101.
114 Y. Li, G. Liu, J. Ma, J. Lin, H. Lin, G. Su, D. Chen, S. Ye, X. Chen, X. Zhu and Z. Hou, *J. Controlled Release*, 2017, **258**, 95–107.
115 R. Zhao, G. Zheng, L. Fan, Z. Shen, K. Jiang, Y. Guo and J. W. Shao, *Acta Biomater.*, 2018, **70**, 197–210.
116 Y. Li, J. Lin, J. Ma, L. Song, H. Lin, B. Tang, D. Chen, G. Su, S. Ye, X. Zhu, F. Luo and Z. Hou, *ACS Appl. Mater. Interfaces*, 2017, **9**, 34650–34665.
117 Y. Fan and J. Moon, *Vaccines*, 2015, **3**, 662–685.
118 K. Shao, S. Singha, X. Clemente-Casares, S. Tsai, Y. Yang and P. Santamaria, *ACS Nano*, 2015, **9**, 16–30.
119 W. Li, H. F. Wei, H. F. Li, J. Gao, S. S. Feng and Y. J. Guo, *Nanomedicine*, 2014, **9**, 2587–2605.
120 Q. Yang, Y. Xiao, Q. Liu, X. Xu and J. Peng, *ACS Appl. Bio Mater.*, 2020, **3**, 4543–4555.
121 S. Chen, D. Li, X. Du, X. He, M. Huang, Y. Wang, X. Yang and J. Wang, *Nano Today*, 2020, **35**, 100924.
122 L. Tang, Y. Zheng, M. B. Melo, L. Mabardi, A. P. Castano, Y. Q. Xie, N. Li, S. B. Kudchodkar, H. C. Wong, E. K. Jeng, M. V. Maus and D. J. Irvine, *Nat. Biotechnol.*, 2018, **36**, 707–716.
123 L. Fan, B. Zhang, A. Xu, Z. Shen, Y. Guo, R. Zhao, H. Yao and J. W. Shao, *Mol. Pharm.*, 2018, **15**, 2466–2478.
124 L. Wei, Y. Zhao, X. Hu and L. Tang, *ACS Cent. Sci.*, 2020, **6**, 404–412.
125 X. Du, Y. Hou, J. Huang, Y. Pang, C. Ruan, W. Wu, C. Xu, H. Zhang, L. Yin and W. He, *Acta Pharm. Sin. B*, 2021, **11**, 3272–3285.
126 C. Teng, C. Lin, F. Huang, X. Xing, S. Chen, L. Ye, H. S. Azevedo, C. Xu, Z. Wu, Z. Chen and W. He, *Acta Pharm. Sin. B*, 2020, **10**, 1521–1533.
127 L. Xing, C. X. Yang, D. Zhao, L. J. Shen, T. J. Zhou, Y. Y. Bi, Z. J. Huang, Q. Wei, L. Li, F. Li and H. L. Jiang, *J. Controlled Release*, 2021, **331**, 460–471.
128 M. Salih, C. A. Omolo, N. Devnarain, A. A. Elrashedy, C. Mocktar, M. E. S. Soliman and T. Govender, *Pharm. Dev. Technol.*, 2020, **25**, 1090–1108.
129 T. Li, P. Wang, W. Guo, X. Huang, X. Tian, G. Wu, B. Xu, F. Li, C. Yan, X. J. Liang and H. Lei, *ACS Nano*, 2019, **13**, 6770–6781.
130 G. N. Feng, X. T. Huang, X. L. Jiang, T. W. Deng, Q. X. Li, J. X. Li, Q. N. Wu, S. P. Li, X. Q. Sun, Y. G. Huang, A. P. Qin, L. Liang and J. J. Fu, *Front. Chem.*, 2021, **9**, 666408.
131 H. Kim, W. Zhang, J. Hwang, E. K. An, Y. K. Choi, E. Moon, M. Loznik, Y. H. Huh, A. Herrmann, M. Kwak and J. O. Jin, *Biomaterials*, 2021, **277**, 121081.

 This journal is © The Royal Society of Chemistry 2022

证书号第5666051号

发明专利证书

发明名称：具有隔热功能的自愈性水凝胶及其应用

发明人：王兴;黄丽霏;付雅南

专利号：ZL 2022 1 0068753.0

专利申请日：2022年01月21日

专利权人：北京化工大学

地址：100029 北京市朝阳区北三环东路15号

授权公告日：2022年12月27日　　授权公告号：CN 114404676 B

国家知识产权局依照中华人民共和国专利法进行审查，决定授予专利权，颁发发明专利证书并在专利登记簿上予以登记。专利权自授权公告之日起生效。专利权期限为二十年，自申请日起算。

专利证书记载专利权登记时的法律状况。专利权的转移、质押、无效、终止、恢复和专利权人的姓名或名称、国籍、地址变更等事项记载在专利登记簿上。

局长
申长雨

国家知识产权局

2022年12月27日

其他事项参见续页

证 书 号 第 5666051 号

专利权人应当依照专利法及其实施细则规定缴纳年费。本专利的年费应当在每年 01 月 21 日前缴纳。未按照规定缴纳年费的，专利权自应当缴纳年费期满之日起终止。

申请日时本专利记载的申请人、发明人信息如下：

申请人：

北京化工大学

发明人：

王兴；黄丽霏；付雅南